

Microstructural-Mechanical Property Relationships in WC-Co composites

Chang-Soo Kim

Ph. D. Thesis

Materials Science and Engineering Department

Carnegie Mellon University

Pittsburgh, PA 15213, USA

Thesis Committee:

Dr. Gregory S. Rohrer (Advisor, Carnegie Mellon University)

Ted R. Massa (Co-advisor, Kennametal Incorporated)

Dr. Warren M. Garrison (Carnegie Mellon University)

Dr. Anthony D. Rollett (Carnegie Mellon University)

Dr. David M. Saylor (Food and Drug Administration)

Dr. Paul Wynblatt (Carnegie Mellon University)

Abstract

While empirical relationships between the mechanical properties of WC-Co composites and the carbide grain size and carbide volume fraction are qualitatively well-known, the influence of other microstructural features on the macroscopic properties has been less clear. In this thesis, a comprehensive study of the effect of the interface character distribution (grain shape and misorientation distribution of WC crystals), grain size, size distribution, contiguity, and carbide volume fraction on the mechanical properties (fracture strength) of WC-Co composites is described. To do this, methods were developed to accurately measure microstructural features, characterize interfaces, and predict mechanical properties.

Atomic force microscopy (AFM) and orientation imaging microscopy (OIM) have been used to determine the WC/WC boundary and WC/Co interface positions in WC-Co composites with Co volume fractions from 10 % to 30 % and mean carbide grain sizes from 1 to 7 microns. Direct measurements of the carbide and cobalt area fractions show that the log-normal distributions of carbide grain size and binder mean free path distributions are Gaussian and that there is a very strong linear correlation between the volume fraction of the binder and the contiguity of carbide phase. The number of vertices per carbide grain is nearly constant and it is weakly influenced by the Co volume fraction. Empirical expressions involving the grain size and carbide contiguity fit well to measured hardness and fracture toughness data.

Stereological analysis of the carbide grain shapes shows that WC particles in these materials have similar distributions of habit planes, with $\{10\bar{1}0\}$ prism facets and

the {0001} basal planes in contact with Co. The orientation imaging microscopy (OIM) measurements demonstrate an absence of orientation texture and that the carbide grain boundaries have similar misorientation distributions, with a high population grain boundaries that have a 90° twist misorientation about the $[10\bar{1}0]$ axis and 30° twist and asymmetric misorientations about the [0001] axis.

Using a two-dimensional finite element analysis (FEM) of the stress-strain field in these materials, a brittle fracture model for the prediction of fracture strength has been developed. The model assumes that a crack initiates either along carbide/carbide boundaries or in carbide grains. When the fracture energy is $\sim 49 \text{ J/m}^2$, the calculated fracture strength under a combined (thermal and mechanical) load shows good agreement with the experimentally measured data. The calibrated model was then applied to the hypothetical microstructures of WC-Co composites. The degree of carbide connectivity (contiguity), orientation and/or misorientation texture appear to be the most important parameter for improving the fracture strength of these materials.

Table of Contents

Chapter 1 – Introduction	1
1.1 Cemented carbides systems -----	1
1.1.1 History -----	1
1.1.2 Classification -----	2
i) WC-Co grades -----	2
ii) Alloyed grades -----	2
1.1.3 Physical Properties -----	3
1.1.4 Applications -----	3
1.2 Motivations -----	4
1.3 Objectives -----	6
1.4 References -----	7
Chapter 2 – Background	8
2.1 Shapes of carbide particles -----	8
2.1.1 Anisotropy -----	8
2.1.2 Equilibrium shape of WC crystals in a Co binder -----	10
Wulff plot -----	11
2.2 Carbide/carbide boundaries -----	13
2.2.1 Basic crystallography -----	13

i) Orientation representation -----	13
Coordinate system transformations -----	13
Fundamental zone (Standard triangle, unique triangle) -----	14
Pole figure (PF) -----	16
Inverse pole figure (IPF) -----	16
ii) Grain boundary representation -----	16
Misorientations -----	17
Misorientation distributions in Euler space -----	18
Misorientation distributions in axis-angle space -----	19
Misorientations in Rodrigues space -----	21
Tilt and twist boundaries -----	21
Coincidence site lattice (CSL) boundaries -----	23
iii) Texture -----	24
Orientation texture -----	24
Misorientation texture -----	25
Grain boundary plane texture -----	26
2.2.2 Character of carbide/carbide grain boundaries -----	27
2.3 Measurements of microstructural parameters -----	28
2.3.1 Linear-intercept analysis -----	28
2.3.2 Microstructural parameters -----	29
i) Volume fraction -----	29
ii) Particle size and size distribution -----	29
iii) Contiguity of carbide phase -----	30

iv) Angularity of carbide phase	31
2.4 Mechanical behavior of WC-Co composites	32
2.4.1 Elastic stress and stored energy	32
i) Stress invariant and strain invariant	32
ii) Elastic energy density	34
2.4.2 Elastic and plastic behaviors	34
i) Elastic constants	34
ii) Plastic deformation	36
2.4.3 Fracture approaches	37
i) Griffith condition	37
ii) Energy release rate and critical intensity factor	38
2.5 Microstructure-property relations of WC-Co composites	39
2.5.1 Mechanical properties	39
i) Hardness	39
ii) Fracture toughness	40
iii) Transverse rupture strength (TRS)	41
2.5.2 Past models for microstructure-property relations	42
i) Hardness	43
ii) Fracture toughness	44
2.6 Numerical models for structural analysis	47
2.6.1 Finite element methods (FEM) for stress-strain calculations	48

2.6.2 Previous analyses for the prediction of crack paths in WC-Co composites using FEM -----	51
2.6.3 Object-oriented finite element (OOF) model -----	52
2.7 Summary -----	55
2.8 References -----	55
Chapter 3 – Microstructural Characterization	61
3.1 Samples -----	61
3.2 Microstructure and property characterization methods -----	65
3.2.1 Atomic force microscopy (AFM) -----	65
3.2.2 Orientation imaging microscopy (OIM) -----	66
3.2.3 Microstructure analysis -----	67
3.2.4 Measurements of mechanical properties -----	70
3.3 Results -----	72
3.3.1 Grain size, binder mean free path, and size distributions -----	73
3.3.2 Contiguity of carbide phase -----	77
3.3.3 Carbide crystal shape -----	78
3.3.4 Orientation and misorientation distributions -----	81
3.4 Correlation with mechanical properties -----	82
3.4.1 Hardness -----	83
3.4.2 Fracture toughness -----	86

3.5 Summary	89
-------------------	----

3.6 References	90
----------------------	----

Chapter 4 – Analysis of Interfaces in WC-Co Composites 92

4.1 Samples	92
-------------------	----

4.2 Stereological method for interface characterizations	93
--	----

4.2.1 Method overview	93
-----------------------------	----

i) Basic idea	93
---------------------	----

ii) Trace classification	95
--------------------------------	----

iii) Applicability and limitations of stereological analysis	96
--	----

4.2.2 Numerical analysis	98
--------------------------------	----

i) Two- and five-parameter calculations	98
---	----

ii) Number of line segments	101
-----------------------------------	-----

iii) Background subtraction	103
-----------------------------------	-----

iv) Data processing; OIM image clean-up	105
---	-----

4.3 WC/Co interfaces	108
----------------------------	-----

4.3.1 Analysis of grade <i>E</i>	108
--	-----

i) Result from the manual tracings	108
--	-----

ii) Result from the automatic extractions	112
---	-----

4.3.2 Analysis of other grades	113
--------------------------------------	-----

4.4 WC/WC boundaries	116
----------------------------	-----

4.4.1 Analysis of grade <i>A</i> (two-parameter calculation)	116
--	-----

4.4.2 Analysis of other grades (two-parameter calculation) -----	124
4.4.3 Five-parameter calculation -----	126
4.5 Summary -----	129
4.6 References -----	129

Chapter 5 – Finite Element Simulations of Fracture Strength in WC-Co Composites 132

5.1 Simulation methods -----	132
Euler angles in OOF software -----	138
5.2 Results from real microstructures using brittle fracture model -----	138
5.3 Results from hypothetical microstructures using brittle fracture model ---- -----	146
5.3.1 Contiguity -----	147
i) Hypothetical microstructures from simulations -----	147
ii) Hypothetical microstructures from real microstructures -----	153
5.3.2 Angularity -----	157
i) Hypothetical microstructures from simulations -----	157
ii) Hypothetical microstructures from real microstructures of other composites -----	160
5.3.3 Aspect ratio -----	164
i) Hypothetical microstructures from simulations -----	164
5.3.4 Size distribution -----	167

i) Hypothetical microstructures from simulations -----	167
5.3.5 Orientation and Misorientation -----	170
i) Simple examples -----	170
ii) Hypothetical microstructures -----	178
5.4 Summary -----	190
5.5 References -----	190
Chapter 6 – Summary	192
6.1 References -----	196

List of Figures

- 2.1 : Crystal structure of WC
- 2.2 : A typical optical micrograph of WC-Co composites
- 2.3 : Proposed equilibrium shapes of WC crystals
- 2.4 : Schematic illustration of Wulff plot and the corresponding Wulff construction
- 2.5 : Illustration of the laboratory coordinate system and crystal coordinate system
- 2.6 : Schematic representation of transformation from the laboratory coordinate to crystal coordinate system
- 2.7 : A [0001] stereographic projection of hexagonal systems
- 2.8 : Example of misorientation distributions in Euler space
- 2.9 : Example of misorientation distributions in axis-angle space
- 2.10 : Example of misorientation distributions in Rodrigues space
- 2.11 : Schematic illustration of the pure tilt and twist boundaries
- 2.12 : Schematic illustration of CSL boundaries in superimposed simple cubic crystals
- 2.13 : Illustrations of orientation texture
- 2.14 : Illustrations of misorientation texture
- 2.15 : Illustration of grain boundary plane texture
- 2.16 : Schematic illustration of stress tensor. Only x (x_1) and y (x_2) components are shown.
- 2.17 : Schematic plots of the relationship between the mechanical properties and the microstructural parameters
- 2.18 : Schematic illustration of the 3-point transverse rupture strength (TRS) bend test

- 3.1 : AFM images of nine specimen grades
- 3.2 : Advantage of etching in Murakami's reagent
- 3.3 : Typical images of AFM and OIM
- 3.4 : Example of direct measurements
- 3.5 : Plots of the carbide grain size distributions
- 3.6 : Carbide grain diameter distributions for each grade
- 3.7 : Comparison of the measured binder mean free path (direct measurements) and calculated binder mean free path (stereology)
- 3.8 : Variation of the contiguity of carbide phase as a function of the carbide volume fraction.
- 3.9 : Distributions of number of vertices and variation of average number of vertices
- 3.10 : Distributions of the number of vertices for each grade
- 3.11 : Comparison of the calculated hardness by empirical equation with experimentally measured data.
- 3.12 : Comparison of the calculated hardness by empirical equation and the previous models with experimentally measured data.
- 3.13 : Comparison of the calculated fracture toughness by empirical equation with experimentally measured data.
- 3.14 : Comparison of the calculated fracture toughness by empirical equation and the previous models with experimentally measured data.
- 4.1 : Schematic illustration of stereological analysis

- 4.2 : Schematic illustrations for the cross-sections of boundary structures
- 4.3 : Different types of boundaries as a function of resolution angles
- 4.4 : Illustration of discretized domain
- 4.5 : Variation of aspect ratio with the number of line segments included in the calculations
- 4.6 : Example of automatic extraction of line segments
- 4.7 : WC/Co Habit plane probability distribution derived from 50 and 200 WC crystals of grade *E*
- 4.8 : Comparison of WC crystal shape in AFM topography image and OIM inverse pole figure (IPF) map
- 4.9 : The proposed average shape of WC crystal in Co
- 4.10 : Atomic models for the chemical termination of WC prism planes
- 4.11 : WC/Co interface plane distributions from automatic extractions
- 4.12 : Variation of aspect ratio with the carbide volume fraction.
- 4.13 : Pole figure of WC crystals
- 4.14 : Grain boundary population of WC crystals and random objects as a function of misorientation angle
- 4.15 : WC/WC grain boundary misorientation distribution in axis-angle space
- 4.16 : Habit plane probability distribution for 90° boundaries and 30° boundaries of grade *A*
- 4.17 : Schematic representations of the three most common types of grain boundaries in composites
- 4.18 : Habit plane distributions of grad *B* from automatic extractions

4.19 : Grain boundary plane distributions using five-parameter calculations

5.1 : Example of OOF simulations

5.2 : Conversion of colors for OOF simulations

5.3 : Comparison of the calculated and measured moduli for each grade

5.4 : Stress invariant 1 and elastic energy density distributions (from grade A) under a combined load

5.5 : Comparison of the calculated and measured strengths for each grade

5.6 : Examples of hypothetical microstructures (for contiguity) with their stress invariant 1 and elastic energy density distributions under a mechanical load

5.7 : Average stresses in the composites, carbide and binder phases with different contiguities

5.8 : Plot of the calculated fracture strength with different contiguities

5.9 : Examples of hypothetical microstructures (for contiguity) with their EED distributions

5.10 : Examples of hypothetical microstructures (for contiguity) with their elastic energy density distributions

5.11 : Schematic illustration of stress distributions of high and low contiguity microstructures

5.12 : Examples of hypothetical microstructures (for angularity) with their SI1 and EED distributions

5.13 : Plot of the calculated fracture strength with different angularities

5.14 : Examples of hypothetical microstructures (for angularity) with their EED distributions

5.15 : Schematic illustration of the stress concentration at sharp edge of WC phase in a y-elongation simulation

5.16 : Examples of hypothetical microstructures (for aspect ratio) with their SI1 and EED distributions

5.17 : Plot of the calculated fracture strength with different aspect ratios

5.18 : Schematic illustration of the stress concentrations with different aspect ratios in a y-elongation simulation

5.19 : Examples of hypothetical microstructures (for size ratio) with their EED distributions

5.20 : Plot of the calculated fracture strength with different size ratios

5.21 : Schematic illustration of the stress concentrations with different size ratios in a y-elongation simulation

5.22 : Schematic illustration of $(001)^C//[001]^S$ orientation texture samples (pseudo-cubic materials) with different misorientations

5.23 : SI1 distribution of [001] orientation texture samples (pseudo-cubic materials) with different misorientations

5.24 : EED distribution of [001] orientation texture samples (pseudo-cubic materials) with different misorientations

5.25 : Effects of orientation and misorientation distributions on stress and elastic energy density distributions

5.26 : Stored energy density variation with orientation and misorientation textures

5.27 : Estimated fracture strength in hypothetical microstructures with and without textures

5.28 : deviation angle (Δ) between the [001] sample axis and a $\langle 0001 \rangle$ crystal axis

5.29 : Probability of finding a crystal as a function of texture intensity factor (β) and deviation angle (Δ) from a sample axis

5.30 : Calculated modulus with different orientation textures (from grade A)

5.31 : Schematic illustration of the orientation in [001] texture and [100] texture

5.32 : SII distributions with different orientation textures (from grade A)

5.33 : EED distributions with different orientation textures (from grade A)

5.34 : The calculated fracture strength and fracture strength increase with different orientation textures

5.35 : The calculated fracture strength increase in the hypothetical microstructures of grades A, B, C, and E

5.36: The calculated maximum fracture strength increase as a function of contiguities

6.1 : Schematic illustration of the effects of microstructural features on the fracture strength of composites.

List of Tables

3.1 : Carbide volume fractions for each specimen grade

3.2 : Mechanical properties for each grade

3.3 : Summary of the results of microstructures

5.1 : Elastic constants of WC and Co

5.2 : Summary of the microstructural and mechanical properties for grades *A*, *B*, *C*, and *E*

Chapter 1

Introduction

Cemented carbides (or sintered carbides) are common hard materials which have outstanding mechanical properties that make them commercially useful in machining, mining, metal cutting, metal forming, construction, wear parts, and other applications [1-3]. Since the early 20th century, the cemented carbides have been widely used in many manufacturing processes that benefit from their combination of high hardness, fracture toughness, strength, and wear resistance. This chapter provides a brief overview of cemented carbide systems, describes the motivation for the current work, and defines the objectives of this thesis.

1.1 Cemented carbide systems

1.1.1 History

Tungsten monocarbide (WC, usually referred to as tungsten carbide) was discovered by Henri Moissan in 1893 during his search for a method to make synthetic diamonds [4]. He found that the hardness of WC is comparable to that of diamond. This material, however, proved to be so brittle that its commercial use was seriously limited. Subsequently, research was focused on improving its toughness, and significant contributions to the development of cemented carbides were made in the 1920's by Karl Schröter [4]. Employing cobalt (Co) as a binding material, Schröter developed a

compacting and sintering process for cemented tungsten carbides (WC-Co) that is still widely used to manufacture WC-Co composites. Most of the further developments were modifications of the Schröter's process, involving replacement of part or all of the WC with other carbides, such as titanium carbide (TiC), tantalum carbide (TaC), and/or niobium carbide (NbC).

1.1.2 Classification

i) WC-Co grades

Straight grades, sometimes referred to as unalloyed grades, are nominally pure WC-Co composites. They contain 3-13 w/o (weight percent) Co for cutting tool grades and up to 30 w/o Co for wear resistant parts. The average carbide particle size varies from sub-micron to eight microns. Straight grades are used for machining cast iron, nonferrous alloys, and non-metallic materials, but generally not for the machining of steel. This thesis is focused on the study of straight grades.

ii) Alloyed grades

Alloyed grades are also referred to as steel cutting grades, or crater resistance grades, which have been developed to prohibit cratering during the machining of steel. The basic compositions of alloyed grades are 3-12 w/o Co, 2-8 w/o TiC, 2-8 w/o TaC, and 1-5 w/o NbC. The average carbide particle size of these grades is usually between 0.8 and 4 μm . In this thesis, only a single alloyed grade was studied, as an example of a microstructure that is significantly different from the straight grades.

1.1.3 Physical Properties

The physical properties of these composites depend on microstructural features, such as grain sizes, size distributions, grain shapes, orientations, misorientations, and the volume fraction of the carbide phase. The hardness, toughness, and fracture strength of WC-Co composites range from 850 to 2000 kg/mm² (Vickers hardness, *HV*), from 11 to 25 MPa (critical stress intensity factor, plane strain fracture toughness, *K_{IC}*), and from 1.5 to 4 GPa (transverse rupture strength, TRS), respectively. Also, it is known that the wear resistance of these materials is five to ten times higher than that of a typical tool steel. The details of the physical properties of WC-Co composites will be described in Chapter 2. It should be noted at the outset that while the relationships between the mechanical properties and the mean grain size, carbide volume fraction are known, the influence of grain shape, size distribution, and interface character distribution are not yet clear. Furthermore, it is not clear how changing these microstructural characteristics beyond normally observed ranges alters the properties of the composites.

1.1.4 Applications

The cemented carbides are primarily used as cutting tools. The most wear resistant materials are the straight WC-Co grades which are used for machining and cutting of materials that require abrasion resistance; e.g. cast iron and nonferrous alloys. On the other hand, the alloyed grades are used for strongly yielding materials that require high deformation resistance, toughness, and thermal shock resistance. Also, many applications exist for cemented carbides in non-cutting areas such as mining, construction, and wear resistance components (for example, various types of dies, nozzles, and rolls).

In these cases, the composites are designed to meet the demands of the specific applications which may require impact, abrasion, and/or corrosion resistance.

1.2 Motivations

Like many other engineering materials, the mechanical properties of cemented carbides are strongly influenced by their microstructures. While the qualitative effects of microstructural variables on the mechanical performance are relatively well-understood, the quantitative functional relationships between micro- and macro-features and their fundamental underpinnings are not well-established. This work focuses on a comprehensive analysis of relationships between microstructural and mechanical properties. As microstructural parameters, we include the interface character distribution in WC-Co composites, as well as the conventional factors, such as grain size, size distribution, carbide volume fraction, and the carbide connectivity (contiguity). As a mechanical property parameter, we mainly focus on the fracture strength (transverse rupture strength, TRS) of composites. Only the modeling of fracture strength is included in this thesis because, currently, it is not feasible to numerically approximate other mechanical properties such as hardness and fracture toughness. For the comprehensive understanding of the relationships, it is necessary to develop methods for the accurate measurements of microstructures, characterization of interfaces, and prediction of fracture strengths.

Conventionally, the linear-intercept scheme (an indirect method) has been used to characterize microstructural features in WC-Co composites. This methodology inevitably

involves inaccuracies and limitations in measuring microstructural parameters (see Section 2.3.1 for details). Especially, the linear-intercept method is not able to evaluate the shape of the carbide phase and its angularity. To understand the fundamental interrelations of micro- and macro-features, it is important to establish an accurate and direct microstructural measurement method. This will be a foundation for developing a model that allows one to predict mechanical properties.

A second issue is that most of the previous microstructural measurements have been orientation averaged. In other words, the anisotropic distributions of misorientations and grain boundary planes of these composites have not been explored. To develop a comprehensive description of the microstructure and, to understand the three dimensional shape, a quantitative analysis of interface crystallography (carbide/carbide boundaries, binder/carbide interfaces) is required. During the processing of materials, the thermodynamic driving force for the formation, dissolution, and evolution of microstructures is mainly provided by the excess free energies of interfaces. These energies are, therefore, closely related to the materials performance. However, little is known about the interface crystallography of WC-Co composites. In the case of WC/Co interface character, the equilibrium shape of WC in Co is still the matter of controversy (see Section 2.1.2 for details). Much less is known about WC/WC boundary character distribution, but some transmission electron microscopy (TEM) observations of special boundaries have been reported [5].

Finally, a model that can be used to calculate fracture strengths of hypothetical microstructures would be valuable for the development of new carbide materials. Since the microstructures of hypothetical materials could be controlled to produce nearly

independent variations in the microstructural parameters, the effects on transverse rupture strength (TRS, or equivalently, fracture strength) would be clearly revealed. To test the effects of individual microstructural features, we first have to establish a reliable model to approximate the fracture strength using real microstructures. Although several models have been proposed to simulate fracture mechanisms of WC-Co composites, the application of these previous models has been limited to the calculations of stress-strain distributions in relatively small areas, and the crystallographic anisotropies were not incorporated (see Section 2.6.2 for details). Thus, the development of a reliable model to predict the fracture strength prediction remains a challenge.

1.3 Objectives

Considering the challenges outlined above, the focus of this work is on the quantitative and comprehensive analysis of microstructural features, interface characteristics, and mechanical properties (fracture strength) of straight WC-Co grades. This thesis has the followings goals:

- 1) Establish a reliable method for the accurate measurements of microstructural features of WC-Co composites. From this, specify robust functional relationships between microscopic parameters and macroscopic physical properties.
- 2) Develop a method to analyze the anisotropic distribution of interfaces in WC-Co composites. Then, quantify the distribution of interface types (with respect to the lattice misorientation and boundary plane orientation) in WC-Co composites.

3) Develop a numerical simulation model to predict the fracture strength as a function of quantifiable characteristics of microstructures, and propose WC-Co composite microstructures with improved fracture strengths.

1.4 References

- [1] H.E. Exner, “Physical and Chemical Nature of Cemented Carbides”, *Int. Metal. Rev.*, **4**, 149 (1979)
- [2] J. Gurland, “New Scientific Approaches to Development of Tool Materials”, *Int. Mater. Rev.*, **33**, No.3, 151 (1988)
- [3] B. Roebuck and E.A. Almond, “Deformation and Fracture Processes and the Physical Metallurgy of WC-Co Hardmetals”, *Int. Mater. Rev.*, **33**, No.2, 90 (1988)
- [4] G. Schneider, Jr., Principles of Tungsten Carbide Engineering, 2nd ed., Society of Carbide and Tool Engineers, 1989
- [5] S. Hagege, G. Nouet, and P. Delavignette, “Grain Boundary Analysis in TEM (IV)”, *Phys. Stat. Sol. A*, **61**, 97 (1980)

Chapter 2

Background

This chapter contains background information relevant to this thesis. First, a brief overview of interfaces in WC-Co composites is given. Next, the basic crystallography and microstructures of the composites are described. This is followed by a short review of the mechanical properties, fracture mechanisms and empirical microstructure-property relationships for the composites. Finally, finite element models (FEM) for stress-strain field calculations, with their capabilities and applications, are presented.

2.1 Shapes of carbide particles

2.1.1 Anisotropy

Cemented carbides are sintered in the presence of a liquid Co phase. During processing, the characteristic carbide microstructure is formed by coarsening. In the coarsening, WC dissolves from relatively smaller crystals, diffuses through the liquid Co, and precipitates on relatively larger crystals. Both the interfacial energies and attachment/detachment at the solid (WC)/liquid (Co) interface affect the shapes of the WC crystals that grow and shrink during the coarsening process.

Interfacial energy can be defined as the work that must be done to create a unit area of an interface at constant T , P , and μ (temperature, pressure, and chemical potential, respectively). In solid materials, the interfacial energy is affected by the crystal structure

(number of broken bonds, interplanar spacing, and the charge balance of cations and anions in ionic compounds). While the symmetry of the interfacial energy is normally same as that of the crystal structure, surface polarity can generate additional anisotropy [1]. WC has a hexagonal crystallographic structure with two atoms (W and C) per unit cell as illustrated in Fig. 2.1. The lattice constants are $a=2.906 \text{ \AA}$ and $c=2.837 \text{ \AA}$ with $c/a=0.976$ [2, 3].

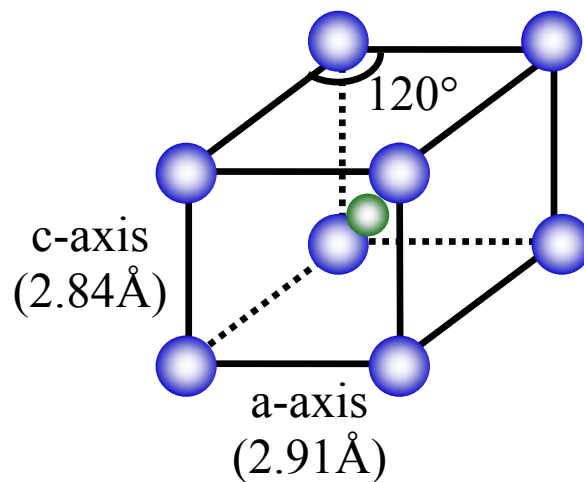
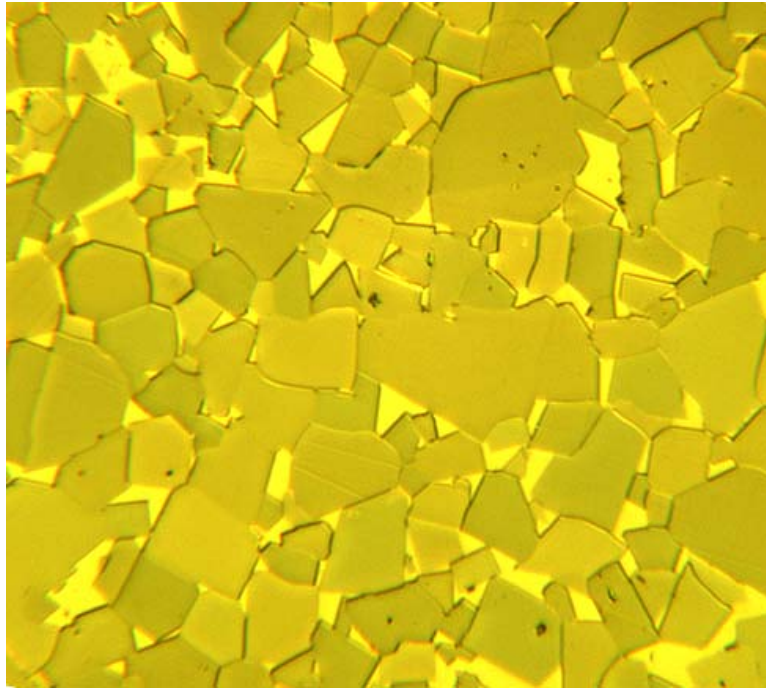


Fig. 2.1 : Crystal structure of WC. Blue and green denote W and C atoms, respectively. W atoms are at $(0, 0, 0)$ and C atoms are at $(1/2, 2/3, 1/2)$ positions in the WC unit cell.

A typical optical micrograph of a straight grade WC-Co composite is shown in Fig. 2.2 (10 Co v/o, grade A in Chapter 3-5). It is clear that the WC surfaces are faceted when WC is embedded in Co. While alloyed cemented carbides frequently display more spherical (or rather rough) WC grains, WC particles in straight WC-Co grades invariably exhibit angular shapes. Based on this angular character of WC particles, it is thought that the WC/Co interfaces possess strong anisotropies and WC crystals have well-defined habit planes.



20 μm

Fig. 2.2 : A typical optical micrograph of WC-Co composites (from specimen grade A in Chapter 3-5). Dark yellow contrasts represent WC grains and bright yellow contrast denotes Co phase. In composites, there are two different types of interfaces: WC/Co interface and WC/WC grain boundaries.

2.1.2 Equilibrium shape of WC crystals in a Co binder

The carbide/carbide and binder/carbide interfacial energies have not yet been quantitatively measured. By wetting experiments, it has been reported that the liquid Co completely wets the WC crystals [4-6], indicating that the average binder/carbide interfacial energy is much lower than the average carbide/carbide interfacial energy.

Previously, from observations of deeply etched samples, the shapes of WC particles in a Co binder have been identified both a trigonal prism with three prismatic

and two basal facets (see Fig. 2.3(a)), or a truncated trigonal prism where some of the corners or edges of the trigonal prism are replaced by new facets (see Fig. 2.3(b)) [4, 7-10]. From these results, the (0001) basal and $(10\bar{1}0)$ prismatic facets of the carbide phase are considered to have relatively low interface energy in contact with Co. In all of the cases of the past studies, however, the shapes of WC in a Co binder were derived from qualitative observations. Thus, the quantitative aspect ratios (base-to-height ratio of prism facet) of the crystals have not been measured. Furthermore, since deep etching can not reveal the full three dimensional shape, it is impossible to know which faces were actually created by impingement at a part of the crystal already removed by polishing or below the level of the etch.

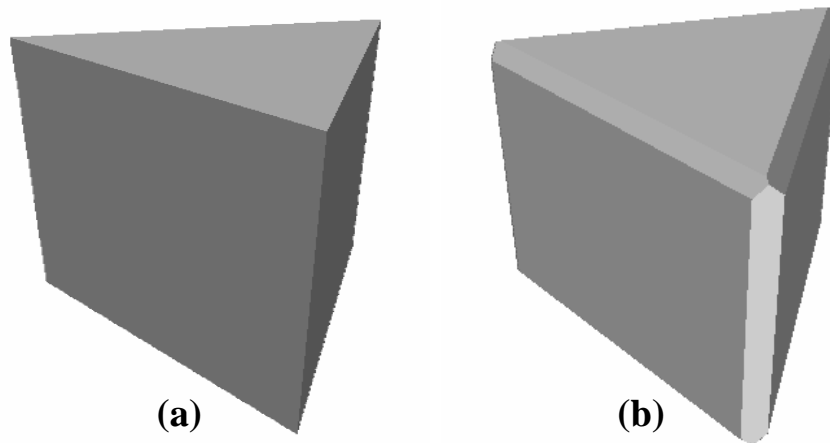


Fig. 2.3 : Proposed equilibrium shapes of WC crystals. (a) Prism shape, (b) prism with truncated edge shape.

Wulff plot

If a particle (or a grain) adopts the equilibrium shape, a Wulff plot (or γ plot) can be used to estimate WC/Co interfacial energy anisotropies. In a Wulff plot (see Fig.

2.4(a)), the direction of the vector to a specific point on the polar plot represents the orientation of the interface, and the magnitude of the vector indicates the relative value of the interfacial energy at that particular orientation. The equilibrium shape is given by the inner envelope of planes perpendicular to each orientation vector (the shaded area in Fig. 2.4(b)). Highly angular WC particle shapes indicate that there should be deep cusps (singularities) in the WC/Co interfacial energy contour, and that there are missing orientations in the WC equilibrium form. It is not clear that the WC crystals in WC-Co composites are equilibrium shapes. The observed WC shapes in these composites are influenced by the mechanisms of dissolution/growth that occur during coarsening and by the impingements of carbide crystals.

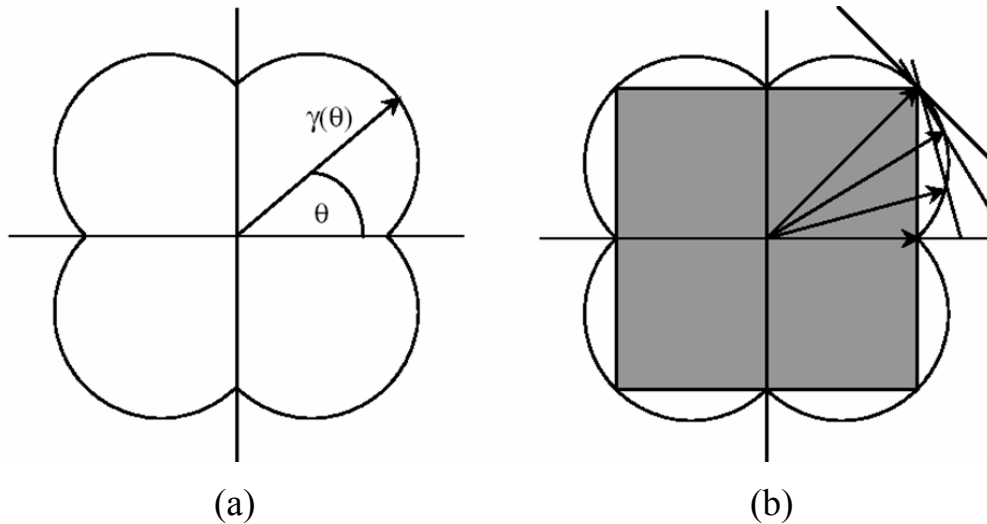


Fig. 2.4 : (a) Schematic illustration of Wulff plot. Surface energy vector, $\gamma(\theta)$, represents the relative surface energy at a specific orientation θ . (b) The corresponding Wulff construction. The inner envelope (shaded area) formed by the normals to surface energy vectors is the equilibrium shape.

2.2 Carbide/carbide boundaries

2.2.1 Basic crystallography

i) Orientation representation

Coordinate system transformations

Physically, there are two reference frames to describe the orientations of grains in polycrystals. They are laboratory (or sample) reference frame and crystal reference frame (see Fig. 2.5, laboratory frame in red, crystal frame in blue). In this document, interfaces will be represented in the crystal reference frame. To transform the laboratory coordinate frame to the crystal coordinate frame, we use three Euler angles (ϕ_1 , Φ , ϕ_2) which define a sequence of rotations from one reference frame to the other reference frame. If \hat{x}_i denote a basis unit vector in laboratory coordinates, we need three consecutive rotations ($\hat{x}_i \rightarrow \hat{x}_i' \rightarrow \hat{x}_i'' \rightarrow \hat{x}_i'''$, where \hat{x}_i''' denote a basis unit vector in crystal coordinates, and \hat{x}_i' and \hat{x}_i'' stand for a basis unit vector in some intermediate coordinates between the laboratory and crystal frames) using the three Euler angles (see Fig. 2.6); \hat{x}_i yields \hat{x}_i' by a rotation of ϕ_1 about \hat{x}_3 axis, \hat{x}_i' yields \hat{x}_i'' by a rotation of Φ about \hat{x}_1' axis, and \hat{x}_i'' yields \hat{x}_i''' by a rotation of ϕ_2 about \hat{x}_3'' axis. Here, the Euler angle notation is that of Bunge's [11]. Using these three successive rotations, it is possible to construct one transformation matrix (g), which converts the laboratory coordinate system to crystal coordinate system. It is given by [11]:

$$g(\phi_1, \Phi, \phi_2) = \begin{bmatrix} c\phi_1c\phi_2 - s\phi_1s\phi_2c\Phi & s\phi_1c\phi_2 + c\phi_1s\phi_2c\Phi & s\phi_2s\Phi \\ -c\phi_1s\phi_2 - s\phi_1c\phi_2c\Phi & -s\phi_1s\phi_2 + c\phi_1c\phi_2c\Phi & c\phi_2s\Phi \\ s\phi_1s\Phi & -c\phi_1s\Phi & c\Phi \end{bmatrix} \quad (2.1)$$

where c and s represent cosine and sine, respectively.

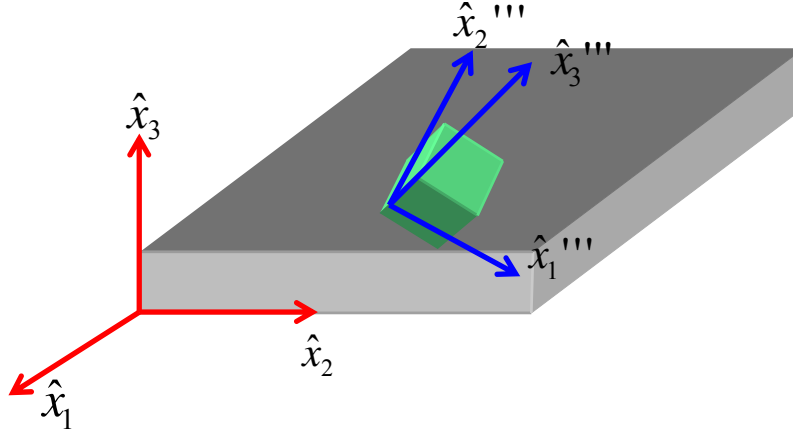


Fig. 2.5 : Illustration of the laboratory coordinate system (red) and crystal coordinate system (blue). \hat{x}_i, \hat{x}_i''' represent unit vectors in the laboratory and crystal reference frames, respectively.

Fundamental zone (Standard triangle, unique triangle)

If we ignore the multiplicity of a special position (a position which contains symmetry elements such as rotation axis, mirror plane, and/or inversion center), there are 24 symmetrically equivalent orientations in a hexagonal crystal system (e.g. $6/mmm$ point group) [12]. In case of a cubic crystal system (e.g. $m\bar{3}m$ point group), the number of equivalent orientations of a general position (a position that does not lie on a symmetry element) increases to 48 [12]. Because of symmetry, any orientation can be described in a fundamental zone (the smallest unit of a crystal system that contains all distinguishable orientations). The fundamental zone of the hexagonal system is given in the $[0001]$

stereographic projection shown in Fig. 2.7. The choice of a fundamental zone is arbitrary, and, in this work, the shaded region will be used as the fundamental zone of WC crystal.

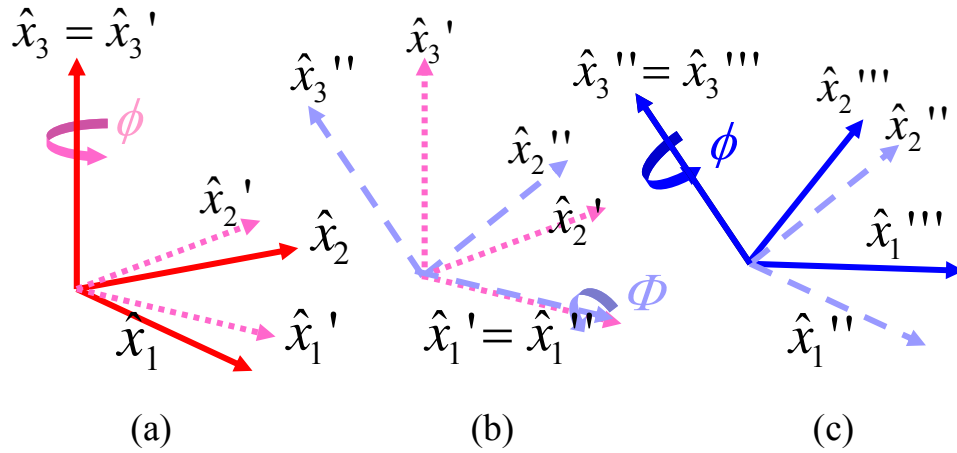


Fig. 2.6 : Schematic representation of transformation from the laboratory (red) coordinate to crystal (blue) coordinate system. (a) Rotation from the laboratory coordinate system, \hat{x}_i , to a new coordinate system, \hat{x}_i' (pink), (b) rotation from \hat{x}_i' to another new coordinate system, \hat{x}_i'' (purple), (c) rotation from \hat{x}_i'' to the crystal coordinate system, \hat{x}_i''' .

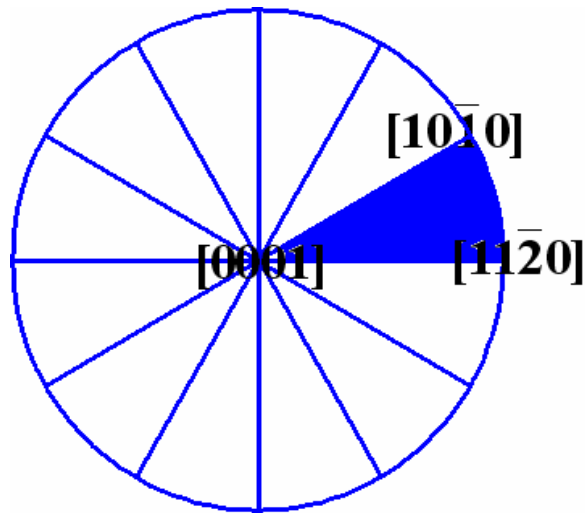


Fig. 2.7 : A [0001] stereographic projection of hexagonal systems. The shaded area represents an example of the fundamental zone.

Pole figure (PF)

Crystal orientations are usually plotted as two-dimensional stereographic projections in pole figures (PF). A pole figure (PF) shows the position of a crystal pole relative to the laboratory reference frame. For example, in a (0001) pole figure of a polycrystal with a hexagonal symmetry, the axes on the stereographic projection indicate directions in the laboratory coordinate system, and the positions of poles represent vectors normal to the (0001) plane of a given crystal with respect to the laboratory reference frame. Such pole figures are usually used for the analysis of the crystal orientation distributions (orientation texture).

Inverse pole figure (IPF)

An inverse pole figure (IPF) shows the position of a sample direction relative to the crystal reference frame. Since the IPF has the symmetry of the crystals, it can be plotted in a fundamental zone. Pole figures, on the other hand, have only the symmetry of the sample (usually taken to be an orthorhombic system) and are typically plotted on the complete stereographic projection of a hemisphere. In a (0001) IPF, the indices in a fundamental zone describe a direction in the crystal coordinate system, and the positions of poles denote the crystal direction (in the crystal reference frame) that is aligned with the sample normal.

ii) Grain boundary representation

To describe the type or character of a grain boundary, five independent macroscopically observable parameters are required. The first three describes the

misorientation of a bicrystal and the last two identifies the grain boundary plane. For numerical calculations used in this research, the lattice misorientation is specified by the three Euler angles (ϕ_1, Φ, ϕ_2) , and the two parameters that determine the boundary planes are specified by the two spherical angles (ϕ, θ) . Other possible choices for the misorientation representations are the axis-angle descriptions (either in an axis-angle space or in a Rodrigues space), which will also be used to display and discuss the results. The grain boundary distribution is usually represented by the notation $\lambda(\Delta g, \mathbf{n})$, which is the relative occurrence of a grain boundary with a misorientation, Δg , and a grain boundary plane normal, \mathbf{n} , in a unit of multiples of a random distribution (MRD).

Misorientations

The lattice misorientation (Δg_{ab}) across the boundary is calculated from the orientations of individual adjoining crystals (g_a and g_b). To bring crystal b into coincidence with crystal a , two successive transformations are specified; first, crystal b is transformed into laboratory coordinates (g_b^T), and then transformed to the frame of crystal a (g_a). Therefore, the overall transformation matrix becomes [11]:

$$\Delta g_{ab} = g_a g_b^T \quad (2.2)$$

where g_b^T denotes the transpose of matrix g_b . From Eq. (2.2), the misorientation angle (ϖ) and the vector components of misorientation (\mathbf{n}_i) can be calculated by following equations [11]:

$$\varpi = \cos^{-1} \left(\frac{\Delta g_{ii} - 1}{2} \right) \quad (2.3)$$

$$\mathbf{n}_i = -\frac{\varepsilon_{ijk} \Delta g_{jk}}{2 \sin \omega} \quad (2.4)$$

where ε_{ijk} is the permutation tensor.

Misorientation distributions in Euler space

Misorientations can be represented in terms of three Euler angles ($\Delta\phi_1, \Delta\Phi, \Delta\phi_2$). Here, the three Euler angles are defined by the consecutive rotation angles to transform from a crystal reference frame to another crystal reference frame. An example of misorientation distributions in WC/WC grain boundaries (specimen grade A, Chapter 3-5) using the Euler space is shown in Fig. 2.8. Variations of WC/WC boundary misorientation distributions along $\Delta\phi_1$ and $\Delta\Phi$ are illustrated in one square section with a specific $\Delta\phi_2$. Distribution scales are represented as multiples of a random distribution (MRD). The distribution in Fig. 2.8 is for the visualization purpose, not for the analysis of the data (Fig. 2.9 and 2.10 also for the descriptions of axis-angle and Rodrigues spaces only). The overall transformation matrix, Δg , is same as Eq. (2.1), except the Δ notations:

$$\Delta g = \begin{bmatrix} c\Delta\phi_1 c\Delta\phi_2 - s\Delta\phi_1 s\Delta\phi_2 c\Delta\Phi & s\Delta\phi_1 c\Delta\phi_2 + c\Delta\phi_1 s\Delta\phi_2 c\Delta\Phi & s\Delta\phi_2 s\Delta\Phi \\ -c\Delta\phi_1 s\Delta\phi_2 - s\Delta\phi_1 c\Delta\phi_2 c\Delta\Phi & -s\Delta\phi_1 s\Delta\phi_2 + c\Delta\phi_1 c\Delta\phi_2 c\Delta\Phi & c\Delta\phi_2 s\Delta\Phi \\ s\Delta\phi_1 s\Delta\Phi & -c\Delta\phi_1 s\Delta\Phi & c\Delta\Phi \end{bmatrix} \quad (2.5)$$

where c and s represent cosine and sine, respectively.

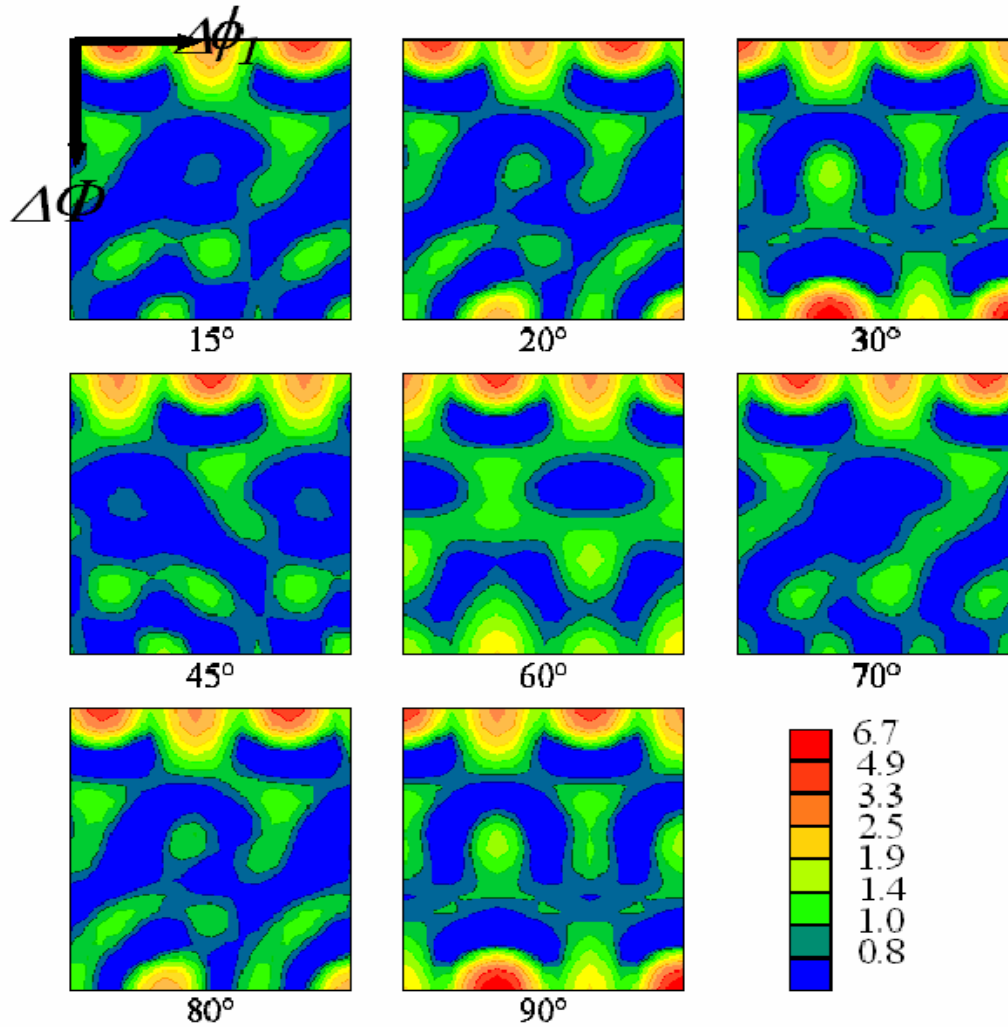


Fig. 2.8 : Example of misorientation distributions in Euler space (from grade A, Chapter 3-5). Scales are multiples of a random distribution (MRD). $\Delta\phi_2$ is specified at each section.

Misorientation distributions in axis-angle space

Another way to describe misorientation distributions is to use misorientation axis-angle pairs. Any misorientation can be specified by a set of the smallest misorientation angle (disorientation angle, Eq. (2.3)) and misorientation axis (Eq. (2.4)). Because every misorientation can be represented by the crystallographically equivalent axis-angle pair with the minimum misorientation angle, the maximum misorientation angle is bounded;

the upper limit depends on the crystal system. For example, the maximum misorientation angles are $\sim 63^\circ$ in a cubic system and $\sim 98^\circ$ in a hexagonal system. In Fig. 2.9, an example of misorientation distributions for WC/WC boundaries (same data set used in Fig. 2.8, data from grade A in Chapter 3-5) is illustrated in axis-angle space. Each standard triangle contains the misorientation axis distributions at a specific misorientation angle.

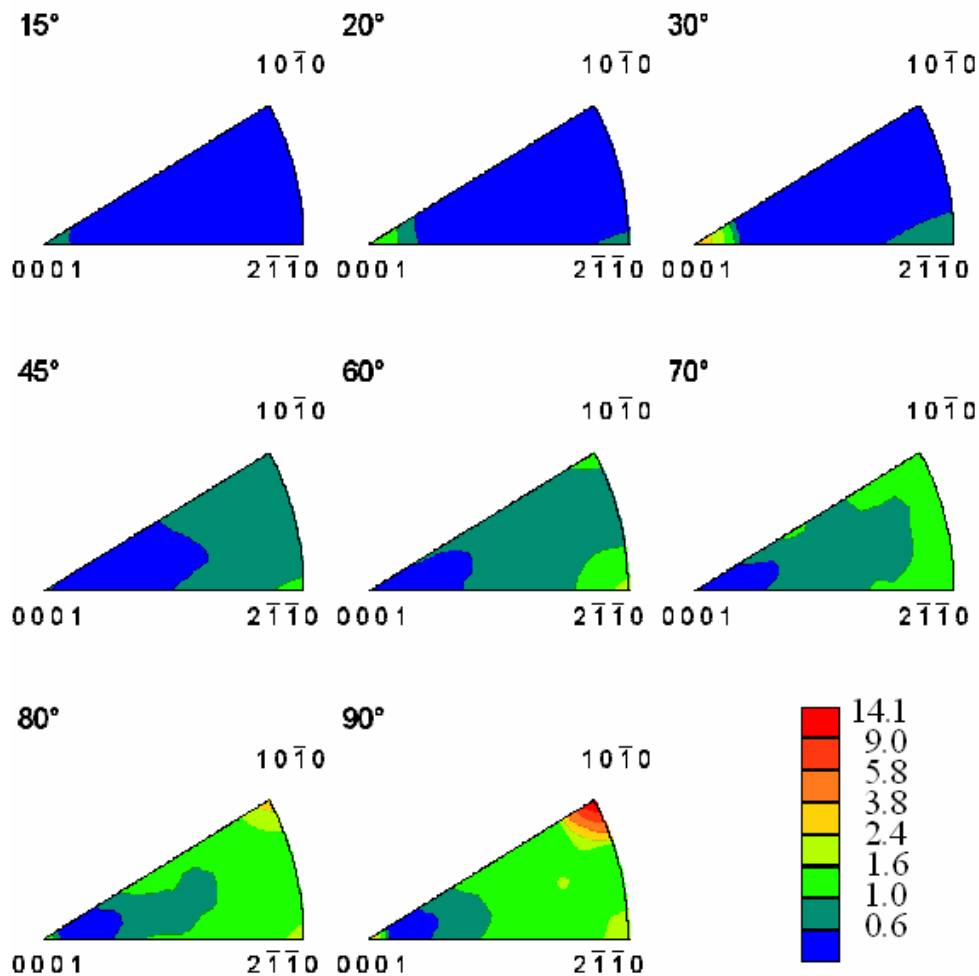


Fig. 2.9 : Example of misorientation distributions in axis-angle space (from grade A, Chapter 3-5). Scales are multiples of a random distribution (MRD). Misorientation angle is specified at each section.

Misorientations in Rodrigues space

The representation of misorientation in Rodrigues space was first considered by Heinz and Neumann [12], followed by Morawiec and Field [13]. A Rodrigues vector is defined by:

$$\mathbf{r}_i = \tan\left(\frac{\omega}{2}\right)\mathbf{n}_i \quad (2.6)$$

where \mathbf{r}_i is the Rodrigues vector, ω is the misorientation angle, and \mathbf{n}_i is the misorientation axis. Euler angle (in Euler space) and Rodrigues vector (in Rodrigues space) parameterizations are useful for the representations of orientation distributions as well as misorientation distributions. An example of misorientation distributions of WC/WC boundaries (same data set used in Fig. 2.8 and Fig. 2.9, data from grade A in Chapter 3-5) is depicted in Fig. 2.10. Here, x , y , and z axes (in Cartesian coordinate) correspond to the \mathbf{r}_1 , \mathbf{r}_2 , and \mathbf{r}_3 vectors, respectively.

Tilt and twist boundaries

A boundary is commonly described in terms of tilt and twist components. A tilt boundary is defined as a boundary in which the misorientation axis lies in the boundary plane and a twist boundary is one in which the misorientation axis is perpendicular to the boundary plane. In real microstructures, most grain boundaries have mixed characteristics of pure tilt and twist components. Examples of pure tilt and twist boundaries are illustrated in Fig. 2.11 (a) and (b).

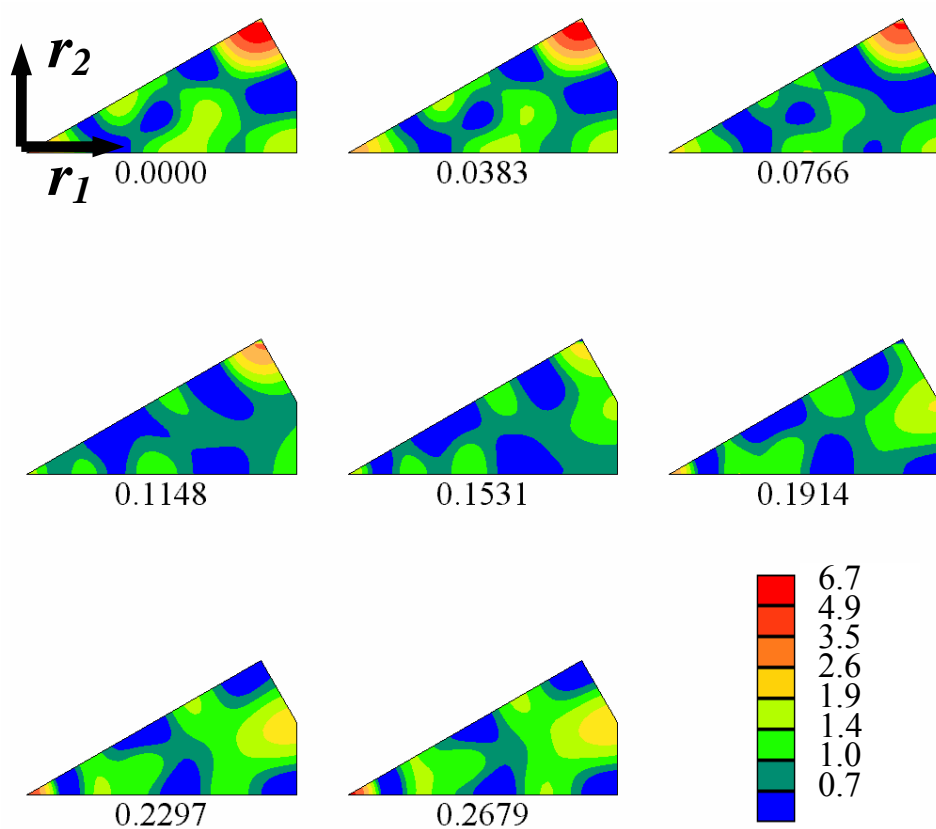


Fig. 2.10 : Example of misorientation distributions in Rodrigues space (data from grade A, Chapter 3-5). Scales are multiples of a random distribution (MRD). Magnitude of r_3 vector is specified at each section.

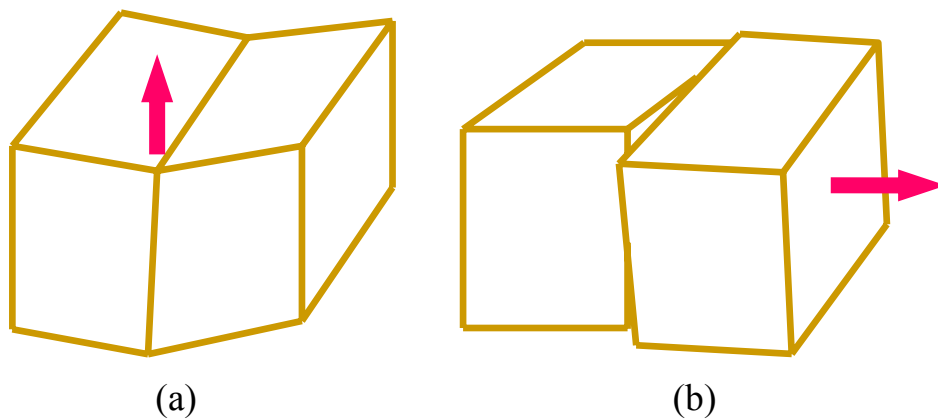


Fig. 2.11 : Schematic illustration of the pure tilt and twist boundaries. (a) Pure tilt, (b) pure twist. The pink arrow represents the misorientation axis.

Coincidence site lattice (CSL) boundaries

When a finite fraction of lattice sites coincide between the two adjacent crystal lattices, then the boundary is called as a coincidence site lattice (CSL) boundary. It is widely believed that this coincidence leads to a reduction in the interfacial energy, especially in the case of high angle boundaries. However, this hypothesis is not always consistent with observations. The CSL boundaries are described by a quantity Σ , the reciprocal ratio between the areas enclosed by a unit cell of the coincidence sites; as the Σ value decreases, the fraction of coincident sites increases. This occurs only for special boundary planes, and only in these cases, we do expect any effect on the grain boundary energy. Fig. 2.12 illustrates examples of the pure twist $\Sigma 5$ and $\Sigma 13$ CSL boundaries in a simple cubic (SC) crystal.

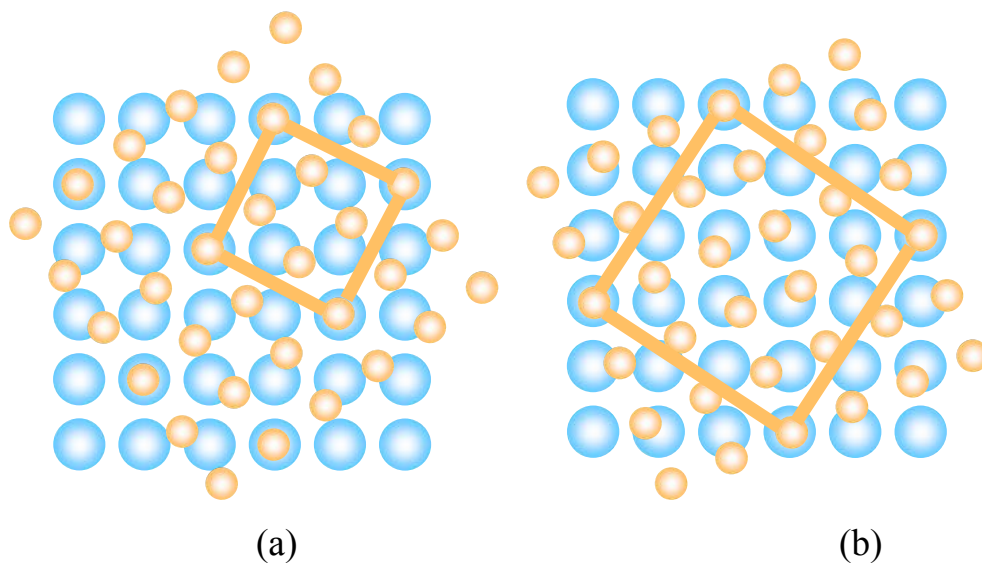


Fig. 2.12 : Schematic illustration of CSL boundaries in superimposed simple cubic crystals. (a) Twist $\Sigma 5$ boundary (misorientation angle=36.86°), (b) Twist $\Sigma 13$ boundary (misorientation angle=22.62°). The orange square in each figure leads a low Σ CSL boundary.

iii) Texture

The texture, $A(g, \Delta g, \mathbf{n})$, is defined as the relative frequency of occurrence of a orientation, g , misorientation, Δg , and/or grain boundary plane normal, \mathbf{n} , in units of multiples of a random distribution (MRD). If there is a preferred crystal orientation with respect to sample reference frame, it is usually referred to as a texture. Preferred misorientations with respect to the bicrystal reference frame are called misorientation textures. And, preferred grain boundary planes with respect to the crystal reference frame are called grain boundary plane textures. Schematic illustrations of these three textures are presented in Fig. 2.13~15. We shall see that there are strong misorientation and grain boundary plane texture in WC/WC boundaries of WC-Co composites (see Chapter 4).

Orientation texture

Orientation texture is described by the preferred orientations of crystals with respect to sample reference frame. It is usually specified by the orientation distribution function (ODF), $A(g)$, in units of MRD. Fig. 2.13 (a) and (b) represent the microstructures without and with orientation textures when the colors and arrows denote the orientations and a certain plane normal direction type (for example, $\langle 110 \rangle$) of individual grains, respectively. It is known that this orientation texture can reduce the stress and stored energy distributions in polycrystalline materials under a thermal load. The effect of orientation texture on the strength of WC-Co composites will be discussed in Section 5.4.3 ii).

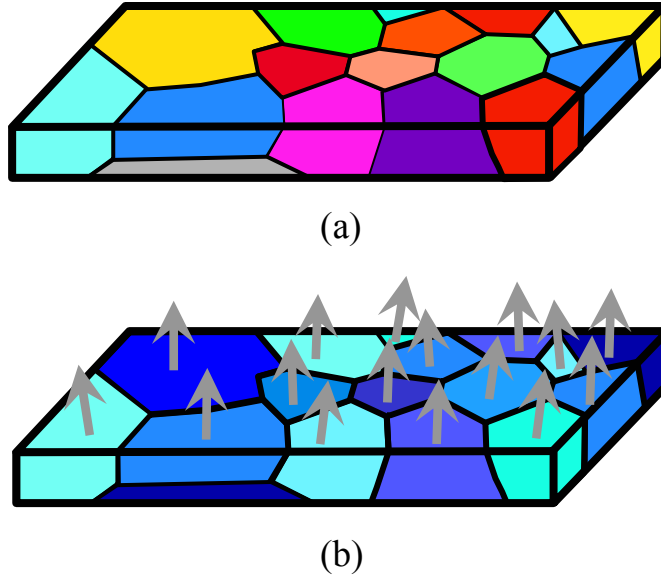
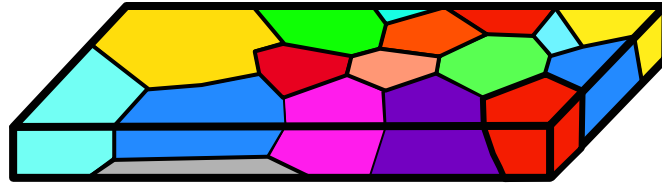


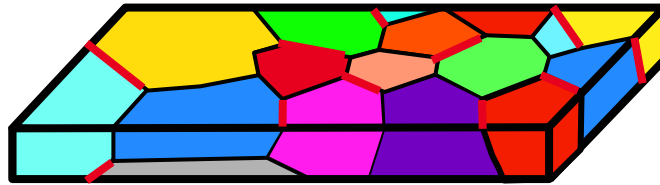
Fig. 2.13 : Illustrations of orientation texture ($\Delta(g)$). Grain colors correlate with orientations. (a) Polycrystals without orientation texture, (b) polycrystals with orientation texture.

Misorientation texture

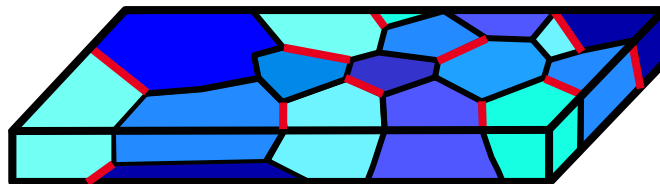
If grain boundaries tend to have specific misorientations (specific misorientation axis-angle pairs), then the microstructures are said to have misorientation textures. It is commonly described by the misorientation distribution function (MDF), $\Delta(\Delta g)$, in units of MRD. Examples of the misorientation texture in WC-Co composites are given in Fig. 2.8~2.10. In those figures, high MRD values are found at specific misorientations. There can be misorientation textures regardless of the existence of orientation textures. If the red bold lines in Fig. 2.14 (b) and (c) indicate a specific misorientation (for example, 60° about $\langle 111 \rangle$), then the polycrystals show microstructures with misorientation textures, (b) without misorientation texture, and (c) with orientation texture.



(a)



(b)



(c)

Fig. 2.14 : Illustrations of misorientation texture ($\Lambda(\Delta g)$). Red grain boundaries denote a specific same misorientation. (a) Poly crystals with no orientation, no misorientation texture, (b) polycrystals with no orientation, but with misorientation texture, (c) polycrystals with orientation and misorientation texture.

Grain boundary plane texture

While misorientation textures in a polycrystalline material identify the existence of preferred misorientations, grain boundary plane textures can be regarded as the presence of preferred boundary planes between adjacent crystals in a polycrystal. The grain boundary texture, $\Lambda(\mathbf{n})$, is only the function of a grain boundary plane normal, \mathbf{n} . Also, grain boundary texture can develop in the absence of orientation and misorientation textures. An example of a grain boundary plane textured polycrystal (without orientation

texture) is illustrated schematically in Fig. 2.15, where the red grain boundary planes stand for a specific type of orientation (for example, $\{100\}$).

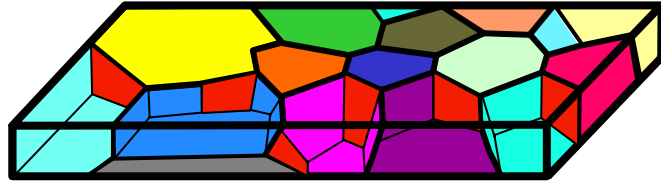


Fig. 2.15 : Illustration of grain boundary plane texture ($\Lambda(n)$). Red grain boundaries have a specific orientation, $\{hkl\}$, in the crystal reference frame. Grain boundary texture can develop in the absence of orientation and misorientation texture.

2.2.2 Character of carbide/carbide grain boundaries

In WC-Co composites, there are binder/carbide interfaces and carbide/carbide grain boundaries. Therefore, one can assume that the microstructure consists of a contiguous carbide phase and an isolated binder phase. This is the so called ‘skeletonized carbide’ model [15]. However, it has been reported that carbide/carbide boundaries invariably contain cobalt as a submonolayer segregant implying that carbide particles are dispersed in a continuous binder phase. In the current literature, this is referred to as the ‘dispersed carbide’ model [16, 17]. Whether the carbide/carbide boundary has thin binder layer or not, little is known about the crystallographic character of carbide/carbide boundaries. From the transmission electron microscopy (TEM) analysis, Hagege et al. [18] observed a 90° twist boundary about $[10\bar{1}0]$, which is related to a low Σ CSL boundary (near $\Sigma 2$). Based on the inhomogeneous distribution of observed dihedral angles between contiguous WC grains, Deshmukh and Gurland [19] proposed that certain grain boundaries are not penetrated by Co and, therefore, occur with a higher frequency.

Although they only examined only 10 carbide/carbide boundaries, they showed, qualitatively, a tendency toward high coincidence contacts between carbide particles (7 of 10 carbide/carbide boundaries were low Σ CSL boundaries). One of the goals of this thesis is to quantitatively specify the relative population of the carbide/carbide grain boundaries.

2.3 Measurements of microstructural parameters

2.3.1 Linear-intercept analysis

In past studies, three parameters have been used to characterize the microstructure and correlated to the mechanical properties of WC-Co composites; the volume fraction of each phase, the average particle size of each of the phases, and the contiguity of carbide phase. In addition to these three common microstructural parameters, the angularity of the carbide phase is also considered to be a crucial factor. Conventionally, these microstructural parameters have been characterized by a combination of point and linear analysis (the linear-intercept analysis method) on scanning electron microscopy (SEM) images. Although the linear-intercept method has the merits of providing information on the volume fraction, size distribution, and contiguity, it also has several limitations. Most importantly, grain shape and area cannot be estimated by this method. And, for statistically reliable results, on the order of 10^3 observations need to be recorded and analyzed. Finally, it is not possible to specify the angularity of the WC phase by the linear-intercept method.

2.3.2 Microstructural parameters

i) Volume fraction

It is a common practice to specify the composition of WC-Co hard materials in terms of weight percent (w/o), but the use of volume percent (v/o) is more informative, since some of the W and C atoms are dissolved in the Co binder [20]. The densities of Co-W-C solid solutions vary from 8.8 to 9.5 g/cm³ with W and C contents. The volume fraction of each phase is the most important factor for determining the mechanical properties of WC-Co composites. As the volume fraction of the carbide phase increases, hardness increases and fracture toughness decreases. The volume fractions of the carbide and binder phase can be obtained from random point counting with at least 10³ counting points.

$$f_c = \frac{N_c}{N_b + N_c} \quad (2.7)$$

in which, f_c is the volume fraction of carbide phase, and N_b , N_c are the numbers of point counts in binder, and carbide phases, respectively.

ii) Particle size and size distribution

Particle size and size distribution also affect the properties of WC-Co composites. This includes the Co binder mean free path and the distribution of free paths, as well as the average size and the size distribution of the carbide particles. Like other engineering materials, the qualitative effect of particle size on the materials performance is well-established. Fine-grained grades give rise to high hardness and low fracture toughness,

and coarse-grained grades produce low hardness and high toughness. The average carbide particle size and binder mean free path can be calculated from the following linear-intercept equations using stereological principles [21].

$$L^* = \frac{2f_c}{2N_{cc} + N_{bc}} \quad (2.8)$$

$$\lambda_1^* = L^* \times \frac{1-f_c}{f_c(1-C)} \quad (2.9a)$$

$$\lambda_2^* = L^* \times \frac{1-f_c}{f_c} \quad (2.9b)$$

where L^* is the average carbide particle size, N_{cc} and N_{bc} are the average numbers of intercepts per unit length of test line with traces of carbide/carbide boundary and binder/carbide interface, λ^* is the binder mean free path, and C is the contiguity of carbide phase. Note that there are two distinct expressions for the binder mean free path; one contains the contiguity factor in the denominator (Eq. (2.9a)), and the other does not (Eq. (2.9b)). Only one of these expressions can be correct.

iii) Contiguity of carbide phase

The contiguity (C) of carbide phase can be defined as the ratio of the carbide/carbide interface area to the total interface area [22, 23]. The degree of contiguity greatly influences the properties of composites, particularly if the properties of the constituent phases differ significantly. Contiguity ranges from 0 to nearly 1 as the distribution of the carbide phase changes from a totally dispersed to a completely agglomerated structure in the liquid phase. The extent of continuity is primarily

determined by the volume fractions. Generally, the contiguity is higher in high carbide volume fraction grades than in low carbide volume fraction grades. From this, it can be imagined that the effects of contiguity on the mechanical properties is similar to that of the carbide volume fraction. As the contiguity increases, hardness increases and fracture toughness decreases. It has been reported that the degree of contiguity is also affected by the carbide particle size; increasing carbide particle size is thought to decrease contiguity [7]. Some authors suggested that the contiguity is also determined by the sintering time, and that it is independent of grain size [22, 23]. The contiguity of the carbide phase can be determined using a linear-intercept analysis by the following formula [21],

$$C = \frac{2N_{cc}}{2N_{cc} + N_{bc}} \quad (2.10)$$

iv) Angularity of carbide phase

Angularity has been used quantitatively to describe the degree of faceting in the carbide grains. Therefore, it is thought to be related to the surface energy anisotropy and/or the anisotropy of growth rates. To our knowledge, the angularity of the carbide phase has not previously been quantified and related to the properties of WC-Co composites. This is probably because it is not possible to estimate angularity using linear-intercept analysis. Non-angular WC-Co composite grades are thought to have undesirable mechanical properties, although the actual effect of angularity has not been quantified.

2.4 Mechanical behavior of WC-Co composites

2.4.1 Elastic stress and stored energy

i) Stress invariant and strain invariant

Stresses (σ_{ij}) and strains (ϵ_{ij}) are 2nd rank tensors (see Eq. 2.11). In the stress and strain tensors, the first subscript denotes the normal of plane and the second subscript stands for the direction of forces. Fig. 2.16 schematically illustrates the stress tensor.

$$\sigma_{ij} = \begin{bmatrix} \sigma_{11} & \sigma_{12} & \sigma_{13} \\ \sigma_{21} & \sigma_{22} & \sigma_{23} \\ \sigma_{31} & \sigma_{32} & \sigma_{33} \end{bmatrix}, \epsilon_{ij} = \begin{bmatrix} \epsilon_{11} & \epsilon_{12} & \epsilon_{13} \\ \epsilon_{21} & \epsilon_{22} & \epsilon_{23} \\ \epsilon_{31} & \epsilon_{32} & \epsilon_{33} \end{bmatrix} \quad (2.11)$$

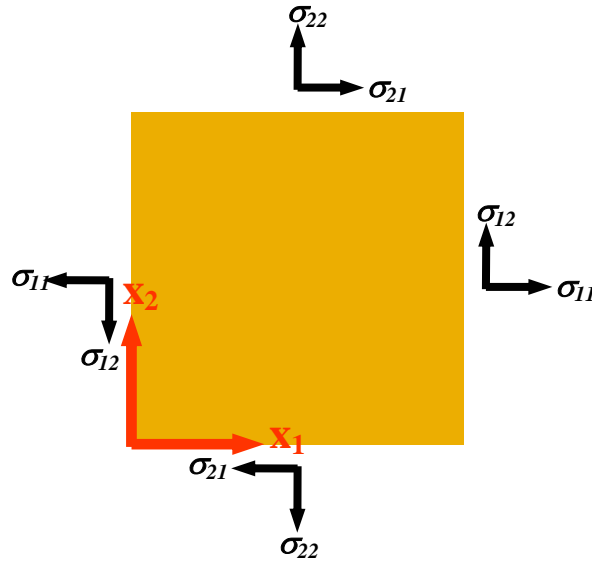


Fig. 2.16 : Schematic illustration of stress tensor. Only x (x_1) and y (x_2) components are shown.

The stress vector at any point, $t_j = \sigma_{ij}n_i$, can be transformed to ‘principal stress’ (whose off-diagonal components are all zero) by taking principal stress directions (n_i') as a basis for a new coordinate system.

$$t_j = \sigma_{ij}n_i = \begin{bmatrix} \sigma_{11} & \sigma_{12} & \sigma_{13} \\ \sigma_{21} & \sigma_{22} & \sigma_{23} \\ \sigma_{31} & \sigma_{32} & \sigma_{33} \end{bmatrix} \begin{bmatrix} n_1 \\ n_2 \\ n_3 \end{bmatrix} \leftrightarrow \begin{bmatrix} \sigma_1 & 0 & 0 \\ 0 & \sigma_2 & 0 \\ 0 & 0 & \sigma_3 \end{bmatrix} \begin{bmatrix} n_1' \\ n_2' \\ n_3' \end{bmatrix} \quad (2.12)$$

where t_j is the stress vector, n_i is the basis vector, $(\sigma_1, \sigma_2, \sigma_3)$ is principal stress, and n_i' is the basis for a new coordinate system. In seeking these principal stresses, the three stress invariants can be determined by:

$$\begin{aligned} I_1 &= \sigma_1 + \sigma_2 + \sigma_3 \\ I_2 &= -(\sigma_1\sigma_2 + \sigma_2\sigma_3 + \sigma_3\sigma_1) \\ I_3 &= \sigma_1\sigma_2\sigma_3 \end{aligned} \quad (2.13)$$

where I_1, I_2, I_3 are the three stress invariants. The detailed description for deriving stress invariants (Eq. (2.13)) can be found elsewhere [24, 25]. In Chapter 5, the stress invariant 1 (I_1) distributions are frequently presented for the analysis of the stress state in WC-Co composites.

Similarly, the strain invariants are given by:

$$\begin{aligned} I_1' &= \varepsilon_1 + \varepsilon_2 + \varepsilon_3 \\ I_2' &= -(\varepsilon_1\varepsilon_2 + \varepsilon_2\varepsilon_3 + \varepsilon_3\varepsilon_1) \\ I_3' &= \varepsilon_1\varepsilon_2\varepsilon_3 \end{aligned} \quad (2.14)$$

where I_1' , I_2' , I_3' are the three strain invariants, ε_1 , ε_2 , and ε_3 are the principal strains along 1, 2, and 3 principal strain directions.

ii) Elastic energy density

The elastically stored strain energy (u , elastic strain energy per unit volume) is important because it influences the amount of external work that must be done to initiate failure by a brittle fracture mechanism. This will be described in more detail in Chapter 5. The stored energy is calculated in the following way:

$$u = \frac{1}{2} \sum_{i,j} \sigma_{ij} \varepsilon_{ij} \quad (i,j=1,2,3) \quad (2.15)$$

2.4.2 Elastic and plastic behaviors

WC-Co composites are composed of a brittle carbide phase and a ductile binder phase. Elastic and plastic behaviors can be described by the linear and non-linear responses to applied stresses. Whereas fracture in ductile materials often involves in the energy absorption during the plastic deformation, failure in brittle materials occurs at the elastic regime. The composites of interest here contain both types of materials, and both failure mechanisms are thought to occur.

i) Elastic constants

In an elastic deformation regime, the elastic strain is usually found to be proportional to the applied stress, which can be expressed by the simple Hooke's law (one dimensional case):

$$\sigma = E\varepsilon \quad (2.16)$$

where σ is the applied stress, ε is the strain, and the proportionality E is Young's modulus of elasticity. The generalized form of Hooke's law accounts for the three dimensional anisotropic linear response to the applied stresses:

$$\sigma_{ij} = C_{ijkl} \varepsilon_{kl} \quad (i,j,k,l=1,2,3) \quad (2.17a)$$

$$\varepsilon_{ij} = S_{ijkl} \sigma_{kl} \quad (i,j,k,l=1,2,3) \quad (2.17b)$$

where σ_{ij} is the stress tensor (2nd order), ε_{ij} is the strain tensor (2nd order), C_{ijkl} is the stiffness tensor (4th order), and S_{ijkl} is the compliance tensor (4th order). Since the properties are not altered by switching $i \leftrightarrow j$ ($\sigma_{ij} = \sigma_{ji}$, $\varepsilon_{ij} = \varepsilon_{ji}$, and $C_{ijkl} = C_{jikl}$) and $i,j \leftrightarrow k,l$ ($C_{ijkl} = C_{klij}$), nine components of stress and strain tensors will reduce to six components and 81 components of the stiffness and compliance tensors reduce to 21 independent variables. The number of independent C_{ijkl} and S_{ijkl} can be reduced by recognizing crystal symmetries. For example, we need only three and five independent components to describe the stiffness and compliance tensors for a cubic and hexagonal crystal system, respectively (see Eq. (2.18)):

$$C_{ij} = \begin{bmatrix} C_{11} & C_{12} & C_{12} & 0 & 0 & 0 \\ C_{12} & C_{11} & C_{12} & 0 & 0 & 0 \\ C_{12} & C_{12} & C_{11} & 0 & 0 & 0 \\ 0 & 0 & 0 & C_{44} & 0 & 0 \\ 0 & 0 & 0 & 0 & C_{44} & 0 \\ 0 & 0 & 0 & 0 & 0 & C_{44} \end{bmatrix} \quad (\text{cubic}) \quad (2.18a)$$

$$C_{ij} = \begin{bmatrix} C_{11} & C_{12} & C_{13} & 0 & 0 & 0 \\ C_{12} & C_{11} & C_{13} & 0 & 0 & 0 \\ C_{13} & C_{13} & C_{33} & 0 & 0 & 0 \\ 0 & 0 & 0 & C_{44} & 0 & 0 \\ 0 & 0 & 0 & 0 & C_{44} & 0 \\ 0 & 0 & 0 & 0 & 0 & \frac{C_{11} - C_{12}}{2} \end{bmatrix} \quad (\text{hexagonal}) \quad (2.18b)$$

In Eq. (2.18), the conventional abbreviated notation for the stiffness tensor was used (see Eq. (2.19)): e.g. $C_{1111}=C_{11}$, $C_{1122}=C_{12}$, ..., $C_{1323}=C_{54}$, ..., etc.

$$\begin{bmatrix} (11) \\ (22) \\ (33) \\ (23) \\ (13) \\ (12) \end{bmatrix} \leftrightarrow \begin{bmatrix} (1) \\ (2) \\ (3) \\ (4) \\ (5) \\ (6) \end{bmatrix} \quad (2.19)$$

ii) Plastic deformation

The plastic deformation behavior of polycrystals is closely related to the slip processes that occur within individual grains of the polycrystalline. It is believed that there are more favorable orientations than others for the dislocation glide, which are usually a crystallographically close packed direction parallel to a closed packed plane. For example, a (0001) slip plane with a slip direction of $\langle 11\bar{2}0 \rangle$ is commonly observed in hexagonal close packed (HCP) materials. However, HCP metals are able to glide on the prismatic and pyramidal planes as well as the close packed basal planes. Because the failure model used in this work is based on elastic fracture (see Chapter 5), the mechanism of the plastic flow and deformation in WC-Co composites will not be described in detail.

2.4.3 Fracture approaches [24-26]

i) Griffith condition

The quantitative relationship between crack size and fracture energy was first investigated by Griffith. The most important point in the Griffith approach is that it does not admit plastic deformation: the only work absorbed in the failure is the elastic energy used to create the fracture surface. Griffith took the stored elastic energy density per unit volume (elastic energy density) to be $\frac{1}{2}\sigma\varepsilon = \frac{\sigma^2}{2E}$, where E is the elastic modulus (Young's modulus) (see Section 2.4.1 ii)). The material volume (per unit thickness) influenced by the crack advance is $2\pi c^2$ (plane stress condition), where $2c$ is the interior crack length. The volume energy released during the crack advance is then $\frac{\pi\sigma^2 c^2}{E}$. On the other hand, the crack surface energy increases by $4c\gamma$, where γ is the surface energy per unit area. Therefore, at the same stress, any cracks above the critical size, c^* , will advance spontaneously. The critical size, c^* , can be determined by the following condition at a given stress:

$$\frac{d}{dc} \left[-\frac{\pi\sigma^2 c^2}{E} + 4c\gamma \right] = 0 \quad (\text{plane stress condition}) \quad (2.20)$$

$$c^* = \frac{2\gamma E}{\pi\sigma^2} \quad (\text{plane stress condition}) \quad (2.21)$$

Inversely, the critical stress, σ^* , at a given crack size can be determined by:

$$\sigma^* = \left(\frac{2\gamma E}{\pi c} \right)^{1/2} \quad (\text{plane stress condition}) \quad (2.22)$$

Here, for a given crack length of c , if the stress is greater than σ^* , then fracture is spontaneous.

ii) Energy release rate and critical intensity factor

The energy release rate approach to fracture includes plastic deformation. The energy release rate, G , is the energy released per unit area of crack advance. In this approach, if G is greater than the critical energy release rate, G_C , then the crack advances spontaneously. In general, G_C is not a material property, but it depends on the geometry (crack size, $2c$) of test specimen and the applied load (P). G_C is usually determined by the following equation:

$$G_C = \frac{P^2}{4t} \frac{dS}{dc} \quad (2.23)$$

where t is the thickness of specimen and S is the compliance.

The stress intensity factor, $K = \sigma\sqrt{\pi c}$, is generally used as a fracture criterion (see Section 2.5.1 ii) for details). Combining Eq. (2.22), the critical stress intensity factor, K_C , is proven to be:

$$K_C(Pa\sqrt{m}) = \sqrt{\frac{G_C E}{(1-\nu^2)}} \quad (\text{plane strain condition}) \quad (2.24a)$$

$$K_C(Pa\sqrt{m}) = \sqrt{G_C E} \quad (\text{plane stress condition}) \quad (2.24b)$$

where ν is the Poisson's ratio. Here, if the stress intensity factor at a given situation is greater than K_C , fracture occurs.

2.5 Microstructure-property relations of WC-Co composites

2.5.1 Mechanical properties [24-26]

i) Hardness

Hardness is a measure of resistance to penetration. Since the carbide phase has a relatively hard and brittle character, and the binder phase is soft and ductile, hardness is primarily accounted for by the carbide phase. In WC-Co composites, therefore, the factor with the most profound influence on apparent hardness is the volume fraction of the carbide phase. The second factor for determining hardness is the particle size of the carbide phase. The schematic relationship between these two microstructural parameters and hardness is shown in Fig. 2.17(a); high hardness is found when the carbide volume fraction is high and the carbide grain size is small. All the WC-Co composite grades are characterized by extremely high hardness values, generally expressed in terms of Vickers (HV) hardness or Rockwell A (HRA) hardness. The Vickers hardness test uses a square-base diamond pyramid as an indenter. This test utilizes the surface area of indentation as a measure of hardness. The unit of Vickers hardness test is $[\text{kg}/\text{mm}^2]$ (the load divided by the surface area of indentation). Instead of the surface area of indentation, the depth of indentation (under a constant load) is used in Rockwell hardness test. Since there are several arbitrary scales for Rockwell hardness depending on the applied load, it is

important to specify which scale is being used. In this thesis, the hardness of WC-Co composites were measured by Vickers hardness tests.

ii) Fracture toughness

Fracture toughness is a measure of the energy required for mechanical failure. Since the ductile binder phase has the ability to absorb energy via plastic deformation, fracture toughness generally exhibits an inverse relation to hardness; low carbide volume fraction and large particle sizes enhance toughness (see Fig. 2.17(b)). The general procedure for measuring fracture toughness involves notching and pre-cracking the specimen, applying a load so that the crack grows, and measurement of the crack advancement. Fracture toughness is not an intrinsic material property. In other words, it depends not only on the materials themselves, but also on the geometry (size) of the material being fractured. For this reason, fracture toughness is usually designated as K_{IC} which is known as the plane strain fracture toughness (or critical stress intensity factor). K_{IC} is independent of the specimen dimensions (size), assuming the test piece is sufficiently large. The plane strain fracture toughness can be estimated through the formula [25]:

$$K_{IC} = \sigma_F \sqrt{\alpha \pi c} \quad (2.25)$$

where σ_F is the stress required to propagate a interior crack of length $2c$, α is a constant dependent on the precise crack shape (close to unity). In Eq. (2.25), the plane fracture toughness (usually called fracture toughness) has the units of $[\text{Pa}\sqrt{\text{m}}]$.

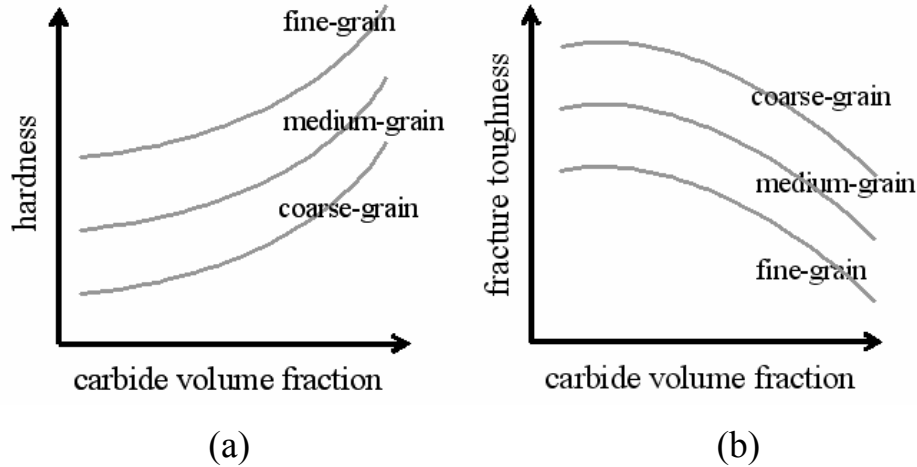


Fig. 2.17 : Schematic plots of the relationship between the mechanical properties and the microstructural parameters. (a) Hardness as a function of the carbide volume fraction and grain size, and (b) fracture toughness as a function of the carbide volume fraction and grain size.

iii) Transverse rupture strength (TRS)

It is customary to perform a tensile test to measure the strength of a material. However, owing to their extreme hardness, WC-Co composites do not respond well to the tensile and/or compression tests. Instead of the tensile test, a transverse rupture strength (TRS) test that bends a specimen until failure is used to measure the fracture strength of WC-Co composites. A typical TRS test for cemented carbides is illustrated in Fig. 2.18. A formula for TRS with a rectangular piece is given by [27]:

$$TRS = \frac{3FL}{2wh^2} \quad (2.26)$$

where, F is the applied force to fracture, L is the distance between two parallel supports, w is the width, and h is the height of test specimen piece (see Fig. 2.18). Because the TRS test estimates the fracture strength of bending, TRS values are expressed in terms of [Pa], the same units as strength and/or stress. Despite the common use of the TRS test for

measuring fracture strength of bending, the relationship between microstructure and TRS is not well-established. Sometimes, TRS said to decrease with carbide volume fraction [28]. It is, however, a matter of controversy. For example, Gurland proposed that a maximum TRS occurs at intermediate binder content [7]. TRS is also influenced by the particle size. Although it is relatively well understood that TRS has the inverse relation to the particle size of carbide, as is the case with hardness, the quantitative relationship is not clear. As mentioned in the introduction chapter (see Section 1.2), the numerical approximation of the TRS (equivalently, fracture strength) in WC-Co composites is one of the primary goals in the current work.

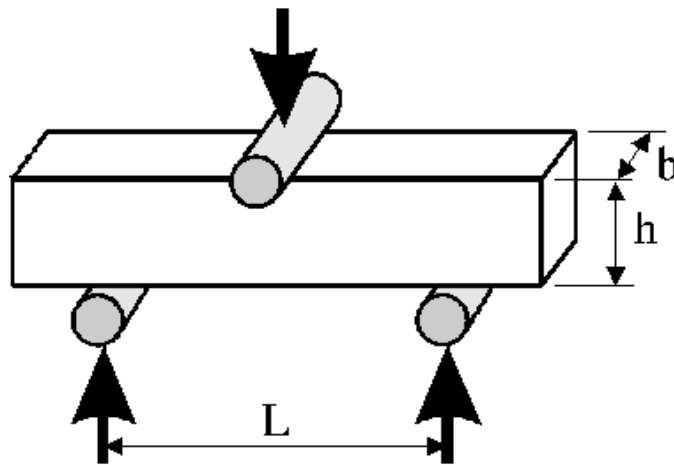


Fig. 2.18 : Schematic illustration of the 3-point transverse rupture strength (TRS) bend test. L is the distance between two parallel supports, b is the with, and h is the height of the test piece.

2.5.2 Past models for microstructure-property relations [29-41]

Since the mechanical properties of WC-Co composites depend on microstructural features, there have been a number of efforts to develop theoretical and empirical models for microstructure-property relationships. Note that in all of these cases, the measured

microstructural parameters were calculated using stereological linear-intercept analysis. Also, they can be considered as ‘semi-empirical’ models, since all of them contain empirical or experimental coefficients based on the measured microstructural factors. In the remainder of this section, some previous models for hardness and fracture toughness are briefly reviewed (The models for strength (or, TRS) of the composites were rarely proposed).

i) Hardness

Most of the past hardness models consist of two parts, a contribution from the carbide phase and a contribution from the binder phase. Attempts were made to relate the hardness of WC-Co composites in terms of the hardness of WC and Co. For the *in-situ* hardness of WC and Co, the empirical relation according to Hall-Petch is frequently used:

$$Hardness = H' + \frac{k}{\sqrt{grain\ size}} \quad (2.27)$$

where H' (hardness of a single crystal) and k (a proportionality factor) are constant.

The most widely accepted hardness model for WC-Co composites is the Lee and Gurland model [29]. The carbide skeleton hypothesis led them to calculate the continuous carbide volume fraction ($f_c C$) and they proposed the following equation with the concept of plastic limit analysis:

$$Hardness (HV) = H_c f_c C + H_b (1 - f_c C) \quad (2.28)$$

$$H_c = 1382 + \frac{23.1}{\sqrt{L^*}}, H_b = 304 + \frac{12.7}{\sqrt{\lambda_1^*}} \quad (\text{kg/mm}^2) \quad (2.29)$$

where H_c and H_b are the *in-situ* hardness of the carbide and binder phase, respectively, f_c is carbide volume fraction, C is contiguity, L^* is stereologically measured linear intercept WC particle size [μm] (Eq. (2.6)), and λ_1^* is stereologically calculated binder mean free path [μm] (Eq. (2.7a)). On right-hand side of Eq. (2.28), the first term describes the effect of WC hardness and second term describes the contribution from Co to the total hardness of composites. Here, the constants in Eq. (2.29) were calculated empirically based on 26 different specimen grades.

Another recent model is the Enqvist et al. model [31]. They rejected the carbide skeleton hypothesis and adopted a model in which hardness decays exponentially with the size of the binder mean free path, λ_2^* . They suggested the following equation that includes only the carbide particle size (L^*) and volume fraction (f_c) parameter, and avoids computing contiguity (C). Note that λ_2^* (which is incorrect) is used, instead of λ_1^* .

$$\text{Hardness (HV)} = (H_c - H_b) e^{-\frac{\lambda_2^*}{k}} + H_b \quad (2.30)$$

$$H_c = 693 + \frac{2680}{\sqrt{2.1 + L^*}}, H_b = 825 \quad (\text{kg/mm}^2) \quad (2.31)$$

where k is the empirically measured hardening range factor (0.35 μm).

ii) Fracture toughness

In most of the previous models, the authors tried to find a proper expression for the strain energy release rate (G). As described before (see Section 2.4.3 ii)), the strain energy release rate (G) can be defined as the rate at which energy is transferred from the

elastic stress field of a crack to the plastic process of crack extension. The critical value of G that makes the crack propagate to fracture, G_{IC} , is the critical strain energy release rate (plane strain condition), and it is linked to the critical stress intensity factor (K_{IC} , plain strain fracture toughness) by the following formula:

$$K_{IC} (Pa\sqrt{m}) = \sqrt{\frac{G_{IC}E}{(1-\nu^2)}} \quad (2.32)$$

where E is Young's modulus, and ν is Poisson's ratio.

Pickens and Gurland [32] suggested that the critical strain energy release rate (G_{IC}) is linearly related to the binder mean free path (λ) and yield strength (σ_y):

$$G_{IC} \cong \alpha\lambda\sigma_y \quad (2.33)$$

where α is the linear coefficient and σ_y is the *in-situ* yield strength. Pickens and Gurland predicted the *in-situ* yield strength based on the Lee and Gurland hardness model [29]. In this model, they also assumed a linear relationship between hardness and yield strength ($H \cong 3\sigma_y$).

Sigl and Fischmeister [37] presented a more elaborate model for the prediction of fracture toughness. They defined four possible crack paths (carbide, binder, carbide/carbide, and binder/carbide), and modeled the strain energy release rates of these four paths.

$$G_{IC} = (r_b A_b + r_{bc} A_{bc}) \bar{\sigma}_f + (A_c + A_{cc}) G_{IC}' \quad (2.34)$$

$$\bar{\sigma}_f = \sigma_y + \frac{\sigma_s - \sigma_y}{2\phi_c + 1} \quad (2.35)$$

where A_b, A_{bc}, A_c, A_{cc} is the area fractions of crack path through the binder (transgranular), binder/carbide interfaces (intergranular), the carbide (transgranular), carbide/carbide interfaces (intergranular), respectively, r_b and r_{bc} are the mean sizes of plastic zone of the binder and binder/carbide interfaces (0.05 μm), respectively, $\bar{\sigma}_f$ is the mean flow stress of binder, σ_s is the saturation stress (12.3 GPa) of binder, σ_y is the yield strength of binder, ϕ_c is the characteristic strain (0.63), and G_{IC}' is the fracture energy of carbide and carbide/carbide boundaries (50 J/m²). Empirical relations were used to calculate the area fractions, A_b, A_{bc}, A_c, A_{cc} [36].

More recently, Ravichandran [40] suggested that the strain energy release rate could be obtained by the sum of the fracture energy of carbide phase ($f_c G_{IC}'$) and fracture resistance of binder phase ($(1 - f_c)\sigma_o \lambda \chi$).

$$G_{IC} = f_c G_{IC}' + (1 - f_c)\sigma_o \lambda \chi \quad (2.36)$$

$$G_{IC}' = \frac{K_c(1 - \nu_c^2)}{E_c} \quad (2.37)$$

$$\chi = \frac{\sigma_{eff}}{\sigma_o} \beta, \quad \frac{\sigma_{eff}}{\sigma_o} = \left[1 + \frac{k}{3} \left(\frac{f_c}{1 - f_c}\right)\right] \quad (2.38)$$

where G_{IC}' is the fracture energy of carbide phase, σ_o is the bulk flow stress of binder (850 MPa), and χ is the rupture parameter of binder, K_c, ν_c, E_c are the fracture toughness, Poisson's ratio, and modulus of carbide, respectively, σ_{eff} is the effective

flow stress of binder, β is the ratio of the critical crack tip to binder thickness (2.0), and k is the maximum shear factor (0.577).

We tested the performances of those previous models using the current specimen grades studied in this thesis. It turned out that the calculated mechanical properties based on the previous models do not match up well with the measured data. This will be presented in Section 3.4.1 and 3.4.2.

2.6 Numerical models for structural analysis

The mechanical response of a material can be modeled by both analytical and numerical methods. Although analytical methods provide closed formed exact solutions, they are limited to specific cases; analytical methods cannot be rigorously applied to complicated microstructures such as those considered in this work. For this reason, since the 1980's, with the increasing capabilities of computers, attempts have been made to predict stress-strain distributions in microstructures using computer-based numerical simulations. Among diverse numerical analysis methods, the finite element method (FEM) is accepted as a powerful tool to approximate the solutions of differential equations governing various physical phenomena. Past attempts to calculate mechanical properties of WC-Co composites using FEM focused only on the prediction of the crack propagation paths using stress-strain analysis within relatively small and localized areas [42, 43].

2.6.1 Finite element methods (FEM) for stress-strain calculations

Like in many other numerical analysis tools, discretizing the domain is the first step in the FEM. The domain is discretized into a finite number of ‘elements’ with polygonal shapes that represent the properties of a corresponding local area. Due to its simplicity, the triangle is the most frequently used element type in two-dimensional finite element analysis. The key to the FEM is utilizing the ‘principle of minimum potential energy’ in these discretized finite elements. The principle of minimum potential energy requires that, when a system reaches an equilibrium state, the first variation of the total potential energy of the system must be zero to minimize the total potential energy. Thus, if we take Π , U^I , and W as the total potential energy, internal potential energy, and work done to the system, respectively, the principle of minimum potential energy can be written in the following way:

$$\Pi = U^I - W \quad (2.39)$$

$$\delta\Pi = \delta U^I - \delta W = 0, \quad \delta U^I = \delta W \quad (2.40)$$

Here, in the stress-strain analysis, the variations of the internal energy and work done to the system are defined as:

$$\delta U^I = \int_{\Omega} \sigma_{ij} (\delta \varepsilon_{ij}) d\Omega \quad (2.41)$$

$$\delta W = \int_{\Omega} b_i (\delta u_i) d\Omega + \int_{\Gamma} s_i (\delta u_i) d\Gamma + \sum_{m=1}^M p_i^m (\delta u_i) \quad (2.42)$$

in which σ_{ij} is the stress tensor, ε_{ij} is the strain tensor, u_i is the displacement, b_i is the body force, s_i is the surface tension, and p_i^m is the mechanical point load at node m . Here,

Ω and Γ represent the respective volume and boundary of the domain, and M denotes the total number of nodes. The preceding equation (Eq. (2.42)) is applicable only to the system under mechanical loads. For a system under thermal loads, the work variation term (Eq. (2.42)) should be modified. From Eq. (2.41) and Eq. (2.42), the principle of minimum potential energy reduces to:

$$\int_{\Omega} \sigma_{ij} (\delta \varepsilon_{ij}) d\Omega = \int_{\Omega} b_i (\delta u_i) d\Omega + \int_{\Gamma} s_i (\delta u_i) d\Gamma + \sum_{m=1}^M p_i^m (\delta u_i) \quad (2.43)$$

In Eq.2.43, the only unknown variable is the displacement (u_i), because the elastic relations of strain-displacement and stress-strain are well-established:

$$\varepsilon_{ij} = L_{ijk} u_k \quad (2.44)$$

$$\sigma_{ij} = C_{ijkl} \varepsilon_{kl} \quad (2.45)$$

where L_{ijk} is the linear differential operator tensor, and C_{ijkl} is the stiffness tensor. Since Eq. (2.43) is analytically unsolvable in a complex structure, a basis function (shape function) is introduced in order to numerically resolve the problem. Employing a basis function also allows us to calculate the displacements at all points inside an element in terms of nodal values (displacements of nodes). A general finite element formulation for the definition of a basis function is expressed by:

$$u_i \approx \hat{u}_i = \sum_{m=1}^M N^m u_i^m \quad (2.46)$$

where N^m is the basis function at node m and u_i^m is the displacement vector whose components are the approximations of the displacements at node m . The basis function

(N^m) varies linearly from 1 at node m to 0 at the remaining nodes. Then, the strains and stresses at any point follow as:

$$\varepsilon_{ij} = L_{ijk} u_k = L_{ijk} \sum_{m=1}^M N^m u_k^m = \sum_{m=1}^M B_{ijk}^m u_i^m, \text{ where } B_{ijk}^m = L_{ijk} N^m \quad (2.47)$$

$$\sigma_{ij} = C_{ijkl} \varepsilon_{kl} = C_{ijkl} \sum_{m=1}^M B_{klm}^m u_m^m \quad (2.48)$$

Substituting Eq. (2.46)~(2.48) into the minimum potential energy equation (Eq. (2.43)), the equation becomes (in a matrix form):

$$\sum_{m=1}^M \left[\int_{\Omega} (\mathbf{B})^T \mathbf{C} \mathbf{B} d\Omega \right] \mathbf{u} = \int_{\Omega} \mathbf{N} \mathbf{b} d\Omega + \int_{\Gamma} \mathbf{N} \mathbf{s} d\Gamma + \sum_{m=1}^M \mathbf{N} \mathbf{p} \quad (2.49)$$

This equation set can be expressed in terms of the standard algebraic equation system:

$$\mathbf{K} \boldsymbol{\phi} = \mathbf{f} \quad (2.50)$$

where

$$\mathbf{K} = \sum_{m=1}^M \left[\int_{\Omega} (\mathbf{B})^T \mathbf{C} \mathbf{B} d\Omega \right], \boldsymbol{\phi} = \mathbf{u}, \mathbf{f} = \int_{\Omega} \mathbf{N} \mathbf{b} d\Omega + \int_{\Gamma} \mathbf{N} \mathbf{s} d\Gamma + \sum_{m=1}^M \mathbf{N} \mathbf{p} \quad (2.51)$$

\mathbf{K} is called the global matrix (or, stiffness matrix) which can be obtained by summing the contributions from the individual element matrices whose components are defined by:

$$\mathbf{K}_e^{lm} = \int_{\Omega_e} (\mathbf{B}_e^l)^T \mathbf{C} \mathbf{B}_e^m d\Omega \quad (2.52)$$

Likewise, \mathbf{f} (which is called the load vector) can be decomposed into a set of element load vectors:

$$\mathbf{f}_e^l = \int_{\Omega^e} \mathbf{N}^l \mathbf{b} d\Omega + \int_{\Gamma^e} \mathbf{N}^l s d\Gamma + \mathbf{N}^l \mathbf{p} \quad (2.53)$$

From Eq. (2.49) and Eq. (2.50), the solutions of the displacements of individual nodes are approximated, and also elastic stress-strain distributions can be calculated by strain-displacement and stress-strain relations (Eq. (2.44) and (2.45)). The detailed descriptions for the residual stress-strain calculations using FEM can be found elsewhere [44-47].

2.6.2 Previous analyses for the prediction of crack paths in WC-Co composites using FEM

In most of the cases, the prediction of crack paths in WC-Co composites has been a main issue in the past attempts for stress-strain field analysis using FEM. Fischmeister et al. [42] calculated the distribution of plastic strains and measured the size of plastic zones in the binder phase. They found that the plastic zone size is smaller than the size of the binder mean free path and that it depends on the shape of the binder regions, which is in agreement with experimental observations. In the initial setting for the FEM calculations, intergranular cracks were assumed to have already formed in the carbide phase. In other words, only the stress-strain states in the binder phase are analyzed in their model.

Spiegler and Fischmeister [43] used a FEM analysis to decide whether cracks propagate along the binder/carbide interface (intergranular) or through the binder phases

(transgranular). They explained that the crack path is determined by the angle at which the crack enters the binder region. It was found that the critical transition angle from transgranular to intergranular fracture is 25° . Both of the preceding analyses were based on the average properties of individual phases (Young's modulus: E_{WC} , E_{Co} , $E_{Composites}$ = 714, 211, 595 GPa, and Poisson's ratio: ν_{WC} , ν_{Co} , $\nu_{Composites}$ = 0.19, 0.31, 0.22, respectively). Another shortcoming of the prior studies is that the calculated regions are limited to localized areas (small area simulations), including less than 20 carbide grains.

2.6.3 Object-oriented finite element (OOF) model

Recently, a comprehensive package for mechanical property calculations has been developed, and continues to be improved by NIST (National Institute of Standards and Technology, Gaithersburg, MD) [47]. The name of this code, object-oriented finite element (OOF) analysis, derives from the object-oriented programming language in which it is encoded (in this case, C++).

Based on the FEM, OOF is designed to approximate solutions in stress-strain states of complex microstructures (including a large number of grains) under mechanical and/or thermal loads. Its ability to model a large number of grains is the primary merit of the OOF code. The stress-strain fields of complicated microstructures having more than several hundred grains can be calculated. It is an obvious advantage over the past analysis models in which the calculations are confined to small, localized areas. Another advantage of the OOF package is that the specific materials properties (crystallographic orientations, stiffness, thermal expansion coefficients, and surface energies of fracture surfaces) of individual crystals are easily incorporated. In other words, the anisotropic

characteristics of each material can be accounted for in the calculation of the internal stress and strain. In the previous FEM models of WC-Co composites, these crystallographic anisotropies have not been properly modeled [40, 41]. For example, the bulk Young's modulus and Poisson's ratio were used instead of the stiffness (C_{11} , C_{33} , C_{44} , C_{12} , and C_{13}) of each phase. OOF also provides a way to simulate crack propagation. It assumes an element cracks when the supplied stored energy is greater than the surface energy the element. It is closely associated with 'brittle fracture', or 'Griffith-like fracture' (see section 2.4.3 i)). This brittle fracture criterion can be written as:

$$2\gamma\Delta L \leq \frac{1}{2}\sigma_{ij}\varepsilon_{ij}A \quad (2.54)$$

where γ is the surface energy of the cracked interface, ΔL is the edge length, A is the area, σ_{ij} is the stress, and ε_{ij} is the strain of a element, respectively. A typical procedure for OOF simulation is as follows:

- 1) Start with a micrograph. The micrograph could be a virtual image from a computer simulation, or an experimental map from certain microscopes. Any digitalized microstructure can be used as input for OOF simulations.
- 2) Select features in the image and assign materials properties. In the OOF code, individual crystals are usually differentiated by color contrast differences. In each distinct crystal, corresponding materials properties are then applied (e.g. orientations, elastic constants, thermal expansion coefficients, and surface energies).

- 3) Perform a virtual experiment with relevant boundary conditions. The simulation is able to be carried out under mechanical loads (tensile or compression) and/or thermal loads (quenching or annealing).
- 4) Calculate and visualize the internal stress and strain. Using a finite element algorithm, the solutions of stress-strain states are approximated. In the OOF package, these solutions can be visualized in terms of various stress, strain, or stored energy distributions such as σ_{xx} , σ_{yy} , σ_{zz} , σ_{xy} , σ_{yz} , σ_{zx} , stress invariant 1 (σ^I , $\sigma^I = \sigma_{xx} + \sigma_{yy} + \sigma_{zz}$), ϵ_{xx} , ϵ_{yy} , ϵ_{zz} , ϵ_{xy} , ϵ_{yz} , ϵ_{zx} , strain invariant 1 (ϵ^I , $\epsilon^I = \epsilon_{xx} + \epsilon_{yy} + \epsilon_{zz}$), or elastic energy density.
- 5) Compute the macroscopic mechanical properties. From the calculation of internal stress and strain, the effective mechanical properties (macroscopic modulus, average stress, average strain, etc.) can be estimated.

There are some reports on mechanical property calculations using the OOF code described in this section. Vedula et al. calculated the stresses and elastic energy densities in polycrystalline alumina. They also compared the stress distributions in orientation textured and non-textured samples and verified that the textured microstructure exhibits a low distribution of stress and stored energy [48]. In this document, this texture effect on the strength of WC-Co composites will be presented in Chapter 5 (see Section 5.3.5). Chawla et al. used the OOF package for the calculations of Young's moduli and thermal expansion coefficients of SiC-Al and WC-Co (double carbide) composites [49]. The authors demonstrated that the calculations are consistent with the experimental results. In this literature [49], the detailed description of OOF code was also presented.

2.7 Summary

In the preceding sections in this chapter, background theories and models which are relevant to the thesis have been reviewed. Previously, the WC habits in the WC/Co interface and the skeletons of WC/WC grain boundaries have been measured in a qualitative way. All of the measurements of microstructural features were accomplished by the linear-intercept method. The mechanical properties (especially for the hardness and fracture toughness) of the composites were modeled as a function of the carbide volume fraction (f_c) and the particle size (average carbide size and mean binder free path). In the following chapters, we will describe in detail about experimental and analytical methods for the microstructural characterization from direct measurements, interface character distributions using a stereological method, and fracture strength calculations based on finite element simulations.

2.8 References

- [1] P.W. Tasker, “The Stability of Ionic Crystal Surfaces”, *J. Phys. C*, **12**, 4977 (1979)
- [2] A.D. Krawitz, D.G. Reichel, and R. Hitterman, “Thermal Expansion of Tungsten Carbide at Low Temperature”, *J. Am. Ceram. Soc.*, **72**, No.3, 515 (1989)
- [3] R.R. Reeber and K. Wang, “Thermophysical Properties of a-Tungsten Carbide”, *J. Am. Ceram. Soc.*, **82**, No. 1, 129 (1999)
- [4] H.E. Exner, “Physical and Chemical Nature of Cemented Carbides”, *Int. Metal. Rev.*, No. 4, 149 (1979)

- [5] L. Ramqvist, "Wetting of Metallic Carbides by Liquid Copper, Nickel, Cobalt and Iron", *Int. J. Powder Metall.*, **1**, No. 4, 2 (1965)
- [6] D.N. French, "The Microstructure and Microproperties of WC-Co Alloys", *Int. J. Powder Metall.*, **5**, No. 3, 47 (1969)
- [7] J. Gurland, "New Scientific Approaches to Development of Tool Materials", *Int. Mater. Rev.*, **33**, No. 3, 151 (1988)
- [8] A.V. Shatov, S.A. Firstov, and I.V. Shatova, "The Shape of WC Crystals in Cemented Carbides", *Mater. Sci. Eng. A*, **242**, 7 (1998)
- [9] H.-R. Lee, D.-J. Kim, N.-M. Hwang, and D.-Y. Kim, "Role of Vanadium Carbide Additive during Sintering of WC-Co: Mechanism of Grain Growth Inhibition", *J. Am. Ceram. Soc.*, **86**, No. 1, 152 (2003)
- [10] S. Kim, S.-H. Han, J.-K. Park, and H.-E. Kim, "Variation of WC Grain Shape with Carbon Content in the WC-Co Alloys during Liquid-phase Sintering", *Scripta Mater.*, **48**, 635 (2003)
- [11] V. Randle and L. Engler, Introduction to Texture Analysis, 1st ed., Taylor & Francis Ltd, 2002
- [12] A. Heinz and P. Neumann, "Representation of Orientation and Disorientation Data for Cubic, Hexagonal, Tetragonal, and Orthorhombic Crystals", *Acta Crystal.*, **A44**, 326 (1988)
- [13] A. Morawiec and D.P. Field, "Rodrigues Parameterization for Orientation and Misorientation Distributions", *Phil.Mag.A*, **73**, No.4, 1113 (1996)
- [14] G.S. Rohrer, Structure and Bonding in Crystalline Materials, 1st ed., Cambridge University Press, Inc., 2001

- [15] S. Bartolucci and H.H. Schlosin, “Plastic Deformation Preceding Fracture in Tungsten Carbide-Cobalt Alloys”, *Acta Metall. Mater.*, **14**, No. 3, 337 (1966)
- [16] J. Gurland and J.T. Norton, “Role of the Binder Phase in the Cemented Carbide-Cobalt Alloys”, *Trans. Metall. Soc. AIME*, **194**, 1051 (1952)
- [17] A. Henjered, M. Hellsing, H.-O. Andren, and H. Norden, “Quantitative Microanalysis of Carbide/carbide Interfaces in WC-Co-base Cemented Carbides”, *Mater. Sci. Technol.*, **2**, 847 (1986)
- [18] S. Hagege, G. Nouet, and P. Delavignette, “Grain Boundary Analysis in TEM (IV)”, *Phys. Stat. Sol. A*, **61**, 97 (1980)
- [19] R. Deshmukh and J. Gurland, “Orientation of Contiguous Tungsten carbide Crystals in Sintered WC-Co as Determined from Slip Line Traces”, *Metallography*, **15**, 383 (1982)
- [20] B. Roebuck and E.A. Almond, “Deformation and Fracture Processes and the Physical Metallurgy of WC-Co Hardmetals”, *Int. Mater. Rev.*, **33**, No. 2, 90 (1988)
- [21] E. Underwood, Quantitative Stereology, Addison-Wesley, Inc., New York, 1970
- [22] J. Gurland, “An Estimate of Contact and Contiguity of Dispersions in Opaque Samples”, *Trans. Metall. Soc. AIME*, **236**, 642 (1966)
- [23] R.M. German, “The Contiguity of Liquid Phase Sintered Microstructures”, *Metall. Trans. A*, **16A**, 1247 (1985)
- [24] G.E. Dieter, Mechanical Metallurgy, McGraw-Hill, Inc., 1988
- [25] T.H. Courtney, Mechanical Behavior of Materials, 2nd ed., McGraw-Hill, Inc., 2000
- [26] R.E. Reed-Hill and R.A. Abbaschian, Physical Metallurgy Principles, 3rd ed., PWS Publishing Co., 1994
- [27] Work Instructions for TRS test, Kennametal, Inc., 1998

- [28] G. Schneider, Jr., Principles of Tungsten Carbide Engineering, 2nd ed., Society of Carbide and Tool Engineers, 1989
- [29] H.C. Lee and J. Gurland, “Hardness and Deformation of Cemented Tungsten Carbide”, *Mater. Sci. Eng.*, **33**, 125 (1978)
- [30] M.T. Laugier, “A Microstructural Model for Hardness in WC-Co Composites”, *Acta Metall.*, **33**, No. 11, 2093 (1985)
- [31] H. Engqvist, S. Jacobson, and N. Axen, “A Model for Hardness of Cemented Carbides”, *Wear*, **252**, 384 (2002)
- [32] J.R. Pickens and J. Gurland, “The Fracture Toughness of WC-Co Alloys Measured on Single-edge Notched Beam Specimens Pre-cracked by Electron Discharge Machining”, *Mater. Sci. Eng.*, **33**, 135 (1978)
- [33] M. Nakamura and J. Gurland, “The Fracture Toughness of WC-Co Two-Phase Alloys – A Preliminary Model”, *Metall. Trans. A*, **11A**, 141 (1980)
- [34] V.D. Krstic and M. Komac, “Toughening in WC-Co Composites”, *Philos. Mag. A*, **51**, No. 2, 1985 (1985)
- [35] D.K. Shetty, I.G. Wright, P.N. Mincer, and A.H. Clauer, “Indentation Fracture of WC-Co Cermets”, *J. Mater. Sci.*, **20**, 1873 (1985)
- [36] L.S. Sigl and H.E. Exner, “Experimental Study of Mechanics of Fracture in WC-Co Alloys”, *Metall. Trans. A*, **18A**, 1299 (1987)
- [37] L.S. Sigl and H.F. Fischmeister, “On the Fracture Toughness of Cemented Carbides”, *Acta Metall.*, **36**, No. 4, 887 (1988)
- [38] D. Han and J.J. Mecholsky, “Fracture Analysis of Cobalt-bonded Tungsten Carbide Composites”, *J. Mater. Sci.*, **25**, 4949 (1990)

- [39] D.B. Marshall, W.L. Morris, B.N. Cox, and M.S. Dadkhah, “Toughening Mechanisms in Cemented Carbides”, *J. Am. Ceram. Soc.*, **73**, No. 10, 2938 (1990)
- [40] K.S. Ravichandran, “Fracture Toughness of Two Phase WC-Co Cermets”, *Acta Metall. Mater.*, **42**, No. 1, 143 (1994)
- [41] J.M. Densley and J.P. Hirth, “Fracture Toughness of a Nanoscale WC-Co Tool Steel”, *Scripta Mater.*, **38**, No. 2, 239 (1998)
- [42] H.F. Fischmeister, S. Schmauder and L.S. Sigl, “Finite Element Modeling of Crack Propagation in WC-Co hard Metals”, *Mater. Sci. and Eng. A*, **105/106**, 305 (1988)
- [43] R. Spiegler and H.F. Fischmeister, “Prediction of crack paths in WC-Co alloys”, *Acta Metall. Mater.*, **40**, No. 7, 1653 (1992)
- [44] O.C. Zienkiewicz and K. Morgan, Finite Elements and Approximation, John Wiley & Sons, Inc., 1983
- [45] J.N. Reddy, An Introduction to the Finite Element Method, 2nd ed., McGraw-Hill, Inc., 1993
- [46] E.B. Becker, G.F. Carey, and J.T. Oden, Finite Elements – An Introduction : Volume 1, Prentice-Hall, Inc., New Jersey, 1981
- [47] W.C. Carter, S.A. Langer and E.R. Fuller Jr., The OOF Manual (version 1.0.8.6), National Institute of Standards and Technology (NIST), (2001); also available online at <http://www.ctcms.nist.gov/oof>
- [48] V.R. Vedula, S.J. Glass, D.M. Saylor, G.S. Rohrer, W.C. Carter, S.A. Langer, E.R. Fuller, “Residual-stress Predictions in Polycrystalline Alumina”, *J. Am. Ceram. Soc.*, **84**, No. 12, 2947 (2001)

[49] N. Chawla, B.V. Patel, M. Koopman, K.K. Chawla, R. Saha, B.R. Patterson, E.R. Fuller, and S.A. Langer, “Microstructure-based Simulation of Thermomechanical Behavior of Composite Materials by Object-oriented Finite Element Analysis”, *Mater. Character.*, **49**, 395 (2003)

Chapter 3

Microstructural Characterization

This chapter describes the methods used to characterize the microstructures of WC-Co composites and presents the results of the analysis. Atomic force microscopy (AFM) and orientation imaging microscopy (OIM) have been used to extract the binder/carbide and carbide/carbide interface positions in WC-Co composites with carbide volume fractions from 0.7 to 0.9 and mean carbide grain diameters from one to seven microns. In this work, we measure the microstructural features using direct measurements of two-dimensional features rather than the conventional linear-intercept method. We will start this chapter with descriptions of the sample preparation method and direct measurement technique used throughout this thesis. After presenting the quantitative results, the relationship between microstructures and properties will be discussed.

3.1 Samples

Nine specimen grades are used for this thesis (samples were prepared at Kennametal Inc., Latrobe, PA, USA). The first eight, labeled *A-H*, contain no intentional alloying additions (straight grades). The last straight specimen grade (grade *H*) is known as a non-angular grade which, in contrast to the grades *A* through *G*, is comprised of carbide grains with less polygonal shapes. The ninth sample, specimen grade *I*, is an alloyed grade that contains Ta, Ti, and Nb at concentrations of 4.7, 2.1, and 0.5 weight

percent (w/o), respectively. This sample is also referred to as a plate-like grade and it contains carbides that are elongated in directions perpendicular to the [0001] axis. Throughout this thesis, the same notation for the nine specimen grades (*A~I*) will be used. The phase fractions for each specimen grade are listed in Table 3.1. These commercially produced samples were consolidated via liquid phase sintering for approximately 45 min. at temperatures in the range of 1400 °C to 1600 °C. Materials with the highest binder fractions were sintered at the lower end of this temperature range and those with the least binder were sintered at the higher temperature. Images from these samples using atomic force microscopy (AFM) are shown in Fig. 3.1 (same scale).

Grade	Carbide fraction (weight)	Carbide fraction (volume)
<i>A</i>	0.940	0.8992
<i>B</i>	0.940	0.8992
<i>C</i>	0.900	0.8367
<i>D</i>	0.900	0.8367
<i>E</i>	0.800	0.6949
<i>F</i>	0.905	0.8443
<i>G</i>	0.920	0.8675
<i>H</i>	0.930	0.8832
<i>I</i>	0.929	0.8815

Table 3.1 : Carbide volume fractions for each specimen grade.

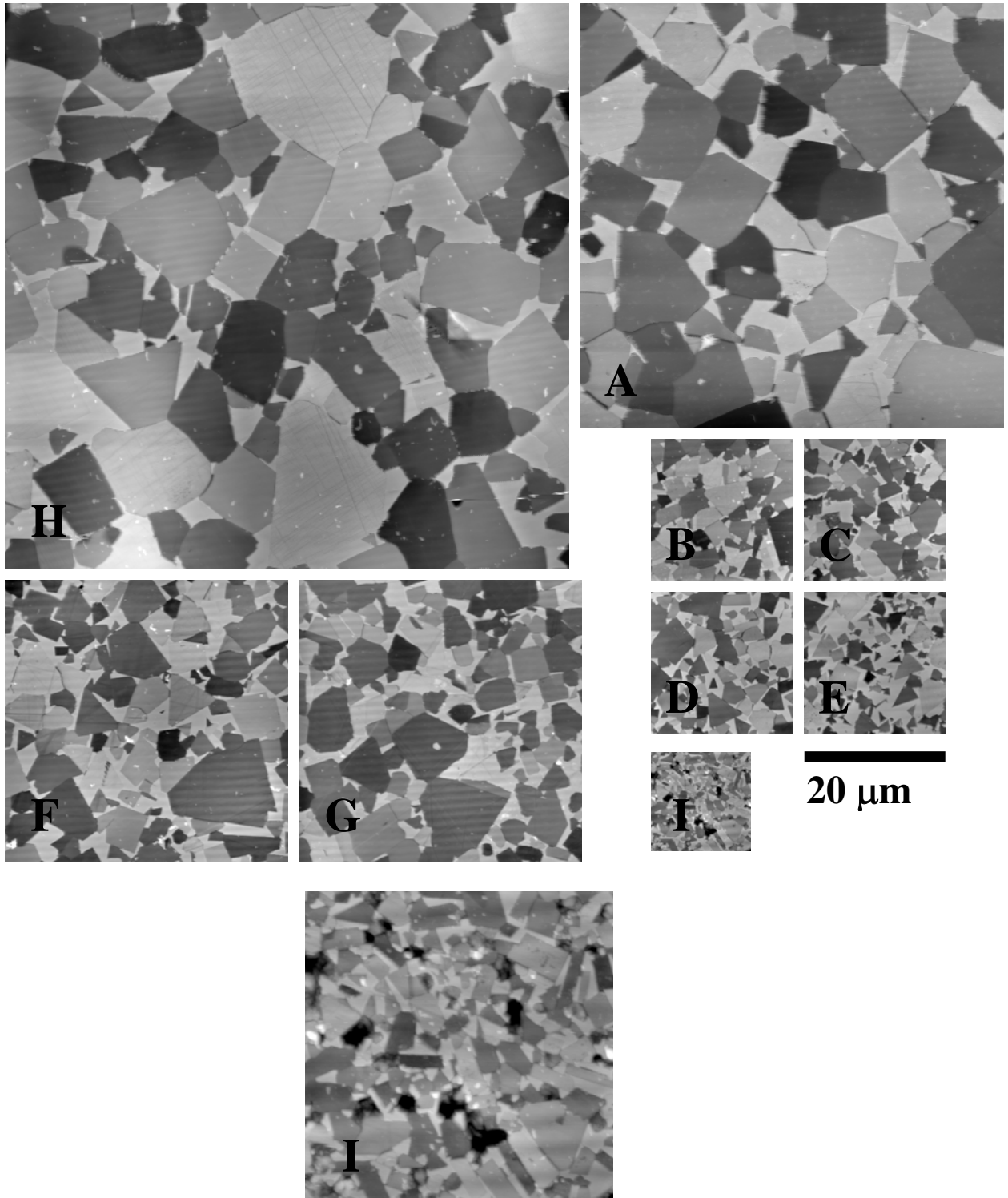


Fig. 3.1 : Images of nine specimen grades (A~I) from atomic force microscopy (AFM). For comparison, same scale is used for upper nine grades. In the bottom, AFM image (different scale, $14 \times 14 \mu\text{m}^2$) of grade I (plate-like grade) is re-shown for a clear visualization.

After polishing using a diamond abrasive, the samples were etched in Murakami's reagent (10 g potassium ferricyanide+10 g sodium hydroxide+100 ml distilled water) for 1 min. The reagent preferentially attacks the carbide phase with different rates and produces topographic differences at the binder/carbide interfaces and the carbide/carbide boundaries that lead to sharp contrast in atomic force microscopy (AFM) images (see Fig. 3.1 and 3.2). Here, dark contrast corresponds to the topologically lower surface (the binder phase before the etch and the carbide phase after the etch), and white contrast represents the relatively higher surfaces (the carbide phase before the etch and the binder phase after the etch).

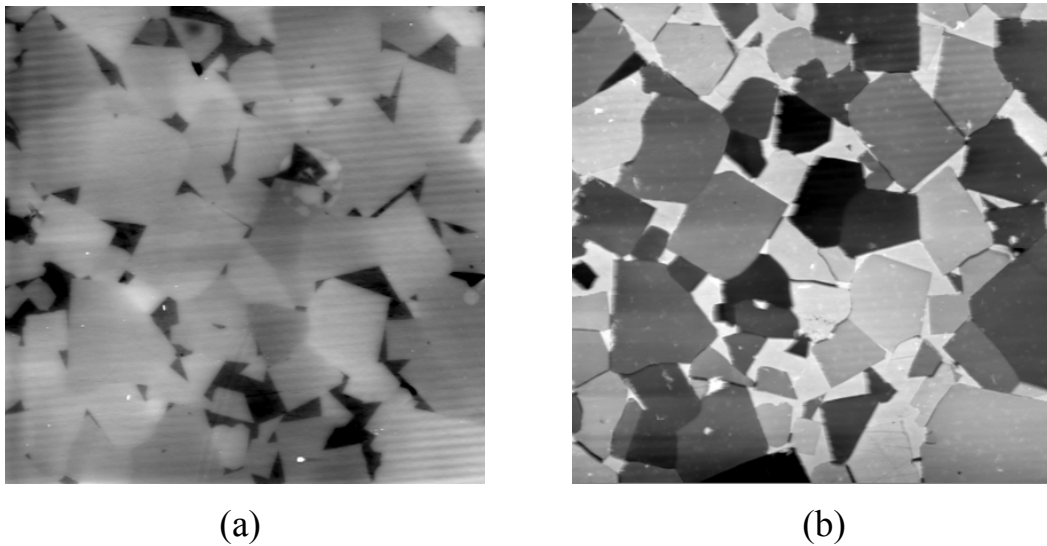


Fig. 3.2 : Advantage of etching in Murakami's reagent (from grade A, $60 \times 60 \mu\text{m}^2$). Same sections are shown. (a) Before etching, and (b) after etching in Murakami's reagent for 1 min. White contrast corresponds to the topologically higher region and dark contrast corresponds to lower region.

3.2 Microstructure and property characterization methods

3.2.1 Atomic force microscopy (AFM)

A Park Scientific Instruments Cp or a Thermomicroscopes M5 was used for all AFM imaging. Gold-coated, sharpened pyramidal Si_3N_4 probes (Thermomicroscopes ML06A-F) were used to obtain contact images. The field of view for each AFM image was selected based on a rough estimate of WC grain size ($80 \times 80 \mu\text{m}^2$ for *H*, $60 \times 60 \mu\text{m}^2$ for *A*, $40 \times 40 \mu\text{m}^2$ for *F* and *G*, $20 \times 20 \mu\text{m}^2$ for *B*, *C*, *D*, and *E*, and $14 \times 14 \mu\text{m}^2$ for *I*) such that each AFM section contains 100~180 carbide grains. The microscope was programmed to automatically record 100 images in a 10 by 10 array such that there was approximately a 10 % overlap with adjacent images in the array. Thus, the total scanned areas ranged from $710 \times 710 \mu\text{m}^2$ for sample *H* to $122 \times 122 \mu\text{m}^2$ for sample *I*. This imaging procedure allows the shape of many grains to be determined with high resolution. Since there are 512×512 pixels in each of the AFM images, the pixel spacing is $0.16 \mu\text{m}$ (*H*), $0.12 \mu\text{m}$ (*A*), $0.08 \mu\text{m}$ (*F* and *G*), $0.04 \mu\text{m}$ (*B*, *C*, *D*, and *E*) and $0.03 \mu\text{m}$ (*I*). Typical AFM digital images (after etching in Murakami's reagent) of WC-Co composites are illustrated in Fig. 3.3(a) (from grade *A*). The Individual WC grains are dissolved at different rates by the etching solution and, therefore, have various shades of darker contrast. The differential etching allows both WC/Co and WC/WC boundaries to be easily identified. In our experience, the vertical sensitivity of the AFM allows the phase boundaries in WC-Co composites to be resolved more clearly than optical microscopy (OM) or scanning electron microscopy (SEM). This is particularly important for

measuring the shapes of the crystals with sub-micron diameters that are found in these materials.

3.2.2 Orientation imaging microscopy (OIM)

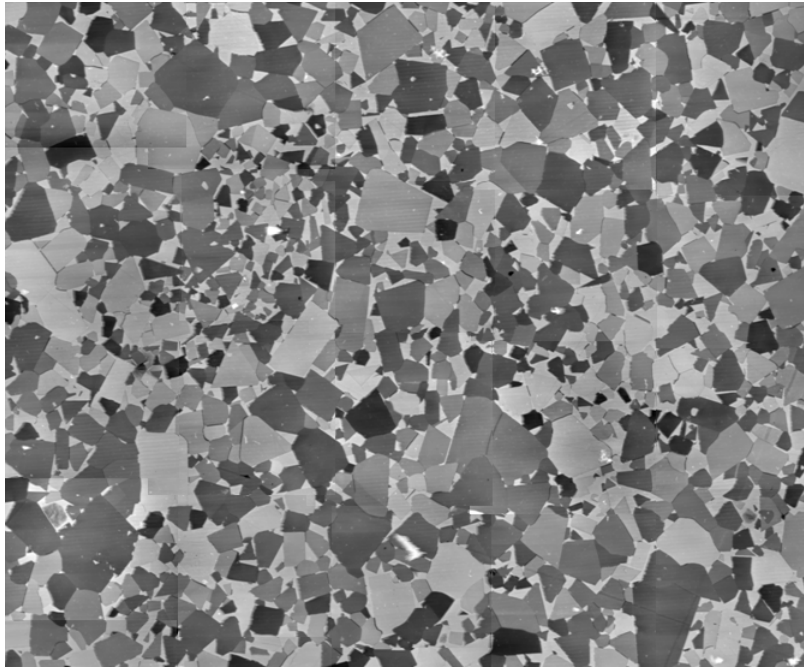
In this work, carbide grain orientations were determined using an OIM system (TexSEM Laboratories, Inc.) incorporated in a Phillips XL40 FEG scanning electron microscope (SEM). These measurements also made it possible to distinguish ambiguous carbide/carbide and cobalt/carbide phase boundaries. For each sample, carbide orientations were mapped in the same regions imaged by AFM. Orientation measurements were made at intervals of 1.2 μm (*H*), 1.0 μm (*A*), 0.4 μm (*F* and *G*), 0.2 μm (*B*, *C*, *D*, and *E*) and 0.15 μm (*I*) over total areas of 800×800 μm^2 , 600×600 μm^2 , 360×360 μm^2 , 180×180 μm^2 and 150×150 μm^2 , respectively. All OIM images were recorded at a specimen tilt of 70°, an accelerating voltage of 20 kV, and a spot size of 5. A typical OIM inverse pole figure (IPF) map is shown in Fig. 3.3(b) (from grade A, same section as Fig. 3.3 (a)). Here, the color contrast stands for the normal direction of the surface plane in each WC crystal.

During these studies, the orientations of Co grains were not recorded. Several factors make it difficult to collect reliable electron backscattered patterns (EBSPs) from the Co phase. First, because of the small size of the binder pools and the topographic differences between carbide and binder phases, the patterns can be affected by superposition and shadowing. Second, because of the different mechanical properties of the two phases, the conditions required for polishing the composites to yield good EBSPs from the carbide grains created so much plastic damage in the binder that diffraction from

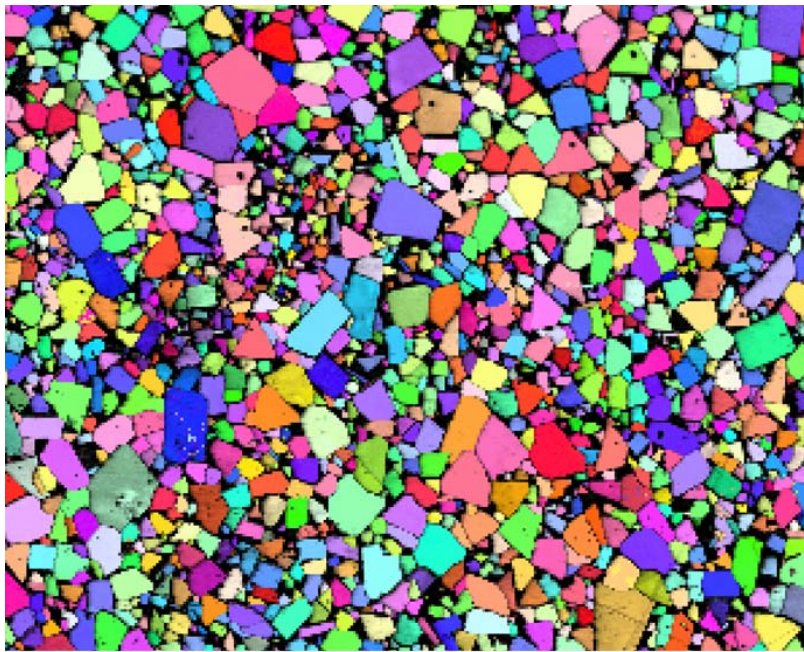
the Co was not observed. Polishing procedures that produced acceptable surfaces of pure Co samples were not aggressive enough to polish the carbide phase. The only way we found to prepare samples so that EBSPs could be simultaneously recorded from the carbide and the binder was to first polish the samples to prepare the carbide phase, and then anneal the sample at 800 °C (in a reducing environment) to heal some of the plastic damage in the binder phase. It was then possible to record EBSPs from the largest binder pools. Limited studies of the sample with the highest volume fraction of Co indicated that neighboring pools of Co had the same orientation and that the Co grain size was larger than the carbide grain size.

3.2.3 Microstructure analysis

The positions of binder/carbide interfaces and carbide/carbide boundaries in AFM images are digitized using a program that automatically records the vector components of binder/carbide (l_{bc}) and carbide/carbide (l_{cc}) line segments when the user traces them with a computer mouse. Hence, polygonal closed contours of WC particles consisting of binder/carbide and carbide/carbide line segments joined at N vertices can be constructed. For each of the nine specimen grades, the boundaries in 20 AFM images were skeletonized so that for each grade, the geometric results are based on measurements of approximately 2500 carbide grains. An example of a skeletonized map is shown in Fig. 3.4. The grain area (A) of carbide is then computed as the total number of pixels within a closed polygon, multiplied by the area per pixel. Grain diameters (d) are computed by assuming that the grain area is circular ($d=2(A/\pi)^{1/2}$). The contiguity of carbide phase (C) is computed according to the following expression:



(a)



70.00 μm = 70 steps IQ 33.38...94.22, IPF [001]

(b)

Fig. 3.3 : Typical images of AFM and OIM in the same area (from grade A). (a) 5×4 array of AFM images, (b) OIM inverse pole figure (IPF) map (Co phase is not indexed).

$$C = \frac{2 \sum_i l_{cc}^i}{\sum_{i,j} (2l_{cc}^i + l_{bc}^j)} \quad (3.1)$$

By tracing the carbide grains and assigning the line segments as binder/carbide or carbide/carbide interfaces, the number of vertices (N), the grain area (A), the grain diameter (d), and the contiguity (C) are determined by direct observation. For comparison, however, we also examined quantities determined from linear-intercept lengths and quantities computed using stereological equations based on the frequency of linear-intercepts. We use all 512 lines in each of the 20 skeletonized AFM image as test lines, so that approximately 2 (x- and y-direction) $\times 10^4$ test lines are used for each specimen grade. From these test lines, we determined the mean carbide intercept length, L , and the mean binder intercept length, λ , and the average number of intercepts per unit length of test line with carbide/carbide boundaries (N_{cc}) and binder/carbide interfaces (N_{bc}). The stereologically determined carbide grain size, L^* , is:

$$L^* = \frac{2f_c}{2N_{cc} + N_{bc}} \quad (3.2)$$

where f_c is the volume fraction of the carbide phase. The stereologically derived contiguity (C^*) is:

$$C^* = \frac{2N_{cc}}{2N_{cc} + N_{bc}} \quad (3.3)$$

In previous work, there are two different expressions by which the stereologically determined binder mean free path (λ^*) is computed:

$$\lambda_1^* = L^* \frac{(1-f_c)}{f_c(1-C)} \quad (3.4a)$$

$$\lambda_2^* = L^* \frac{(1-f_c)}{f_c} \quad (3.4b)$$

where λ_1^* was used in references [1-3] and λ_2^* was used in references [4, 5]. We shall see that λ_1^* turns out to be the correct expression for WC-Co composites.

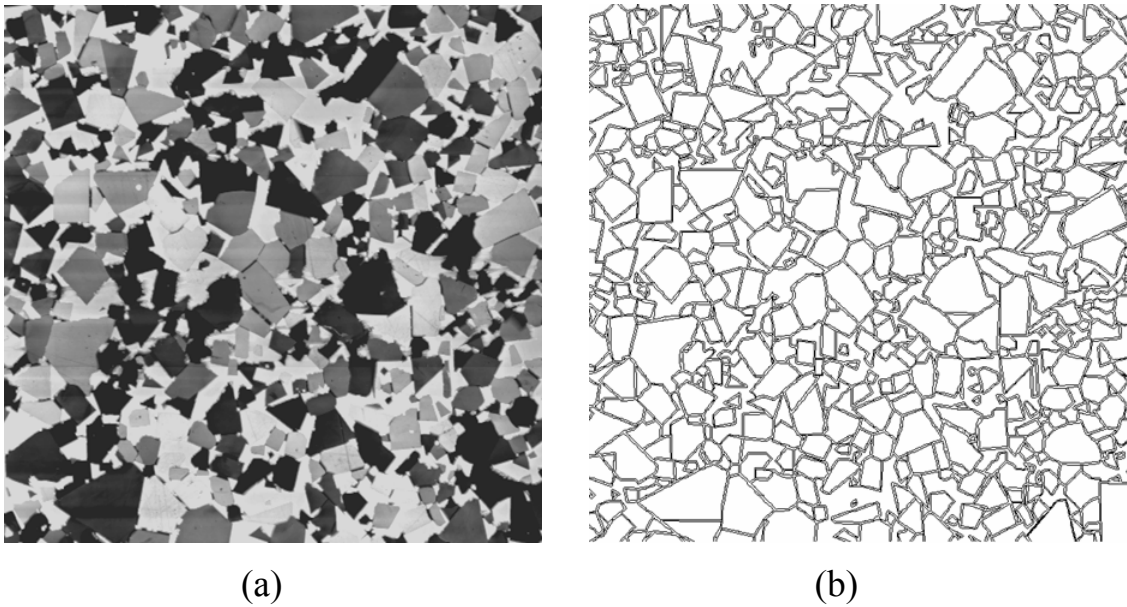


Fig. 3.4 : Example of direct measurements (from grade *D*, $40 \times 40 \mu\text{m}^2$). (a) Original AFM image, (b) skeletonized map.

3.2.4 Measurements of mechanical properties

All of the measured mechanical properties are summarized in Table 3.2. These measurements were all conducted by collaborators at Kennametal Incorporated (Latrobe, PA, USA). The values in parentheses are the standard deviations in each grade.

Grade	Hardness [HV]	Toughness [MPa]	TRS [GPa]
<i>A</i>	1070.8 (9.7)	17.9 (0.29)	1.94 (0.05)
<i>B</i>	1343.8 (6.0)	12.7 (0.37)	3.29 (0.13)
<i>C</i>	1160.6 (3.1)	13.8 (0.34)	2.84
<i>D</i>	1173.6 (6.0)	14.6 (0.32)	-
<i>E</i>	967.2 (2.3)	21.4	2.57
<i>F</i>	1021.8 (10.1)	17.1 (0.45)	1.71 (0.12)
<i>G</i>	1218.0 (4.2)	15.1 (0.32)	-
<i>H</i>	897.4 (9.0)	18.7	-
<i>I</i>	-	12.6	-

Table 3.2 : Mechanical properties for each grade. The values in the parenthesis denote standard deviations. - notation means N/A (not available).

Hardness was measured on a Vickers hardness scale (HV, 30-kg load). Five measurements of each grade were averaged for the mean hardness. All the measured hardness values are at the vicinity of mean hardness, and the standard deviations (grades *A-H*) of each grade range from 2 to 10 kg/mm², which is on the order of 1 % or less.

To measure the fracture toughness, a 10000 kg load cell was used for pre-cracking of test specimens and a 230 kg load cell was used for breaking specimens in the four-point bending failure test. The specimen dimensions were 6 mm high, 3 mm wide, and 45 mm long. For statistically reliable information, 20 measurements for each specimen grade were performed. The standard deviations in the Table 3.1 (for grades *A-D*, *F*, and *G*) fall in the range of 0.29~0.45 MPa, which are in the range of 2 to 3 %.

The dimensions for the transverse rupture strength (TRS) test specimens were 5×5×20 mm³. More than 15 independent measurements were averaged, and the standard

deviation for three grades (grades *A*, *B*, and *F*) ranges from 0.05 to 0.13 GPa, which range from 3 to 7 %.

3.3 Results

Grade	d [μm]	L [μm]	L^* [μm]	λ [μm]	λ^* [μm]	f'_c	f_c	C	N	Aspect Ratio (manual)
<i>A</i>	5.31 (3.19)	5.25 (3.89)	5.28	1.72 (1.35)	1.69	0.8992	0.8852	0.5951	6.94 (3.15)	1.52
<i>B</i>	1.65 (0.97)	1.58 (1.20)	1.61	0.53 (0.39)	0.51	0.8992	0.8847	0.5912	6.87 (2.55)	1.50
<i>C</i>	1.41 (0.90)	1.44 (1.06)	1.47	0.63 0.48)	0.64	0.8367	0.8220	0.5007	6.78 (3.29)	
<i>D</i>	1.53 (0.83)	1.43 (1.02)	1.50	0.68 (0.51)	0.64	0.8367	0.8239	0.5020	6.45 (2.35)	1.33
<i>E</i>	1.40 (0.88)	1.41 (1.12)	1.44	0.96 (0.81)	0.99	0.6949	0.6919	0.3513	6.16 (2.89)	1.18
<i>F</i>	3.12 (1.80)	2.94 (2.10)	3.01	1.25 (0.98)	1.27	0.8443	0.8316	0.5213	6.69 (3.28)	
<i>G</i>	2.85 (1.59)	2.59 (1.89)	2.65	1.06 (0.83)	1.02	0.8675	0.8531	0.5510	6.75 (2.59)	1.43
<i>H</i>	6.67 (3.69)	6.27 (4.08)	6.30	2.32 (2.09)	2.26	0.8832	0.8659	0.5679	8.80 (4.00)	
<i>I</i>	0.90 (0.45)	0.79 (0.57)	0.82	0.38 (0.28)	0.35	0.8815	0.8322	0.5272	6.84 (2.46)	6.00

Table 3.3 : Summary of the results of microstructures.

d : carbide grain diameter by direct measurements, L : carbide grain size by direct measurements, L^* : carbide grain size by stereology (linear-intercept), l : binder mean free path by direct measurements, l^* : binder mean free path by stereology, f'_c : theoretical carbide volume fraction, f_c : measured carbide volume fraction by direct measurements, C : contiguity by direct measurements, N : ave. number of vertices per grain

The measured microstructural parameters are summarized in Table 3.3. The values in parentheses denote standard deviations in the measurements.

3.3.1 Grain size, binder mean free path, and size distributions

The average grain diameter and the average intercept length are comparable. The ratios of the two values fall in the range of 0.99 to 1.13, such that the intercept length, L , is usually smaller than the effective grain diameter, d . The stereologically derived mean intercept length is comparable to the measured value. The assumption of the circular section plane in the calculation of d leads to the systematically larger values. Random intercept lengths through the polygonal carbide grains are, on average, smaller than through a circle of the same area. Note that the volume fraction of the carbide phase (f_c) is systematically lower than the value calculated on the basis of the starting materials. This is expected, since some of the carbide will dissolve into the Co during sintering. The amount of carbide lost to dissolution varies from 0.5 to 5.6 %, which is less than the equilibrium value of about 10 % at the 1400 °C WC-Co eutectic.

The distributions of grain sizes were found to be surprisingly uniform. When the size distributions are normalized, all exhibit uni-modal and that log-normal size distributions are close to the Gaussian distributions (see Fig. 3.5(a) and Fig. 3.6). For comparison, the Gaussian, Hillert [6, 8], and Louat [7, 8] distributions are also shown. A Gaussian distribution is often called a ‘normal distribution’ which is given by:

$$f(R) = \frac{1}{\sigma\sqrt{2\pi}} \exp\left[\frac{-(R - \mu)^2}{2\sigma^2}\right] \quad (3.5)$$

where $f(R)$ is the probability function, R is the variate (grain diameter or radius), μ is the mean of the variate, and σ is the variance (standard deviation) of the variate. The so-called ‘standard normal distribution’ can be expressed by taking $\mu=0$, and $\sigma=1$:

$$f(R) = \frac{1}{\sqrt{2\pi}} \exp\left[-\frac{R^2}{2}\right] \quad (3.6)$$

Both of the Hillert and Louat distributions come from mean field grain growth theory. The mean field theory deals with the normal growth of a grain that is completely embedded in an averaged environment. In the mean field theory, the overall flux (j) of particles is given by the sum of the diffusion term and the drift velocity term:

$$j = -D \frac{\partial f}{\partial R} + f v \quad (3.7)$$

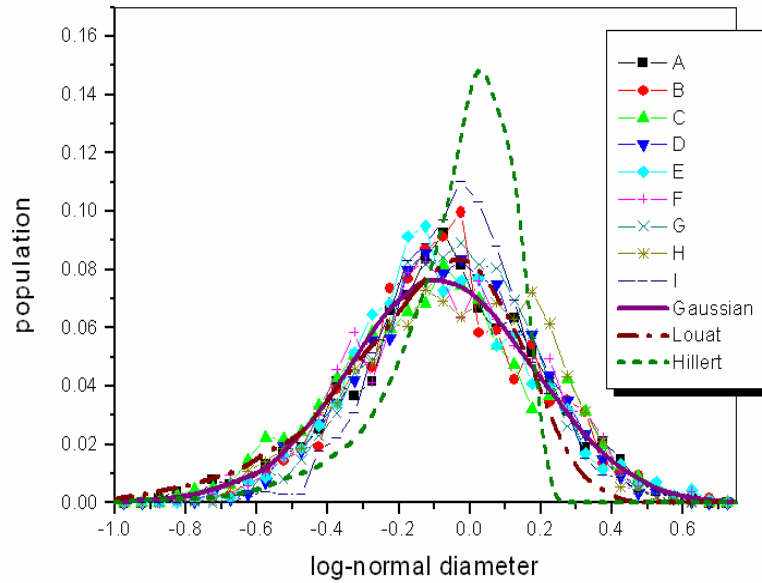
where f is the frequency or probability of finding a particle size R , D is the diffusivity, and v is the velocity of particle size R . Using the continuity equation, the time derivative of the probability function (f) can be written as:

$$\frac{\partial f}{\partial t} = \frac{\partial}{\partial R}(-j) = \frac{\partial}{\partial R}\left(D \frac{\partial f}{\partial R}\right) - \frac{\partial}{\partial R}(f v) \quad (3.8)$$

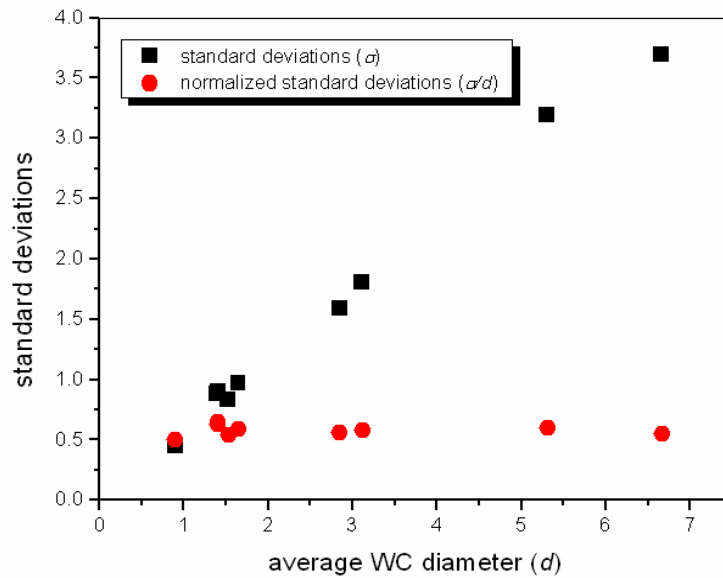
In Eq. (3.8), Hillert [6] considered only the drift velocity term ($\frac{\partial f}{\partial t} = -\frac{\partial}{\partial R}(f v)$) while Louat [7] considered only the diffusion term ($\frac{\partial f}{\partial t} = \frac{\partial}{\partial R}\left(D \frac{\partial f}{\partial R}\right)$).

The separate distributions are illustrated in Fig. 3.6. The largest deviation from the ideal behavior was in specimen *I* (the plate-like grade) and *H* (the non-angular grade).

The standard deviations of the distributions scale linearly with the mean grain size and the normalized standard deviations are in the range of 0.55 to 0.60 in all of the grades.



(a)



(b)

Fig. 3.5 : Plots of the carbide grain size distributions. (a) The distributions of grain sizes for each grade. For comparison, Gaussian, Louat [7], and Hillert [6] distributions are also shown. (b) Variation of the standard deviation (σ) as a function of the grain size. The normalized standard deviations (σ/d) for each grade are almost constant (0.55-0.60).

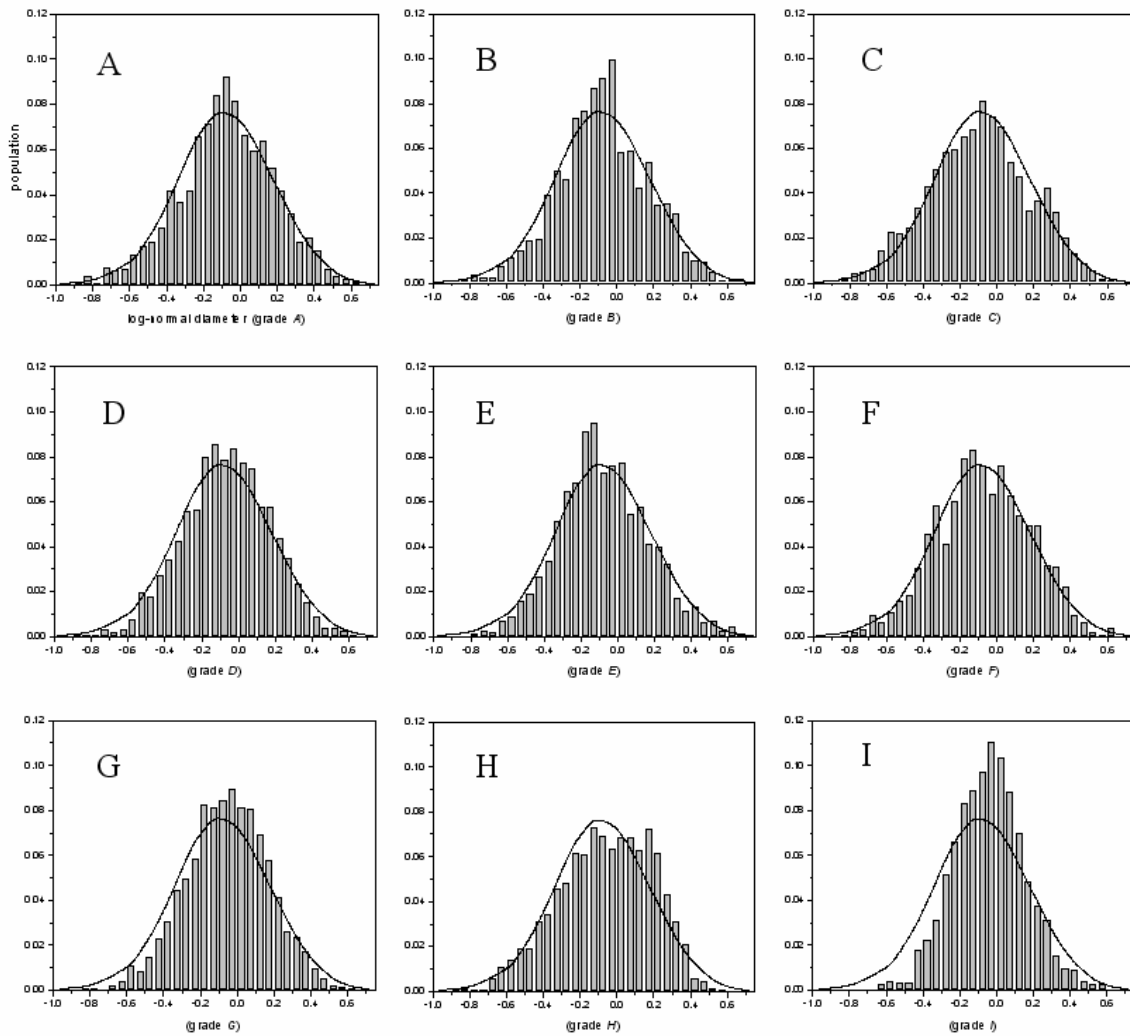


Fig. 3.6 : Carbide grain diameter distributions for each grade. Each plot is based on ~2500 WC grains. Gaussian distribution is compared with the distributions of nine grades.

The results for the binder mean free paths are summarized in Fig. 3.7 and they were compared to stereological estimates, λ_1^* and λ_2^* . It seems clear from this comparison that λ_1^* , which includes the sample contiguity of the carbide phase, is the

correct quantity. The log-normal distribution of binder mean free paths (not shown) is Gaussian and it is similar to the grain size distribution.

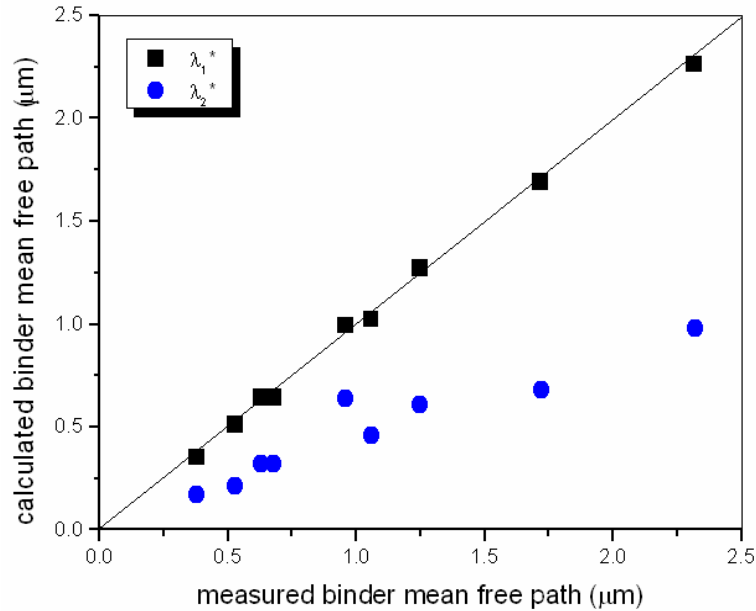


Fig. 3.7 : Comparison of the measured binder mean free path (direct measurements) and calculated binder mean free path (stereology) using stereological equations (3.4a) and (3.4b).

3.3.2 Contiguity of carbide phase (*C*)

The contiguity measurements are linear with the volume fraction of the binder phase, as illustrated in Fig. 3.8. Note that the contiguity is independent of the grain size. The average diameters of specimens *A* and *F* are more than three times larger than *B* and *I*, yet the contiguity of *A* and *B* are essentially the same, as are those of *F* and *I*. When one considers the uniformity of the distributions of grains sizes and binder mean free paths, the independence of the contiguity on grain size is not too surprising. Since the normalized size distributions in all of the microstructures are approximately the same, topological properties such as the contiguity should also be scale invariant. While this

conclusion is consistent with German's predictions [9], there are some reports in the literature which suggest that contiguity increases with grain size and depends on the sintering process [10]. However, we note that the apparent contiguity would be expected to decrease in fine-grained materials as the tail of the size distribution falls below the detection limit of the microscopic probe.

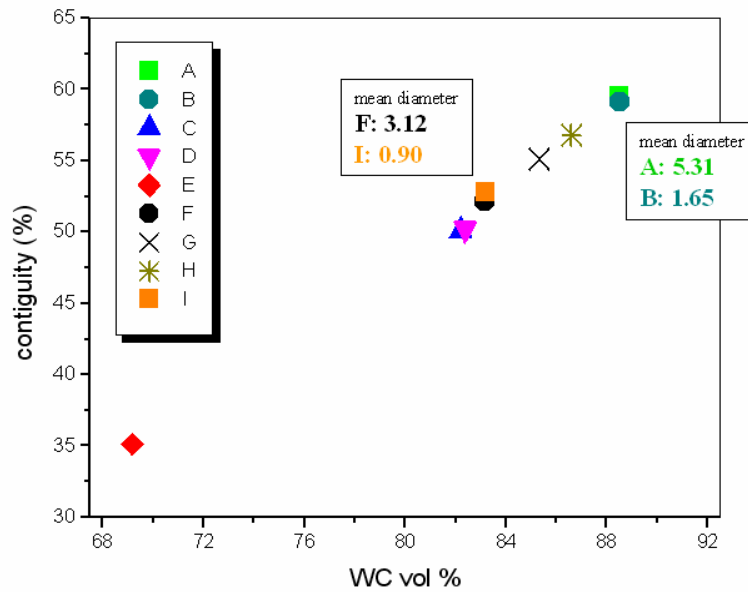


Fig. 3.8 : Variation of the contiguity of carbide phase as a function of the carbide volume fraction.

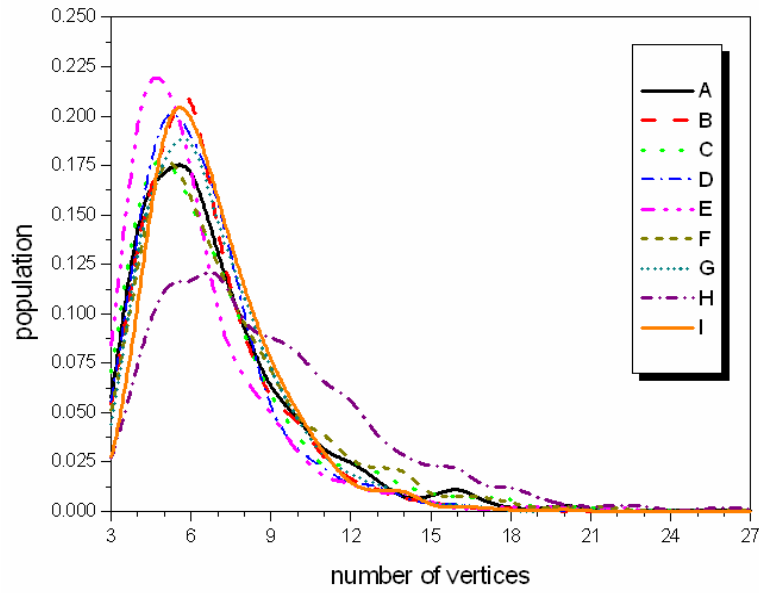
3.3.3 Carbide crystal shape

While the contiguity is not closely linked to the average grain size, it can potentially vary with the crystal shape. One aspect of a crystal's shape that can be characterized is the angularity, which we take to be inversely related to the number of vertices bounding a polygonal particle. In other words, a wedge shaped crystal with three vertices in a section plane has the maximum angularity. Since each carbide grain has been approximated as a polygon, we use the average number of vertices per grain (N) as a

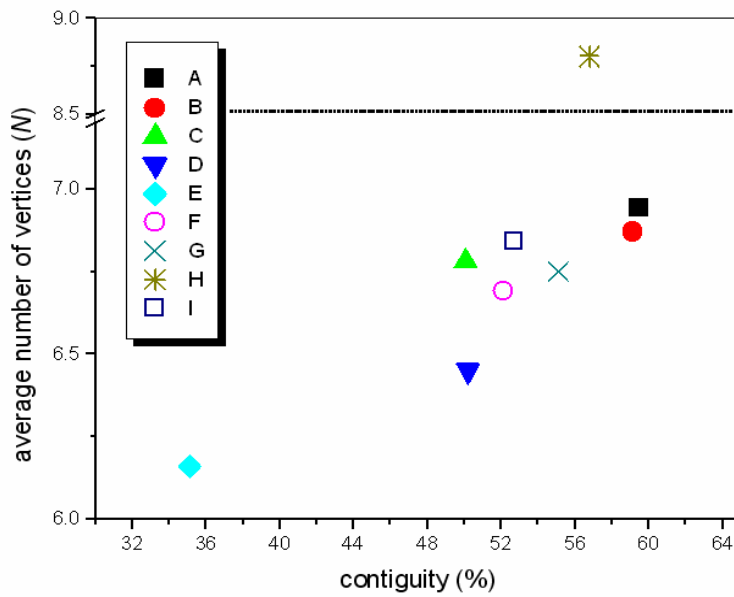
measure of the angularity. Since N has an inverse relationship with angularity, N can be thought of as a measure of inverse angularity. As can be seen in Table 3.3, the average number of vertices for most of the grades varies between 6 and 7, but the inverse angularity of grade H is almost 9. The distributions of inverse angularity are shown in Fig. 3.9(a). Separate distributions for each grade are given in Fig. 3.10. Based on this comparison, grade H clearly has a lower angularity than the others. The measurements exhibit a weak dependence on contiguity, as illustrated in Fig. 3.9(b). The dependence is most easily attributed to impingement effects. Since the contiguity scales linearly with the carbide volume fraction, the number of vertices increases as the amount of binder decreases. As crystals impinge on one another more frequently, they have more vertices.

The average three-dimensional shapes of the carbide crystals have also been determined. These measurements were conducted using a stereological technique [11, 12] that will be described in Section 4.3. In all cases, it was found that the average particle shape is a trigonal prism, with three $\{10\bar{1}0\}$ prism facets and two $\{0001\}$ facets (see Fig. 2.3(a)). With one exception, the crystals are approximately equiaxed. The ratio of the crystal's height to the base varied from 1.2 to 1.5. The one exception was sample I , which has an aspect ratio of 6. It should be emphasized that these average shapes are derived only from the WC interfaces in contact with Co. In reality, the shapes of individual crystals are always truncated in one way or another because of impingement. It is interesting to note that the aspect ratio is linked to the contiguity and/or volume fraction of carbide phase (except specimen I , the plate-like grade). The carbide shape is more equiaxed in a more Co volume fraction sample. This result will be presented in Section 4.3.2 (see Fig. 4.10). The mechanical properties are apparently unaffected by the aspect

ratios, since the properties of specimen *I* (with an aspect ratio 6) do not differ significantly from predictions based on measurements of materials with equiaxed carbides (this will be discussed in Section 4.4).



(a)



(b)

Fig. 3.9 : Number of vertices. (a) Distributions of the number of vertices per grain for each specimen grade, (b) variation of average number of vertices as a function of contiguity.

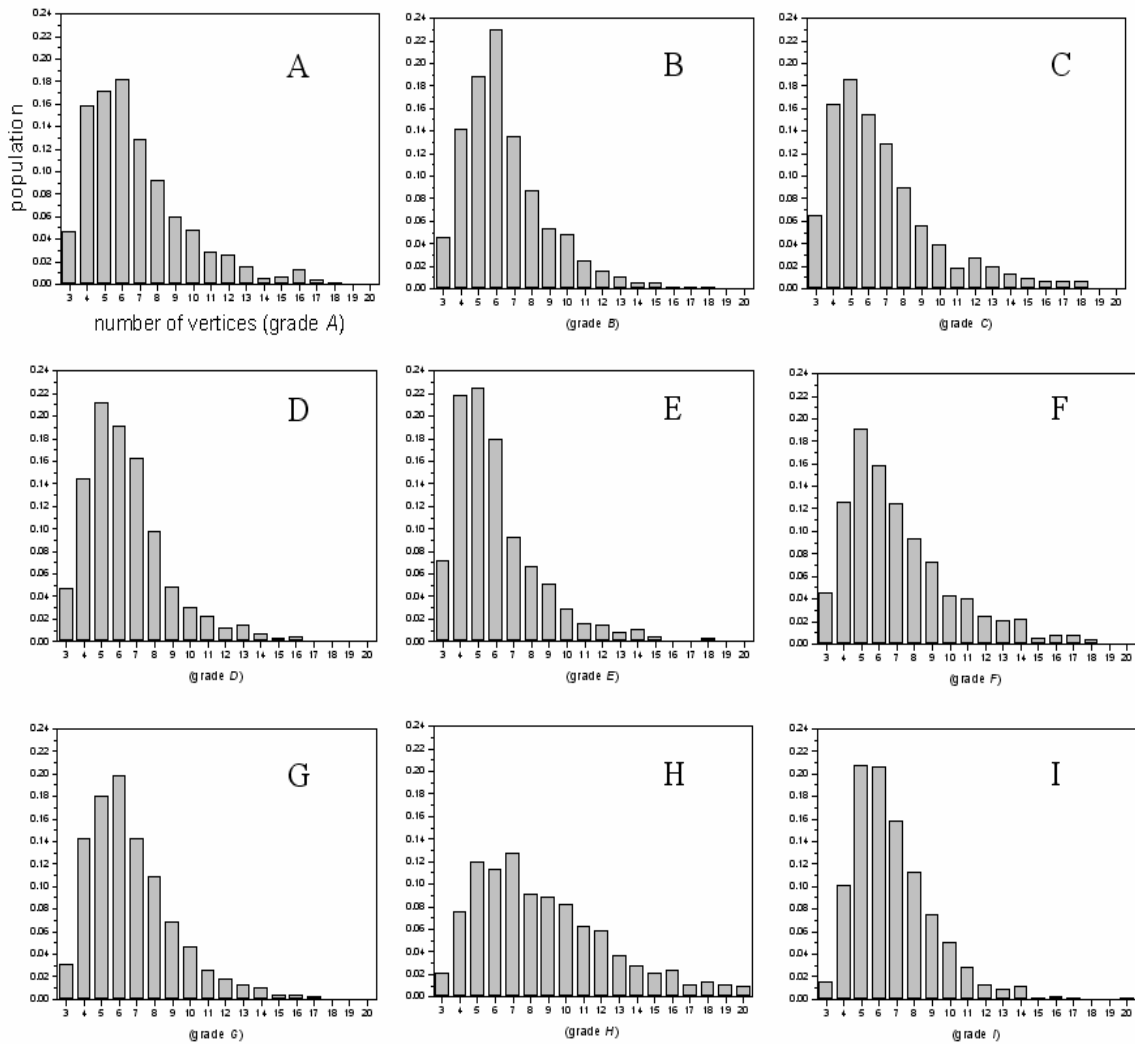


Fig. 3.10 : Distributions of the number of vertices for each grade. All distributions are based on ~2500 WC grains.

3.3.4 Orientation and misorientation distributions (see Section 4.4 for details)

While no grain orientation texture was detected in these specimens, there were significant features in the misorientation texture. All the specimens had a high population of WC/WC grain boundaries that have a 90° twist misorientation about the $[10\bar{1}0]$ axis

(see Fig. 4.16(a)). Stereological analysis of these boundaries indicates that the most common habit plane for these boundaries is $\{10\bar{1}0\}$. Because of the high planar coincidence at this particular interface, it has been argued to be a low energy boundary that resists wetting by liquid Co during processing. The specimens also have an elevated population of boundaries with a 30° misorientation about the $[0001]$ axis (see Fig. 4.16 (b) and (c)).

A quantitative analysis of the population of these boundaries has shown that there are approximately constant fractions of special boundaries in all straight angular grades; 90° and 30° boundaries occupy 11~14 % and 2~3 % of the total WC/WC boundaries, respectively. Currently, therefore, it is not feasible to correlate the contents of these special boundaries with properties. However, if crack initiations at WC/WC boundaries and/or crack propagation along these WC/WC boundaries (intergranular fracture) are important factors for determining the failure of the composites, the populations of those strong special interfaces remain as an important parameter to potentially enhance the mechanical properties of WC-Co composites.

3.4 Correlation with mechanical properties

The data in Table 3.2 and Table 3.3 reflect the well-known inverse correlation between hardness and fracture toughness. Also, experimentally measured transverse rupture strength (TRS, fracture strength) values are listed. In seeking correlations with the microstructural parameters, we must first decide which parameters have a demonstrated influence on the mechanical properties. An examination of the correlations indicates that

the angularity and aspect ratio do not influence the hardness, toughness or fracture strength (TRS) in a significant way. On the other hand, the grain size, contiguity, binder mean free path, and carbide volume fraction do correlate with the properties of the materials, although the last three of these quantities are not independent. The contiguity is linearly related to the binder volume fraction (see Fig. 3.8), and the binder mean free path is determined entirely by the carbide volume fraction and contiguity. Therefore, we limit the analysis to the dependence of hardness and toughness on average carbide diameter (d) and contiguity of carbide phase (C).

3.4.1 Hardness

For the hardness, we assume that the hardness and yield strength are related and propose an empirical expression in analogy to the Hall-Petch relation:

$$H = \frac{a_1}{\sqrt{d}} + a_2 C + a_3 \quad (3.9)$$

where the coefficients a_1 , a_2 , and a_3 are determined by generalized least squares fitting. As a test of the generality of the analysis, we fit only the properties of grades *A* through *G*. Grades *H* (the non-angular, coarse grained grade) and *I* (the plate-like, fine-grained grade) represent excursions from the others in terms of the particle aspect ratios, grain size, angularity, and composition. Therefore, correlations with the properties of grades *H* and *I* can then be used as a test of the generality of the expression. Based on the grades *A*~*G*, the fitted hardness equation as a function of WC grain diameter (d) and contiguity (C) is:

$$H (HV, kg / mm^2) = \frac{1057}{\sqrt{d}} + 2196 C - 726, (0.9 < d < 7 [\mu m], 0.7 < C < 0.9) \quad (3.10)$$

where d has the units of [μm]. In Fig. 3.11, measured Vickers hardness (HV) of nine grades is compared with the calculated hardness using Eq. (3.10). Also, the relative errors are plotted at the bottom. The fitting results for grades H and I , as well as grades $A-G$, show good agreement with the measured hardness; the relative errors are within 9 %. This result suggests that the empirical equation (Eq. (3.10)) can be applied to predict hardness in a wide range of microstructures, including those with WC particle diameter of 0.9-7 μm , and carbide volume fraction of 0.7-0.9, which covers most of the commercial WC/Co products. Furthermore, the equation is useful even in composites with different WC/Co interfacial characters (grade H , non-angular) and/or alloying elements (grade I).

The success of the fitted equation is ascribed to the homogeneity of the microstructures. The similarities of grain size distributions of each grade and the strong relationship between contiguity (C) and volume fraction (f_c) yield to a simple linear fitting equation consisting of two parameters, carbide grain diameter (d) and contiguity (C).

To test the empirical hardness equation (Eq. (3.10)) and to compare with other models, we applied the microstructural parameters of nine specimen grades to the past models [1, 4]. The results and relative errors are shown in Fig. 3.12. Fitting the hardness by Eq. (3.10) shows better performance than the previous models. While the past models have some physical rationale, they also include empirical constants (see Eq. (2.28)~(2.31)) [1, 4, 14, 15], and they are thus comparable to the current approach. The superior performance of Eq (3.10) is most likely connected to the improved measurements to which the expression was fit, not the functional form. Therefore, we expect that if these

empirical constants were modified to reflect more accurate measurements of the microstructural characteristics, the predictions would improve and be similar to the expression presented here.

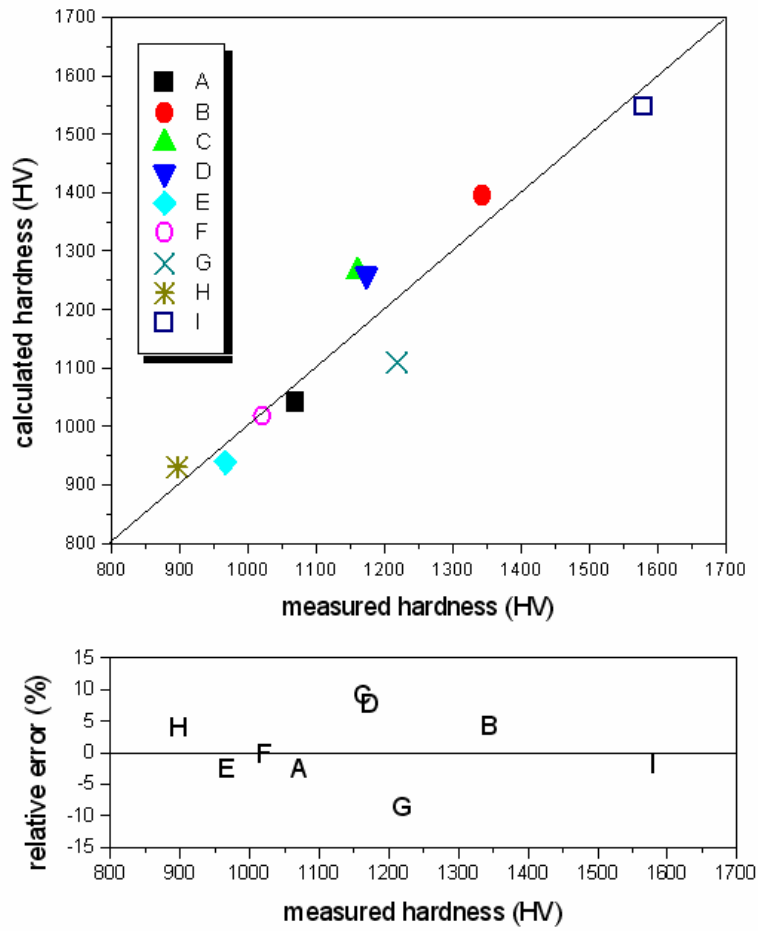


Fig. 3.11 : Comparison of the calculated hardness by empirical equation with experimentally measured data.

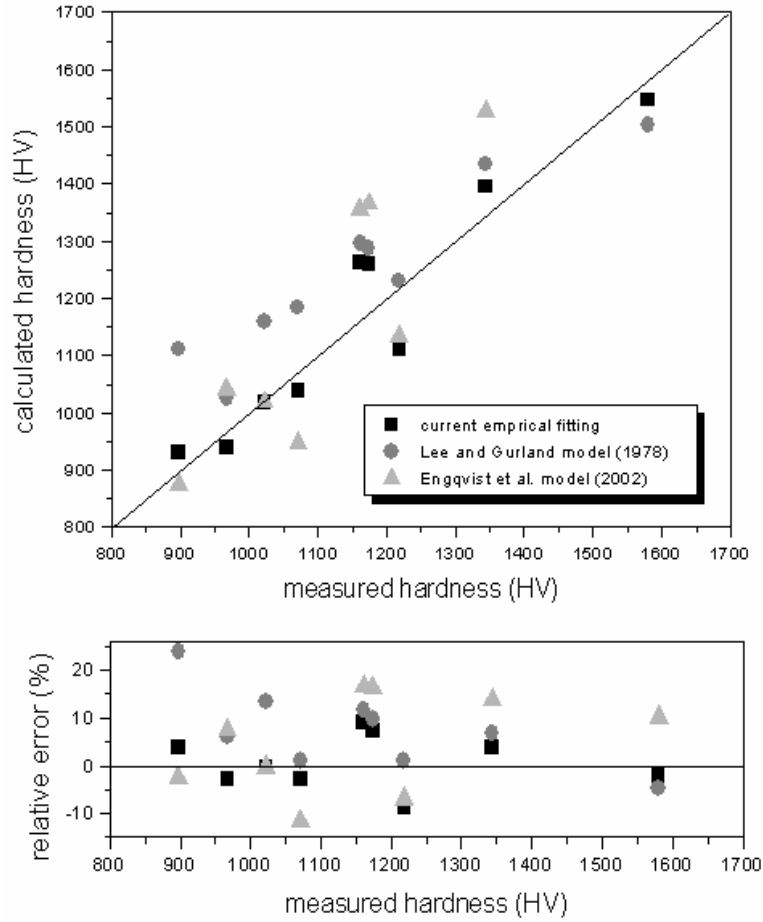


Fig. 3.12 : Comparison of the calculated hardness by empirical equation and the previous models with experimentally measured data.

3.4.2 Fracture toughness

For fracture toughness, we assume a strong inverse relation between hardness and fracture toughness, and propose following formula:

$$K_{IC} = a_1 \sqrt{d} + \frac{a_2}{C} + a_3 \quad (3.11)$$

where the coefficients a_1 , a_2 , and a_3 are also fitting constants. Again, to test the generality, we found the empirical coefficients using measurements for grades A through G.

$$K_{IC} (MPa\sqrt{m}) = 5.59\sqrt{d} + \frac{8.32}{C} - 8.98, (0.9 < d < 7 [\mu\text{m}], 0.7 < C < 0.9) \quad (3.12)$$

The results and relative errors are given in Fig. 3.13. As is the case with hardness, the fitted equation for fracture toughness produces results coinciding with the experimental data. The fact that fracture toughness of grades *H* and *I* also agree with the experimental value validates the generality of fitting equation. The relative errors are within 9 %. Again, microstructural homogeneity (strong linearity between contiguity and volume fraction, and the scale independent carbide grain size distribution) is assumed to be the origin of the success of the fitted equations. The homogeneity allows us to predict fracture toughness based on two basic microstructural parameters (WC grain diameter and contiguity). The primary difference between the empirical equation and previous models is that the binder mean free path is the most important parameter in the past models [2, 3, 5, 15-17]. In the present equation, the effect of binder mean free path is incorporated indirectly in the size and contiguity. It is, of course, possible to include the binder mean free path, but this is not an independent variable. Again, the empirical equation presented here is applicable to a wide range of microstructures with WC grain diameter of 0.9-7 μm and carbide volume fraction of 0.7-0.9.

To test the relevance of the current empirical equations, we compared the fitting results with those of past models [2, 3, 5]. As can be seen in Fig. 3.14, it is clear that the results are superior to those of past models. Using Eq. (3.10) and Eq. (3.12), accurate measurements of grain size and contiguity make it feasible to estimate the hardness and fracture toughness simultaneously.

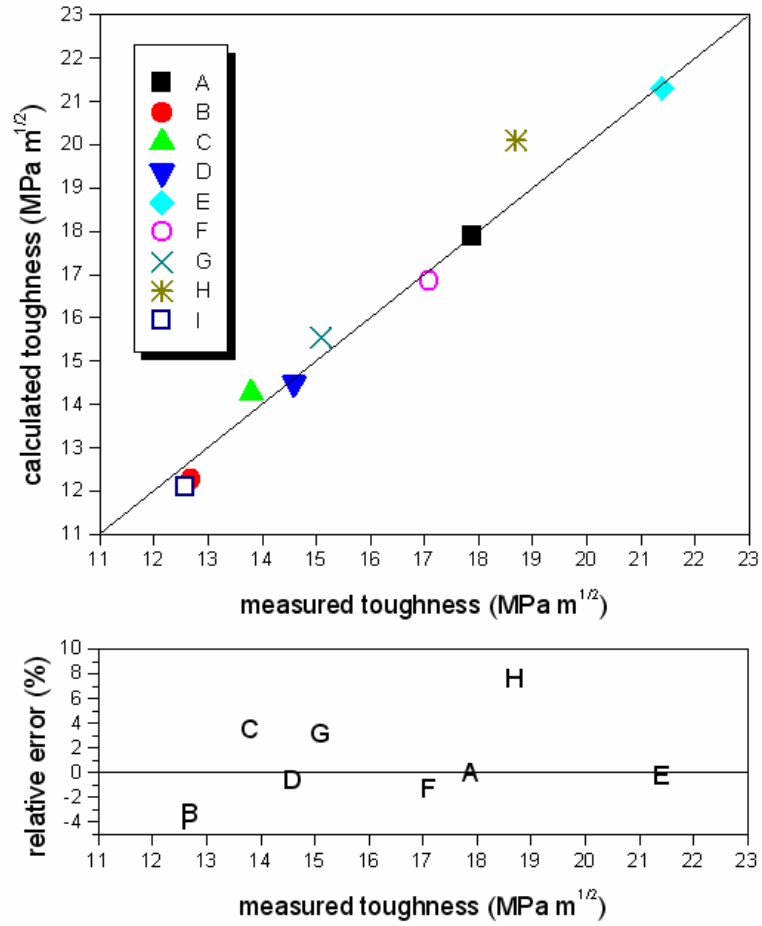


Fig. 3.13 : Comparison of the calculated fracture toughness by empirical equation with experimentally measured data.

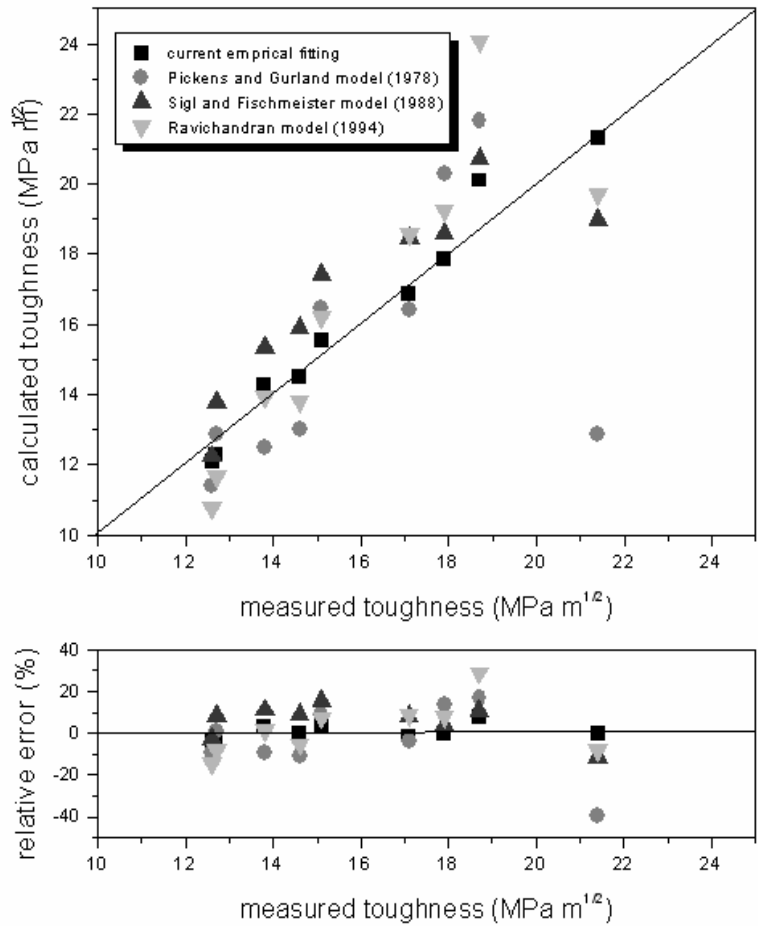


Fig. 3.14 : Comparison of the calculated fracture toughness by empirical equation and the previous models with experimentally measured data.

3.5 Summary

Atomic force microscopy (AFM) and orientation imaging microscopy (OIM) have been used to determine the WC/WC boundary and WC/Co interface positions in WC-Co composites. Direct measurements of the carbide and cobalt area fractions show that the distributions of carbide grain size and binder free path are log normal and Gaussian, and that there is a very strong linear correlation between the volume fraction of the binder and the carbide contiguity. The number of vertices per carbide grain is slightly

influenced by the Co volume fraction. Empirical expressions involving the two microstructural parameters with the most significant effect on properties, the grain size and the carbide contiguity, fit well with the experimentally measured hardness and fracture toughness data.

3.6 References

- [1] H.C. Lee and J. Gurland, “Hardness and Deformation of Cemented Tungsten Carbide”, *Mater. Sci. Eng.*, **33**, 125 (1978)
- [2] J.R. Pickens and J. Gurland, “The Fracture Toughness of WC-Co Alloys Measured on Single-edge Notched Beam Specimens Pre-cracked by Electron Discharge Machining”, *Mater. Sci. Eng.*, **33**, 135 (1978)
- [3] L.S. Sigl and H.F. Fischmeister, “On the Fracture Toughness of Cemented Carbides”, *Acta Metall.*, **36**, No. 4, 887 (1988)
- [4] H. Engqvist, S. Jacobson, and N. Axen, “A Model for Hardness of Cemented Carbides”, *Wear*, **252**, 384 (2002)
- [5] K.S. Ravichandran, “Fracture Toughness of Two Phase WC-Co Cermets”, *Acta Metall. Mater.*, **42**, No. 1, 143 (1994)
- [6] M. Hillert, “On Theory of Normal and Abnormal Grain Growth”, *Acta Metall.*, **13**, No. 3, 227 (1965)
- [7] N.P. Louat, “Theory of Normal Grain Growth”, *Acta Metall.*, **22**, No. 6, 721 (1974)
- [8] H.V. Atkinson, “Theories of normal grain growth in pure single phase systems”, *Acta metall.* **36**, No.3, 469 (1988)

- [9] R.M. German, “The Contiguity of Liquid-Phase Sintered Microstructures”, *Metall. Trans. A*, **16**, No. 7, 1247 (1985)
- [10] J. Gurland, “New Scientific Approaches to Development of Tool Materials”, *Int. Mater. Rev.*, **33**, No. 3, 151 (1988)
- [11] D.M. Saylor and G.S. Rohrer, “Determining Crystal Habits from Observations of Planar Sections”, *J. Am. Ceram. Soc.*, **85**, 2799 (2002)
- [12] C.-S. Kim and G.S. Rohrer, “Geometric and Crystallographic Characterization of WC Surfaces and Grain Boundaries in WC-Co Composites”, *Interface Sci.*, **12**, 19 (2004)
- [13] M.T. Laugier, “A microstructural model for hardness in WC-Co composites”, *Acta Metall.*, **33**, No.11, 2093 (1985)
- [14] B. Roebuck, E.G. Bennett and M.G. Gee, “Grain size measurements methods for WC/Co hardmetals”, 13 International Plansee Seminar, Reutte, Austria, vol.2, 273 (1993)
- [15] H. Doi, Y. Fujiwara and K. Miyake, “Mechanism of plastic deformation and dislocation damping of cemented carbides”, *Trans. Metall. AIME*, **245**, 1457 (1969)
- [16] M. Nakamura and J. Gurland, “The fracture toughness of WC-Co two-phase alloys – A preliminary model”, *Metall. Trans. A*, **11A**, 141 (1980)
- [17] L.S. Sigl and H.E. Exner, “Experimental study of the mechanics of fracture in WC-Co alloys”, *Metall. Trans. A*, **18A**, 1299 (1987)

Chapter 4

Analysis of Interfaces in WC-Co Composites

In this chapter, a stereological method for the quantitative analysis of the binder/carbide and carbide/carbide interface character distributions in WC-Co composites is described. To quantify the types of interfaces in WC-Co composites using stereology, geometrical and orientation data were obtained using atomic force microscopy (AFM) and orientation imaging microscopy (OIM). Based on the stereological analysis of the interface traces on the plane of observation, preferred habit planes of binder/carbide interfaces have been determined, and the quantitative surface area ratio of habit planes was calculated. By the measurements of WC grain boundary misorientations, we demonstrate that there are preferred misorientations and habit planes also in the carbide/carbide boundaries.

4.1 Samples

The same nine specimen grades (see Section 3.1) are used to reveal the interface character types of WC-Co composites. The distribution of WC/Co interfaces were explored for all nine grades (grades *A~I*) and the distribution of WC/WC boundaries have been investigated mainly for the seven straight angular grades (grades *A~G*).

4.2 Stereological method for interface characterizations

The shapes of three-dimensional crystals are usually observed in the form of two-dimensional planar sections in micrographs. To resolve the three-dimensional shapes of such crystals, several techniques might be applied. Among them, serial sectioning is the most commonly used technique. It is, however, labor-intensive, time-consuming and resolution-limited when the sectioning is accomplished by polishing. To make three-dimensional images of crystals, 3DXDM (three-dimensional X-ray diffraction microscopy) can also be used. However, this apparatus is still in development, not yet widely available, and also has limited resolution. In this thesis, we used a recently developed stereological method [1-7] to determine the three-dimensional shapes of WC crystals embedded in a Co binder. This method was applied not only to estimate the WC habit planes (for investigating the three-dimensional form of carbides) in contact with Co, but also to characterize the distribution of WC/WC grain boundary planes.

4.2.1 Method overview [1-7]

i) Basic idea

In two-dimensional micrographs, sections of faceted crystals (WC crystals) appear as polygons, where each line segment, l_{ij} , comes from a different bounding plane (see Fig. 4.1(a)). While the actual plane that created the observed line segment is unknown, it is certain to belong to the set of planes (n_{ijk}) whose normals are perpendicular to the segment (see Fig. 4.1(c)). If the crystal orientation (g) is known, then

the possible habit planes can be transformed to the crystal reference frame, $\mathbf{n}'_{ijk} = g\mathbf{n}_{ijk}$. On a stereographic projection, the planes \mathbf{n}'_{ijk} lie on a great circle perpendicular to the position of the line segment (see Fig. 4.1(d)). By observing many segments from different crystals, a corresponding number of sets of possible planes (each on a different great circle) that might be responsible for the observations are also identified. These observations are used to calculate the probability, $p(\mathbf{n}')$, that a given length of line on the perimeter of a random section plane falls on a plane with the orientation \mathbf{n}' according to the following equation:

$$p(\mathbf{n}') = \frac{\sum_{i,j,k} g_i \mathbf{n}_{ijk} |L_{ij}|}{\sum_{i,j,k} |L_{ij}|} \quad (4.1)$$

The key to this analysis is that the correct habit planes are sampled with a high probability: there is at least one habit plane in each set of possible planes, \mathbf{n}_{ijk} . Therefore, the great circles arising from each observed line segment must intersect at the positions of true habit planes and $p(\mathbf{n}')$ will exhibit local maxima at these positions. Because non-habit planes are far more numerous, any specific non-habit plane is observed much less frequently than a correct habit plane.

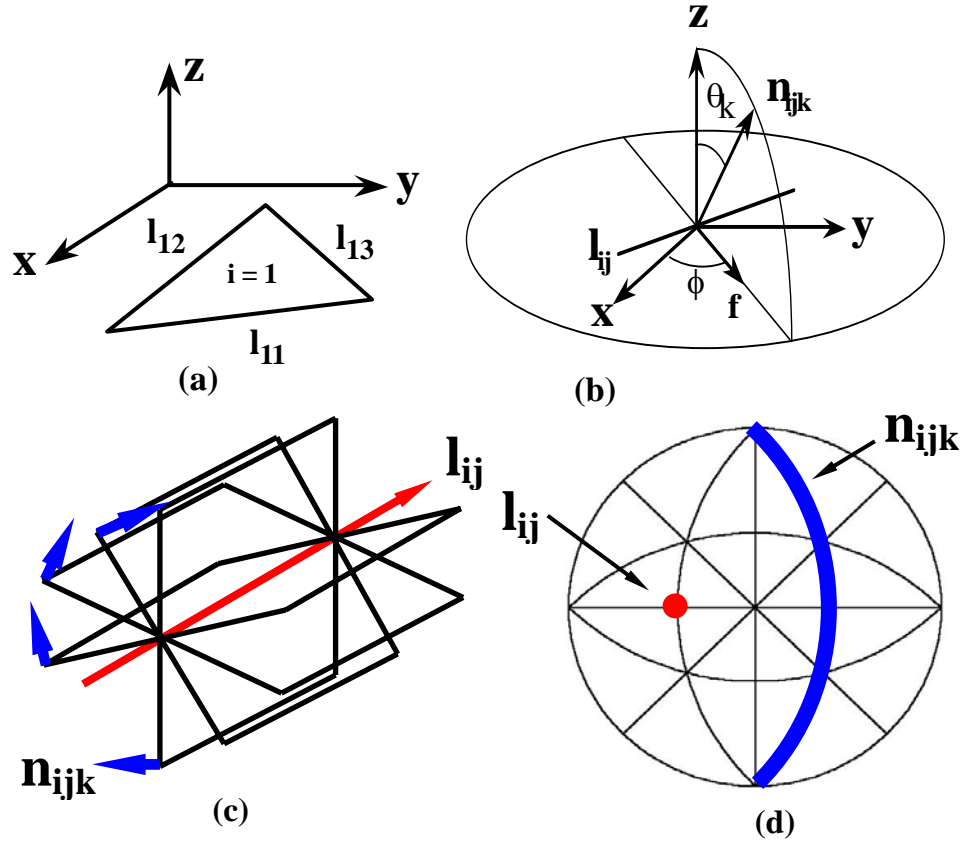


Fig. 4.1 : Schematic illustration of stereological analysis (see text for details).

ii) Trace classification

To determine the crystal shape, it is necessary to know the relative area of each habit plane. Since it is known that the total length of a set of randomly distributed lines intersecting an area is proportional to that area, the ratios of the line lengths associated with each habit plane provide an estimate of the relative surface area [8]. To determine which line segments are associated with each habit plane, we compute the angle (α) between each line segment, l'_{ij} , and each previously identified habit plane, n'_{hkl} , in the crystal reference frame:

$$\alpha = \cos^{-1} \left[\frac{l'_{ij} \cdot n'_{hkl}}{|l'_{ij}| |n'_{hkl}|} \right] \quad (4.2)$$

For the habit plane of origin, $|\alpha-90^\circ|$ ideally vanishes. In practice, discretization and experimental errors lead to finite values of $|\alpha-90^\circ|$. Therefore, we assign a line segment to a habit plane whenever $|\alpha-90^\circ|$ is less than some predetermined tolerance angle, between 3 and 10°. This condition allows us to assign each line length to one of a small set of possible habit planes. After all of the data have been classified in this way, which we call the trace classification procedure, we have the total length of line per habit plane and ratios of these quantities yield the surface area ratio.

Here, we apply this method to both WC/WC grain boundaries and WC/Co interfaces for the two-parameter calculations. For the WC/Co interfaces, the boundary trace, n_{ijk} , is transformed to the WC reference frame. For the WC/WC boundaries, the planes in the zone of the boundary trace, n_{ijk} , are transformed to the crystal reference frame once with each of the orientations of the two adjoining crystals.

iii) Applicability and limitations of stereological analysis

There are two essential preconditions in order to apply the stereology described above. First, polycrystals must be randomly oriented with respect to the sample reference frame. If there is strong orientation texture, the analysis will be biased by the texture. Second, the boundary planes should have random inclinations with respect to the sample surface (see Fig. 4.2 (a)). Since we assume a random distribution of inclinations in the sample reference frame, any deviation from this will create error in the result. Sometimes, most of grain boundaries are parallel to sample normal direction (see Fig. 4.2 (b)). This is a so called ‘columnar boundary structure’. In this case, it is not necessary to use the stereological method to determine grain boundary distributions; knowledge of the grain

orientations, the boundary trace, and the boundary plane normal vector lies in the surface plane completely specifies all the five parameters that describe a grain boundary.

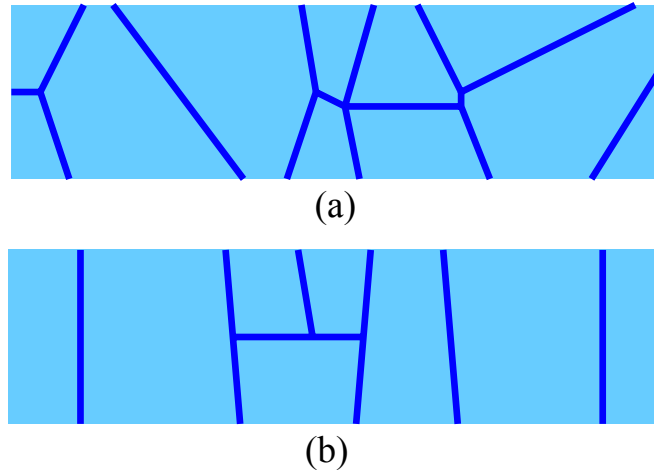


Fig. 4.2 : Schematic cross-sections of boundary structures. (a) Boundary structure with random inclinations, (b) columnar boundary structure.

To use the stereological method, an extensive data set of line segments must be acquired. The analysis is, therefore, limited in an approximate resolution of 10° (see Section 4.2.2 ii) for details, sometimes, we can use a small resolution angle in the misorientation averaged calculations). However, since there exist an enormous number of different types of grain boundaries and the number increases as resolution angle decreases (see Fig. 4.3, there are $\sim 10^4$ to 10^5 distinct types of boundaries with 10° resolution depending on crystal symmetries), 10° resolution remains within a reasonable angular mesoscale range.

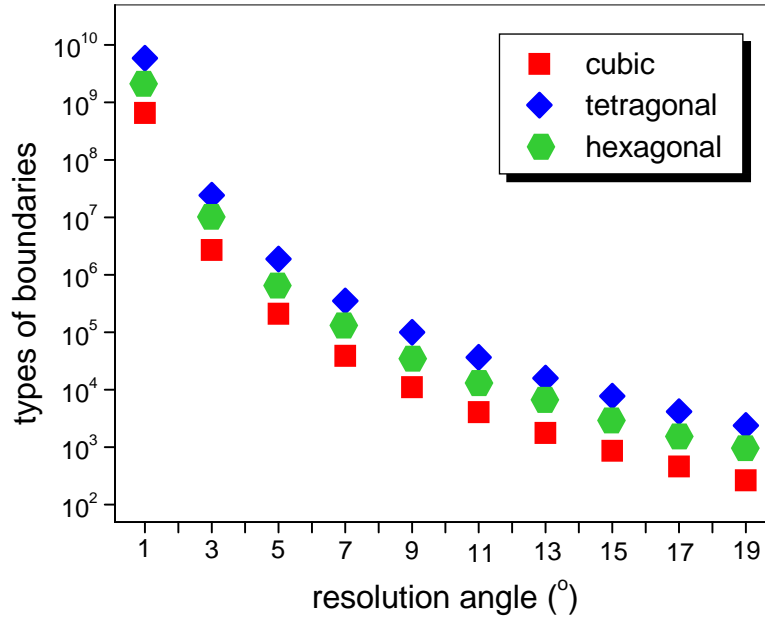


Fig. 4.3 : Different types of boundaries as a function of resolution angles (in degrees). Number of boundary types increases as resolution angle decreases.

4.2.2 Numerical analysis

i) Two- and five-parameter calculations

All line segments for the analysis of interfacial plane distributions were obtained from two methods; by ‘manual hand tracing’ of boundary positions in AFM images using a computer mouse (a program automatically records the vector components of each line segment), and by ‘automatic extraction’ in OIM images using the OIM software (TexSEM Laboratories, Inc. version 3.03) following the method outlined by Wright and Larsen [9]. The line segment data using the manual method is more accurate in positioning exact locations of interfaces but it has limitations in time-and-labor. On the other hand, the line segment data by the automatic method are easily obtained, but less

accurate. Regardless of how they are obtained, each segment is then associated with a set of Euler angles obtained from the OIM image. In this work, we first used data set from the manual tracing based on AFM images, and then applied the line segment data from the automatic extractions through OIM images.

Among the five macroscopic parameters of grain boundaries, the stereological method basically approximates one parameter that describes grain boundary plane inclinations. The other four parameters (three from misorientations and one from boundary planes) can be easily identified in two-dimensional micrographs. In applying this stereology, therefore, we can either ignore (two-parameter calculation, misorientation averaged calculation) or include (five-parameter calculation) the three parameters explaining misorientations. The grain boundary distributions in the two- and five-parameter calculations are represented by the notations $\lambda(\mathbf{n})$ and $\lambda(\Delta g, \mathbf{n})$, respectively, which are the relative occurrences of a grain boundary. Here, Δg and \mathbf{n} denote a misorientation and grain boundary plane normal, respectively (see Section 2.2.1 ii)). For both of the two- and five-parameter calculations, the spherical domain of planes in both the laboratory and crystal reference frames was partitioned into equal area cells with the in-plane angle, ϕ , in the range between 0° and 360° , and the out-of-plane parameter, $\cos\theta$, in the range of 0 to 1 (see Fig. 4.4). In the case of five-parameter calculation, misorientation space must also be discretized. Here, the three Euler angles were used to parameterized the misorientations in the range $\Delta\phi_1=0^\circ$ to 360° , $\cos(\Delta\Phi)=0$ to 1, and $\Delta\phi_2=0^\circ$ to 360° so that the volume of each cell in the Euler angle space is equal. Hence,

the numbers of cells are $\frac{360 \times 90}{\Delta^2}$ (two-parameter calculation) and

$$\frac{360 \times 180 \times 360 \times 360 \times 90}{\Delta^5}$$
 (five-parameter calculation), where Δ is the resolution angle (in degrees). The discretized domain forms ‘accumulator matrix’, in which the observed boundary trace, \mathbf{n}_{ijk} , is added. For the calculation of misorientation averaged boundary plane distributions (two-parameter calculation), there were two dimensional arrays of 324 (=36×9), 1296 (=72×18), or 3600 (=120×30) equal cells, depending on approximate resolution of 10°, 5° or 3°. The five-parameter analysis was conducted using a resolution of 10° which results in five dimensional arrays of $\sim 7.5 \times 10^6$ (=36×18×36×36×9) equal volume cells. The symmetry operators for the hexagonal system were applied to all of the observed line segments in the crystal reference frame.

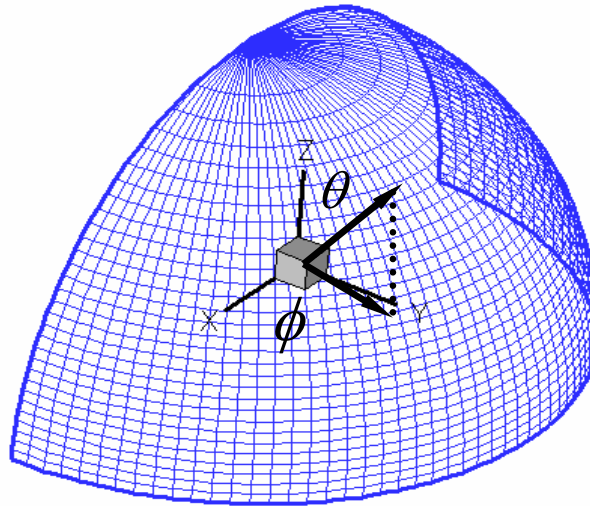


Fig. 4.4 : Illustration of discretized domain for the analysis of binder/carbide interface. Only $\frac{1}{2}$ of the total domain is shown. The out-of-plane angle $\cos\theta$ ranges from 0 to 1, and the in-plane angle ϕ ranges from 0 to 2π .

ii) Number of line segments

For a reliable and smooth plane distribution, experience has shown that each distinguishable cell should contain on average of 100 (two-parameter calculation) and 10 (five-parameter calculation) line segments. Thus, the number of line segments that are required in the analysis is given by:

$$N_2 = \frac{360 \times 90}{\Delta^2 \times O} \times 100 \quad (\text{two-parameter calculation}) \quad (4.3a)$$

$$N_5 = \frac{360 \times 90 \times 360 \times 180 \times 360}{\Delta^5 \times 2 \times O^2} \times 10 \quad (\text{five-parameter calculation}) \quad (4.3b)$$

where N_2 and N_5 are the respective minimum number of line segments for two- and five-parameter calculations, and O is the number of proper symmetry operators for a given crystal system. For example, in a hexagonal system, at least $\sim 2.8 \times 10^3$ line segments are required for the two-parameter calculation with a resolution of 10° ($\Delta=10$, $O=12$), and $\sim 2.6 \times 10^5$ segments are required for the five-parameter calculation with a resolution of 10° ($\Delta=10$, $O=12$). Those number requirements decrease to 1.4×10^3 (two-parameter, $\Delta=10$, $O=24$), 6.5×10^5 (five-parameter, $\Delta=10$, $O=24$) in a cubic system, and they increase to 8.2×10^3 (two-parameter, $\Delta=10$, $O=4$), 2.4×10^6 (five-parameter, $\Delta=10$, $O=4$) in a trigonal system. From this, it is obvious that the five-parameter calculation using the manual tracings is not feasible. Thus, in this work, the two-parameter analysis was carried out based on both of the manual and automatic schemes, but the five-parameter calculation resorted to only the automatic method.

It should be also noted that the above approximations (Eq. (4.3a) and (4.3b)) are for the case of analyses from the automatic tracings. When the manual tracings are used

in the two-parameter calculations, it turned out that the result exhibits a faster convergence to a smooth distribution. For example, we calculated the aspect (base-to-height) ratio of grade G as a function of the number of line segments included in the analysis (see Section 4.2 for the detailed description of aspect ratio calculation). In Fig. 4.5, it seems clear that as the number of analyzed line segments increases, the aspect ratio converges asymptotically and reaches a constant value. The variation of aspect ratio in Fig. 4.5 suggests that, for reliable results, more than ~ 1000 WC/Co interface line segments need to be analyzed. Here, all the results from manual tracings are based on at least 1000 line segments.

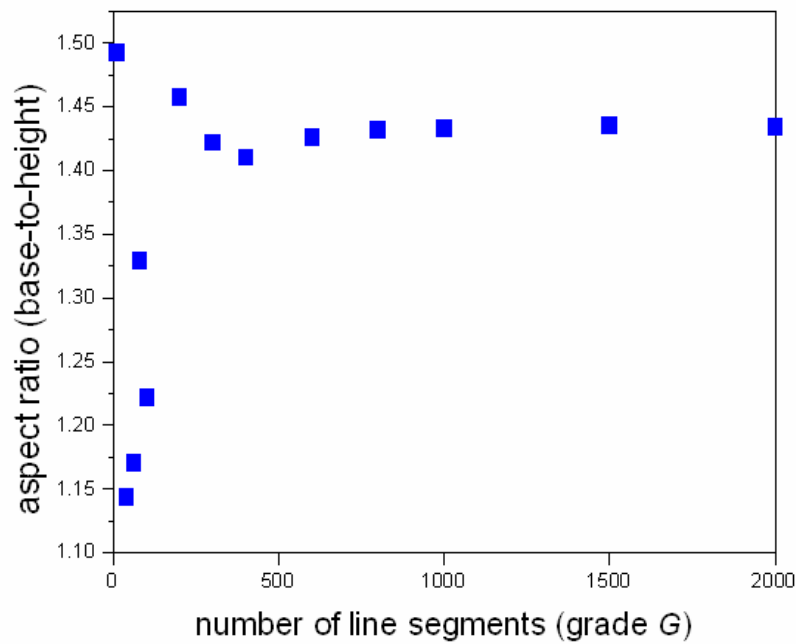


Fig. 4.5 : Variation of aspect ratio with the number of line segments included in the calculations (for grade G).

iii) Background subtraction

Since every observed boundary trace generates a ser of possible plane orientations in the crystal reference frame, it is apparent that too much length has been added to the cells of the accumulator matrix. If the number of possible discrete boundary plane orientations in the crystal reference frame is D ($=\frac{360 \times 90}{\Delta^2}$, where Δ is a resolution angle), the observed length (l_i^O) at i^{th} boundary plane cell is composed of the correct length (l_i^C) from this cell (i) and the incorrect length (l_i^{IC}) associate with some other cell ($j, j=1 \sim D, j \neq i$). In other words, l_i^{IC} is the quantity that has been added to the i^{th} cell but actually came from j^{th} cell ($j, j=1 \sim D, j \neq i$). Now, we define a weighting factor (ω_{ij}) that implies the fraction of traces whose correct boundary plane is j , but also pass through i because they are in the same zone:

$$l_i^O = l_i^C + l_i^{IC} = l_i^C + \sum_{\substack{j=1 \\ j \neq i}}^D \omega_{ij} l_j^C \quad (4.4)$$

Since the weighting factor, ω_{ij} , is largest when i and j are neighboring cells and decreases to a constant value as the angular separation between i and j increases, we divide the incorrectly assigned length, l_i^{IC} , into two parts. The first part originates from nearest neighbor cells and the second part comes from non-nearest neighbor cells. If we approximate the incorrectly assigned length in the j^{th} cell originating from non-nearest neighbor as the average correct length ($\langle l^C \rangle$) in each cell, then the incorrectly assigned length in the i^{th} cell is then given by:

$$\sum_{\substack{j=1 \\ j \neq i}}^D \varpi_{ij} l_j^C \approx \sum_{\substack{j=1 \\ j \neq i}}^D \varpi_{ij} \langle l^C \rangle \quad (j \neq \text{nearest neighbors of } i) \quad (4.5)$$

For any accumulated length, we assume that the probability of a correct assignment is $1/B$ and the probability of an incorrect assignment is $(B-1)/B$, where B is the number of cells on a great circle. Then, the average of incorrectly assigned length from non-nearest cells can be written as:

$$\sum_{\substack{j=1 \\ j \neq i}}^D \varpi_{ij} \langle l^C \rangle = \frac{(B-1)}{B} \langle l^O \rangle \quad (j \neq \text{nearest neighbors of } i) \quad (4.6)$$

Now, taking into consideration that the ratio of $\langle l^O \rangle$ to $\langle l^C \rangle$ is B :

$$\sum_{\substack{j=1 \\ j \neq i}}^D \varpi_{ij} = B - 1 \quad (4.7)$$

For the incorrectly assigned length from nearest neighbor cells, we assume that the length in a cell is approximately equal to the length in a nearest neighbor cell. This approximation is valid as long as the number of cells on a great circle (B) is large enough.

Combining Eq. (4.5) ~ Eq. (4.7) yields:

$$l_i^{IC} = \sum_{\substack{j=1 \\ j \neq i}}^D \varpi_{ij} l_j^C = \sum_{j=NN+1}^D \varpi_{ij} \langle l^C \rangle + \sum_{\substack{j=1 \\ j \neq i}}^{NN} \varpi_{ij} \langle l^C \rangle \approx (1-Z) \frac{(B-1)}{B} \langle l^O \rangle + Z(B-1) l_i^C \quad (4.9)$$

Finally, we reach the following expression:

$$l_i^c \approx \frac{l_i^o + (Z-1) \frac{(B-1)}{B} \langle l^o \rangle}{1 + Z(B-1)} \quad (4.10)$$

Bear in mind that the final equation (Eq. (4.10)) can be applied in a smooth and continuous distribution. The detailed description for this ‘background subtraction’ is available in reference [5].

iv) Data processing; OIM image clean-up

The distribution of grain boundary misorientations was determined from OIM images. The orientation data were processed to remove spurious observations using a ‘grain dilation clean-up’ in the OIM software (TexSEM Laboratories, Inc. version 3.03). Before the clean-up procedure, the crystallographic orientation of the Co phase has been fictitiously assigned as $\phi_l=0$, $\Phi=0$, and $\phi_2=0$, since it was not possible to get reliable diffraction patterns of the Co phase. There are two advantages to this false assignment. First, it makes it easy to distinguish the carbide and binder phase. Second, because the Co phase is indexed as a single orientation, we avoid distorting WC/Co interface positions in the clean-up procedure. This second advantage is especially important when the line segments are extracted automatically. A single orientation was assigned to each carbide grain, by averaging all of the orientations within a single grain that were measured with a confidence index (CI) greater than 0.2. An example of automatic line segment extraction is shown in Fig. 4.6. In the cleaned-up IPF maps (Fig. 4.6 (b) and (c)), the Co phase is colored as red because it has the orientation of $\phi_l=0$, $\Phi=0$, and $\phi_2=0$ (basal orientation). For the comparison of boundaries between original and cleaned-up maps, an image quality (IQ) map is also illustrated. The orientations of individual adjoining grains (g_a and

g_b) were then used to calculate the misorientation ($\Delta g_{ab} = g_a g_b^T$) across each boundary. From the misorientation, the rotation angle ($\omega = \cos^{-1} [(\Delta g_{ii} - 1)/2]$) and components of rotation axis ($r_i = -\varepsilon_{ijk} \Delta g_{jk} / (2 \sin \omega)$) were calculated. Note that the calculation of misorientations is useful only for the WC/WC boundaries. In the distributions presented here, the relative population of boundary types is weighted by boundary length.

In the next two sections, the results for WC/Co interfaces and WC/WC boundaries will be discussed separately. As examples, grades *E* and *A* will be discussed in detail and compared to summary results from the other grades for the WC/Co and WC/WC interface distributions, respectively.

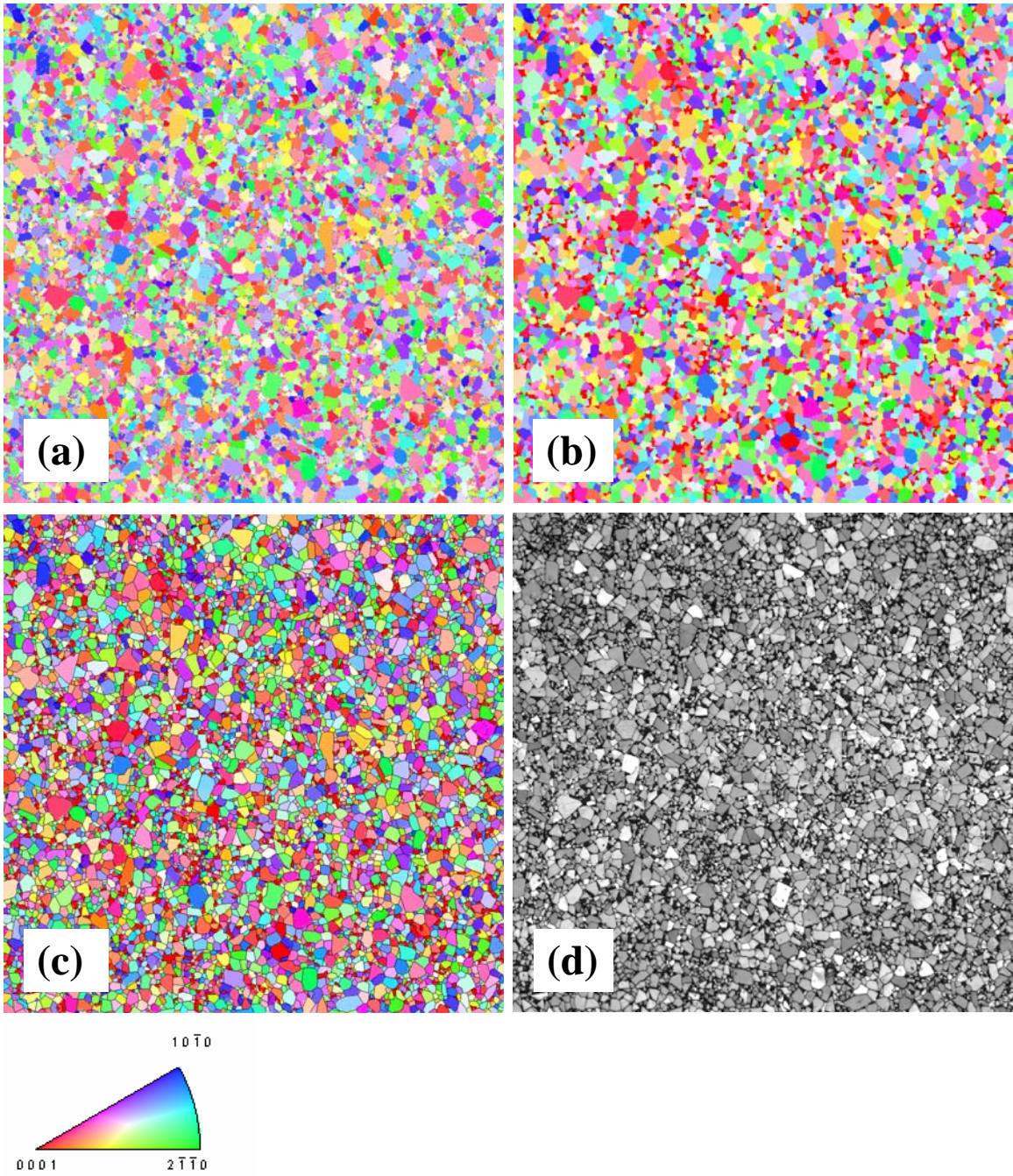


Fig. 4.6 : Example of automatic extraction of line segments (from grade A). (a) original IPF map, (b) cleaned-up IPF map, (c) cleaned-up IPF map with extracted line segments, (d) IQ (image quality) map.

4.3 WC/Co interfaces

The habit planes of the WC/Co interfaces are formed by the interaction between the liquid phase (Co) and the solid phase (WC) during the coarsening process. Here, the results from the manual tracings are described in detail, followed by a discussion of the results from the automatic extractions. Note that only the two-parameter calculation is relevant for the analysis of WC/Co interfaces.

4.3.1 Analysis of grade *E*

i) Result from the manual tracings

In this section, the WC/Co interface distribution, $\lambda(\mathbf{n})$, of grade *E* (grain diameter 1.40 μm , and carbide volume fraction 0.6919, the low carbide volume fraction grade) that results from the analysis of line segments obtained by manual tracing will be described. The stereographic projections in Fig. 4.7 show plots of WC/Co interface distribution, $\lambda(\mathbf{n})$, determined from (a) 50 observed crystals (~160 line segments) and (b) 200 observed crystals (~670 line segments) of grade *E* with an approximate resolution of 10° . As mentioned earlier, this is the probability that a length of line on the perimeter of an observed section of a WC crystal plane was created by a plane with a specific orientation: the results are presented in multiples of a random distribution (MRD). In both cases, the peaks at the $\{0001\}$ and $\{10\bar{1}0\}$ positions demonstrate that the basal and prism planes dominate the WC crystal habit. To determine what fraction of the observations belong to each habit plane, we computed the angle (α) between each line segment (in the crystal

reference frame) and the normals to $\{0001\}$ and $\{10\bar{1}0\}$. For $|\alpha-90^\circ| \leq 5^\circ$ (5° tolerance), 80% of all the observed line segments belong to one of the two habit planes. If the tolerance angle is increased to 10° , then the fraction of observations that can be assigned to either the $\{0001\}$ and $\{10\bar{1}0\}$ planes increases to 92%. When the 5° tolerance angle is used, which is comparable to the anticipated experimental errors, the basal-to-prism facet area ratio is 0.34. This ratio is not strongly sensitive to α ; it varies from 0.31 to 0.35 as the tolerance angle is varied from 3° to 10° .

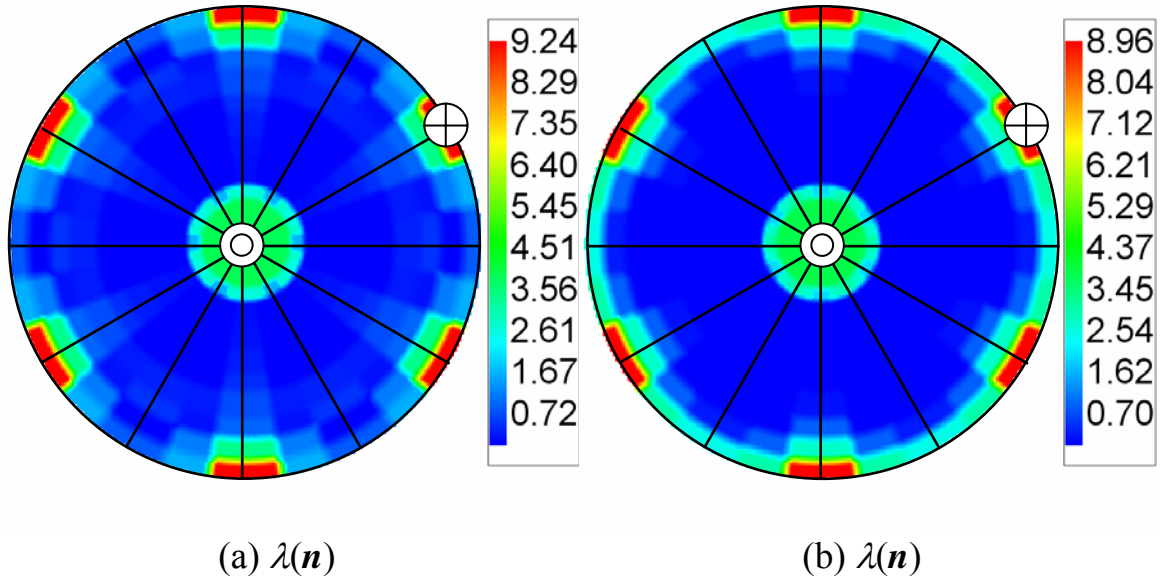


Fig. 4.7 : WC/Co Habit plane probability distribution derived from (a) 50 and (b) 200 WC crystals of grade *E*. Both are plotted in $[0001]$ stereographic projection. \odot represents a basal position and \oplus stands for a prismatic position.

The results suggest that the average three-dimensional shape of the WC crystal in Co is a hexagonal prism with six indistinguishable $\{10\bar{1}0\}$ prism facets and two $\{0001\}$ basal facets. To test this assignment, we can inspect the shape of the sections that happen

to be oriented parallel or perpendicular to the basal plane. Sections perpendicular to the basal plane should be rectangular and those sections parallel the basal plane should be hexagonal. As illustrated in Fig. 4.8, those sections perpendicular to $\{0001\}$ are rectangular, as expected. However, those parallel to the $\{0001\}$ plane are invariably triangular; hexagonal sections of WC crystals parallel to $\{0001\}$ are not observed. This indicates that the shape is a trigonal prism bound by only three of the six indistinguishable $\{10\bar{1}0\}$ planes. Considering this shape and the area ratio cited above, the trigonal prism is roughly equiaxed, with an edge length that is 1.18 times the height, as illustrated in Fig. 4.9. This shape is consistent with earlier observations reported for similar alloys [10-13]. However, it has to be noticed that the shape in Fig. 4.9 is not an equilibrium form. It is an illustration of the relative surface area of each facet and it should be regarded as an average shape or the growth form rather than equilibrium form.

The vast majority of the WC/Co boundary traces are consistent with crystal terminations along $\{10\bar{1}0\}$ and $\{0001\}$ planes and from this, we conclude that the average shape of a WC crystal in Co is an approximately equiaxed trigonal prism. Since this conclusion is consistent with earlier observations of deep etched samples [10-13], the stereological analysis is assumed to be reliable. It should be kept in mind that the result from our analysis is merely an average shape; in the composite the WC crystals are always in contact with other crystals and the shape is, therefore, truncated from the idealized form. What we can be certain of from the current results is that approximately two thirds of the WC in contact with Co has an $\{10\bar{1}0\}$ orientation and the remainder has the $\{0001\}$ orientation.

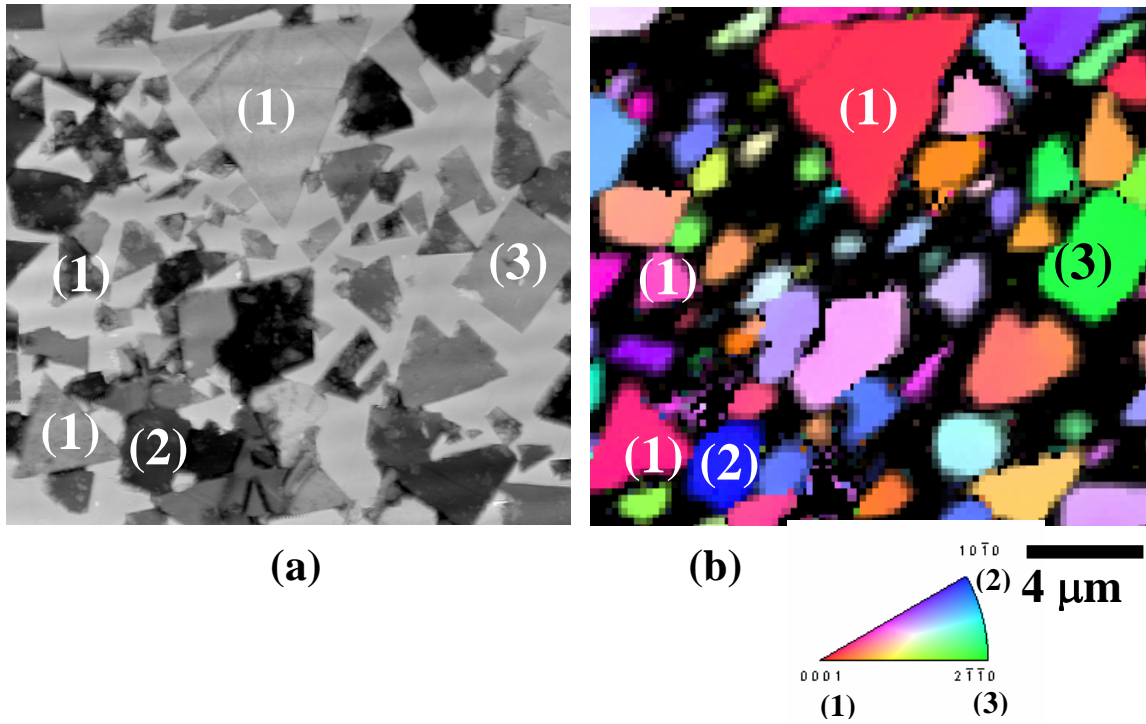


Fig. 4.8 : Comparison of WC crystal shape in (a) AFM topography image and (b) OIM inverse pole figure (IPF) map showing the crystal orientation. Both sections are from grade *E*. Triangular crystals oriented with $[0001]$ perpendicular to the paper are labeled (1).

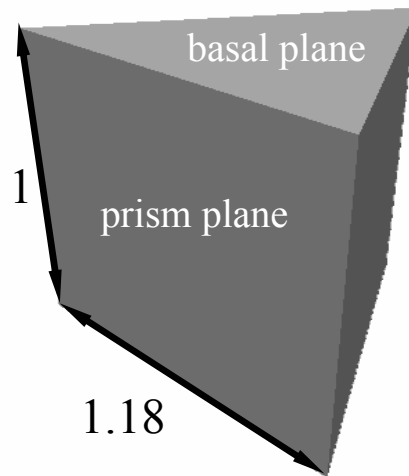


Fig. 4.9 : The proposed average shape of WC crystal in Co (data from grade *E*).

The observed trigonal symmetry of the crystal habit presumably derives from the two different terminations of the prism faces [11]. If one terminates the WC structure by breaking the fewest number of bonds, then the atoms on the six $\{10\bar{1}0\}$ faces each retain four nearest neighbors (see Fig. 4.10(a)). However, there are now two distinct sets of prism faces; three terminated by W and three terminated by C. Either set of three can form the observed triangular prism. As long as one of the two terminations is more stable than the other in contact with Co, then the observed trigonal shape is expected. Based on the current data, it is not possible to say which of the terminations is observed (see Fig. 4.10(b) and 4.10(c)).

ii) Result from the automatic extractions

In Fig. 4.11 (c), the interface plane distribution, $\lambda(\mathbf{n})$, from the automatically extracted line segments (~21000 segments) of specimen grade *E* is shown on a stereographic projection. The results are similar to those from manual tracings, but the peak heights differ; Peak positions are same (basal and prismatic positions), and the relative MRD ratios of basal to prismatic facets are approximately same. Because the manual and automatic results are comparable, the automatic method is assumed to have sufficient accuracy.

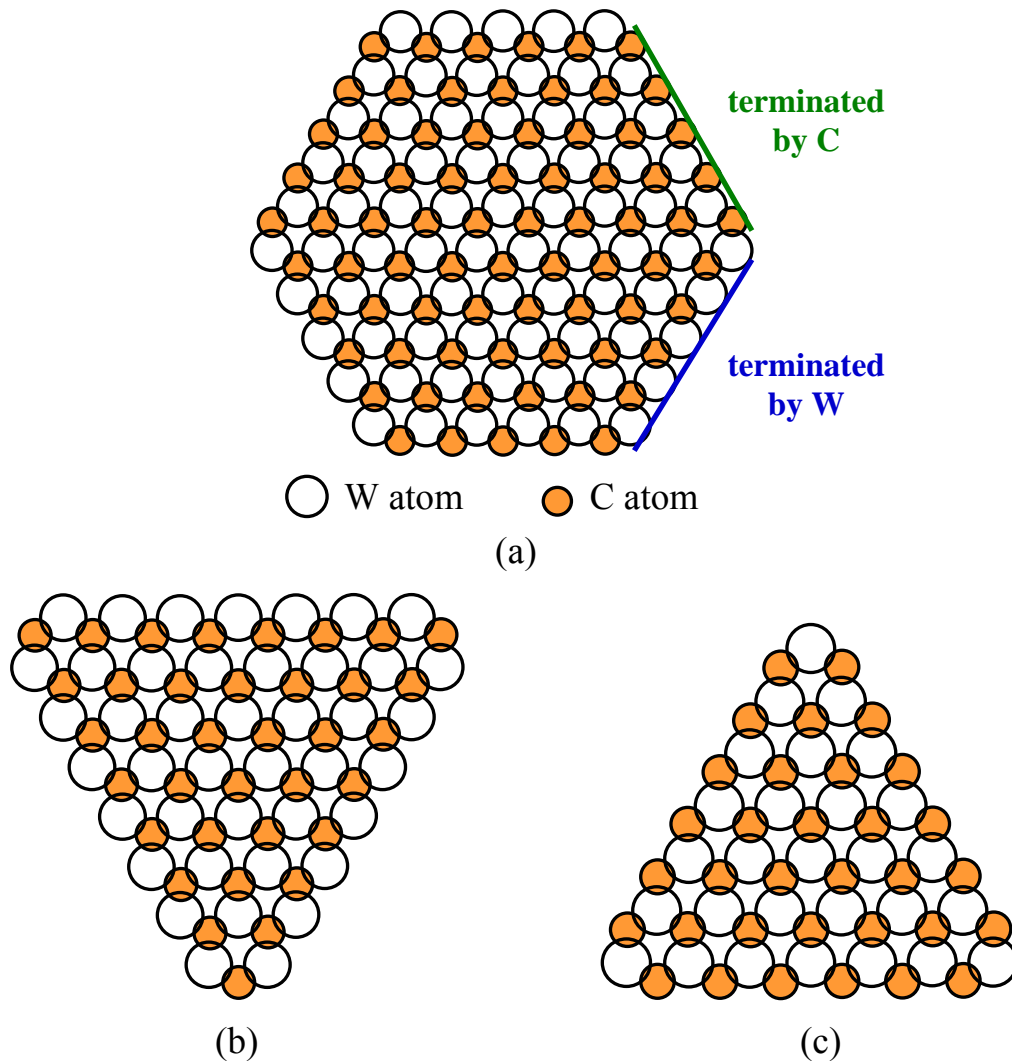


Fig. 4.10 : Atomic models for the chemical termination of WC prism planes. The smaller shaded circles represent C and the larger open circles represent W. (a) Hexagonal shape with both C and W terminated surface, and (b), (c) two possible trigonal shapes with W and C terminated surfaces, respectively.

4.3.2 Analysis of other grades

Analyses of the other specimen grades showed interface distributions dominated by basal and prism facets (see Fig. 4.11 (a)~(e)). However, they exhibit different aspect (base-to-height) ratios. Fig. 4.11 includes WC/Co interface plane distributions from selected specimen grades (automatic extractions, data from grades *B*, *D*, *E*, *H*, and *I*) with

an approximate resolution of 10° . The upper three are based on straight angular grades with different Co fractions (similar average carbide grain size). While maximum peak heights at prismatic positions are almost the same, the prismatic/basal peak ratios are different. It turned out that the aspect ratio is related to the carbide volume fraction. It is more obvious when we calculate and compare the aspect ratio using trace classification method. Fig. 4.12 shows the estimated aspect ratio as a function of the carbide volume fraction. Aspect ratios were calculated using both from the manual tracing and automatic extraction methods. If we ignore the result of grade *I* (the plate-like grade), the aspect ratio increases as the carbide volume increases. In other words, the WC crystals in composites with a high Co fraction display a more equiaxed shape. It is a general trend in calculations both from the manual tracings and automatic extractions.

The lower two results in Fig. 4.11 are from atypical specimen grades; the straight non-angular grade (grade *H*) and the alloyed grade (grade *I*). In non-angular grade (Fig. 4.11 (d)), maximum peak height at the prismatic facet is smaller than in the angular grades (Fig. 4.11 (a)~(c)). Also, there was a measurable distribution of facets that were neither prismatic nor basal. In the alloyed grade (Fig. 4.11 (e)), the peak intensity at the basal facet is stronger than that of prismatic facet, which indicates that the relative area of the basal plane is greater than the prismatic plane.

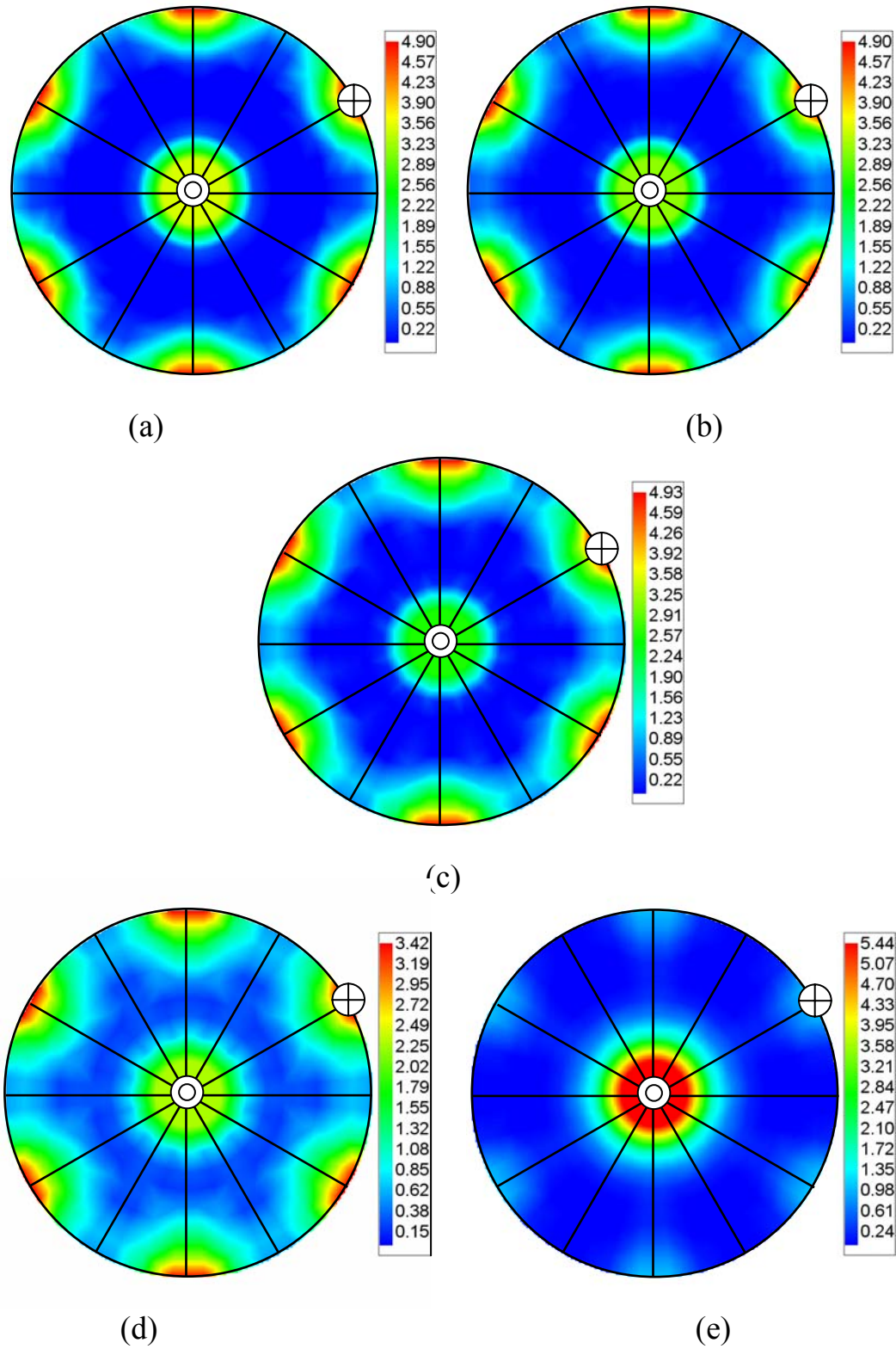


Fig. 4.11 : WC/Co interface plane distributions, $\lambda(\mathbf{n})$, from automatic extractions. (a) grade *B*, (b) grade *D*, (c), grade *E*, (d) grade *H* (the non-angular grade), and (e) grade *I* (the plate-like grade). \odot represents basal position and \oplus stands prismatic positions.

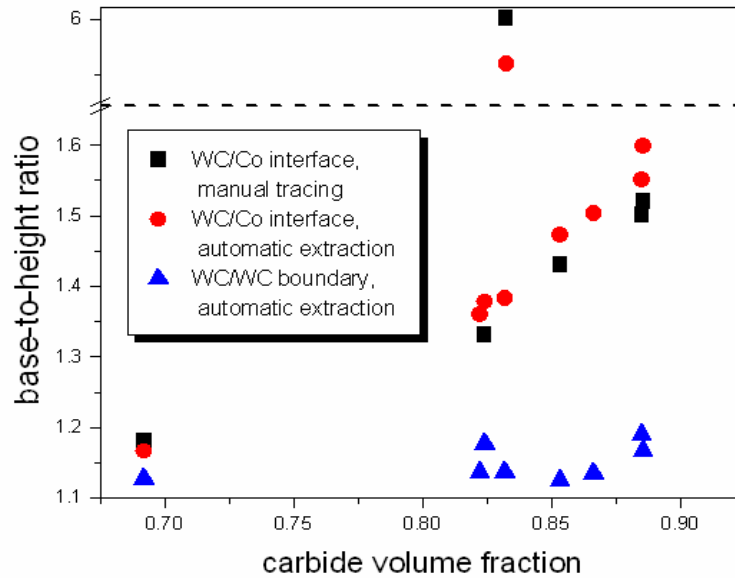


Fig. 4.12 : Variation of aspect ratio with the carbide volume fraction.

4.4 WC/WC boundaries

Recall that for a WC/WC boundary plane distribution analysis, we can either ignore the misorientations ($\lambda(\mathbf{n})$, the two-parameter calculation) or include the misorientations ($\lambda(\Delta g, \mathbf{n})$, the five-parameter calculation). This work is focused on the two-parameter calculation, and the five-parameter calculation results are briefly discussed in the last section (Section 4.4.3).

4.4.1 Analysis of grade A (two-parameter calculation)

In this section, results from misorientation averaged WC/WC grain boundary distributions, $\lambda(\mathbf{n})$, will be discussed for specimen grade A (grain diameter 5.31 μm , and carbide volume fraction 0.8852, the high carbide volume fraction grade). The results

presented here are based on observations of ~8400 WC grains and ~15600 WC/WC boundaries in a planar section of specimen grade A.

Based on an examination of (0001) pole figure of grade A, we conclude that the WC crystals exhibit no orientation texture (see Fig. 4.13). There is, however, a strong misorientation texture. The misorientation across all of observed WC/WC boundaries (~15,600) has been determined and Fig. 4.14 illustrates the relative frequency of occurrence of boundaries with different misorientation angles. For comparison, the distribution expected for randomly misoriented hexagonal crystals is also shown [14]. Note that the experimental distribution shows two peaks, at ~30° and 90°, which are not consistent with the random distribution. To examine the distribution of misorientation axes, the data are plotted in axis-angle space, as illustrated in Fig. 4.15. Note that at 30°, there is a peak at the position of the [0001] rotation axis and at 90°, there is another peak at the position of the $[10\bar{1}0]$ axis, indicating that boundaries with these two misorientations occur with a much higher than random frequency.

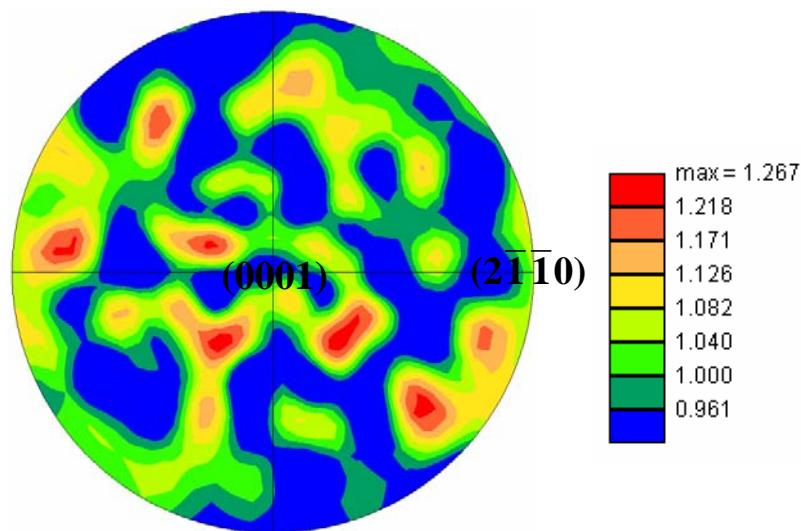


Fig. 4.13 : Pole figure of WC crystals (based on ~8400 grains of grade A). No orientation textures found.

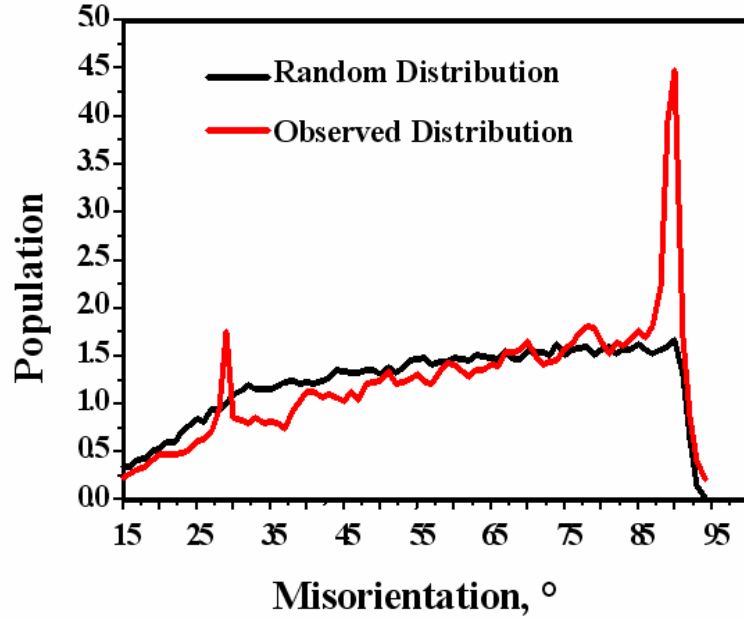


Fig. 4.14 : Grain boundary population of WC crystals (grade A) and random objects as a function of misorientation angle.

We can also analyze the habit planes of the boundaries that have a 30° rotation around the $[0001]$ axis and those that have a 90° rotation about the $[10\bar{1}0]$ axis. Here, we consider the bounding plane of each crystal independently. In other words, in the analysis of the line segments, we are applying the complete hexagonal symmetry of each crystal. The habit plane distribution for the crystals comprising boundaries with 90° rotations about the $\langle 10\bar{1}0 \rangle$ axis, $\lambda(\Delta g, \mathbf{n}) = \lambda(90^\circ / \langle 10\bar{1}0 \rangle, \mathbf{n})$, are depicted in Fig. 4.16(a). Here the misorientation, Δg , is specified by an angle/axis notation, $90^\circ / [10\bar{1}0]$. It is clear that the habit of this boundary is on the $\{10\bar{1}0\}$ plane, which is perpendicular to the common rotation axis, $[10\bar{1}0]$. As long as the interface plane is perpendicular to the bicrystal's common rotation axis, then the bounding plane is the same in both crystals and it is a pure twist configuration. If there was a tilt component, the boundary could not be

constructed from only $\{10\bar{1}0\}$ planes. The bicrystal formed by a 90° $[10\bar{1}0]$ twist is illustrated schematically in Fig. 4.17(a).

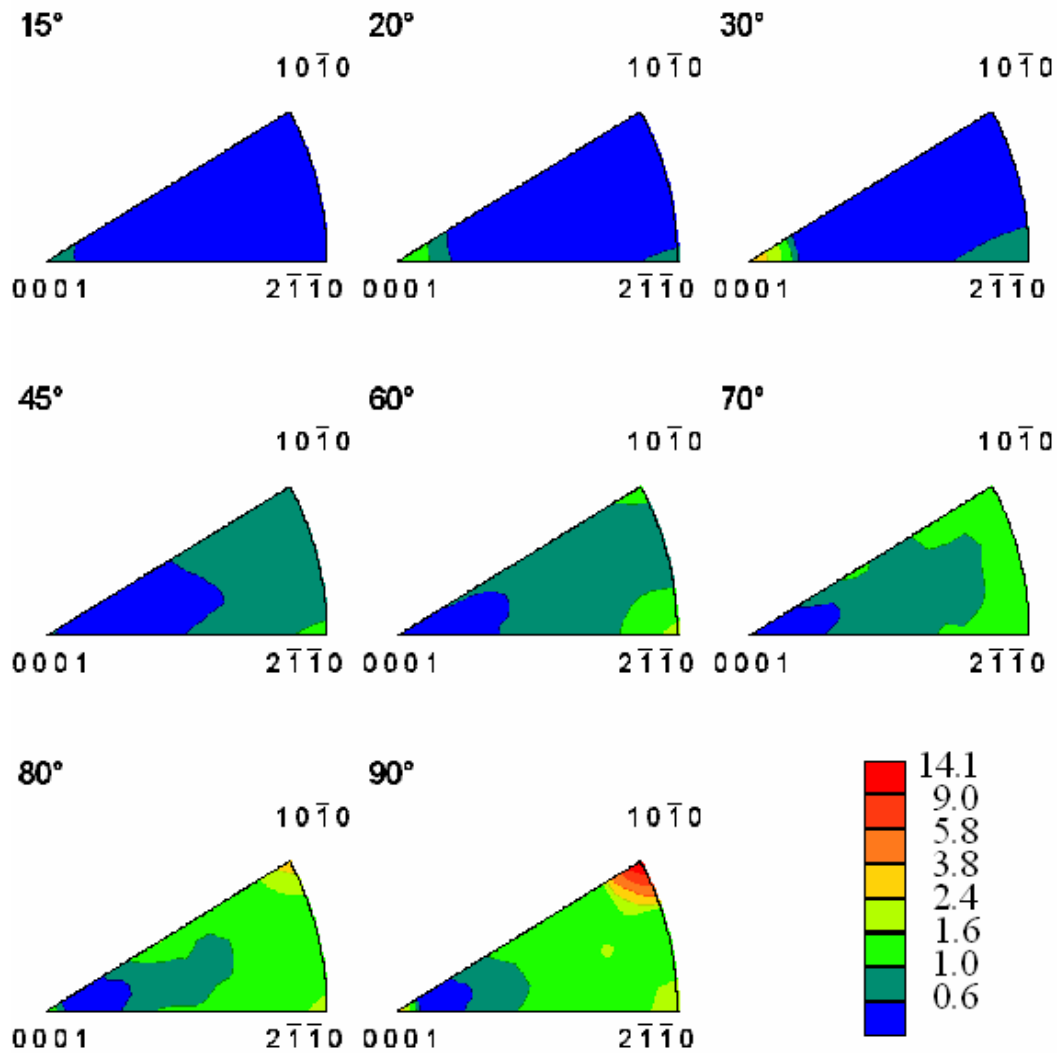
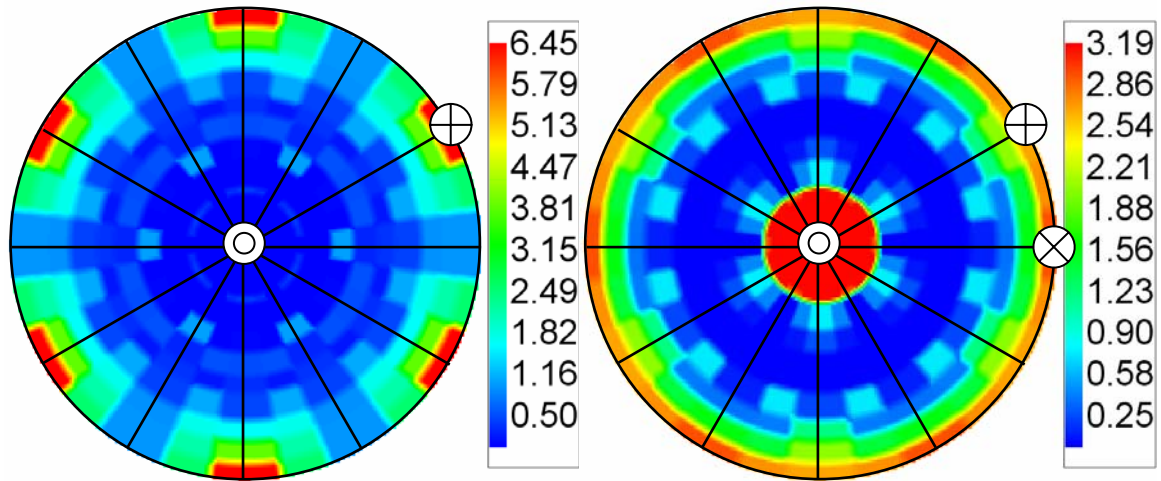


Fig. 4.15 : WC/WC grain boundary misorientation distribution (grade A) in axis-angle space. Sections of fundamental zone are taken perpendicular to the $[0001]$ axis.

The boundaries with 30° rotations around the $\langle 0001 \rangle$ axis, $\lambda(\Delta g, \mathbf{n}) = \lambda(30^\circ / \langle 0001 \rangle, \mathbf{n})$, on the other hand, exhibit multiple habit planes, as illustrated in Fig. 4.16(b). The peak at the basal position confirms the presence of twist boundaries. As

mentioned above, as long as the interface plane is perpendicular to the common axis, it is a twist boundary. This configuration is illustrated in Fig. 4.17(b). The remaining habit planes are $\{10\bar{1}0\}$ and $\{11\bar{2}0\}$. The normals to these planes are perpendicular to the $[0001]$ misorientation axis and separated by 30° (the misorientation angle). Therefore, they are complementary planes that comprise the same 30° tilt boundary. In other words, when one crystal is terminated by a $\{10\bar{1}0\}$ plane, the geometrically required complement (parallel plane) in the crystal rotated by 30° around $[0001]$ is $\{11\bar{2}0\}$. Therefore, both of the two habit planes perpendicular to the $[0001]$ axis can be accounted for by the same asymmetric tilt bicrystal, illustrated in Fig. 4.17(c).



(a) $\lambda(\Delta g, \mathbf{n}) = \lambda(90^\circ / \langle 10\bar{1}0 \rangle, \mathbf{n})$

(b) $\lambda(\Delta g, \mathbf{n}) = \lambda(30^\circ / \langle 0001 \rangle, \mathbf{n})$

Fig. 4.16 : Habit plane probability distribution for (a) 90° boundaries and (b) 30° boundaries of grade A. Both are plotted in the $[0001]$ stereographic projection. \odot , \oplus , and \otimes represent (0001) , $(10\bar{1}0)$, and $(11\bar{2}0)$ poles, respectively.

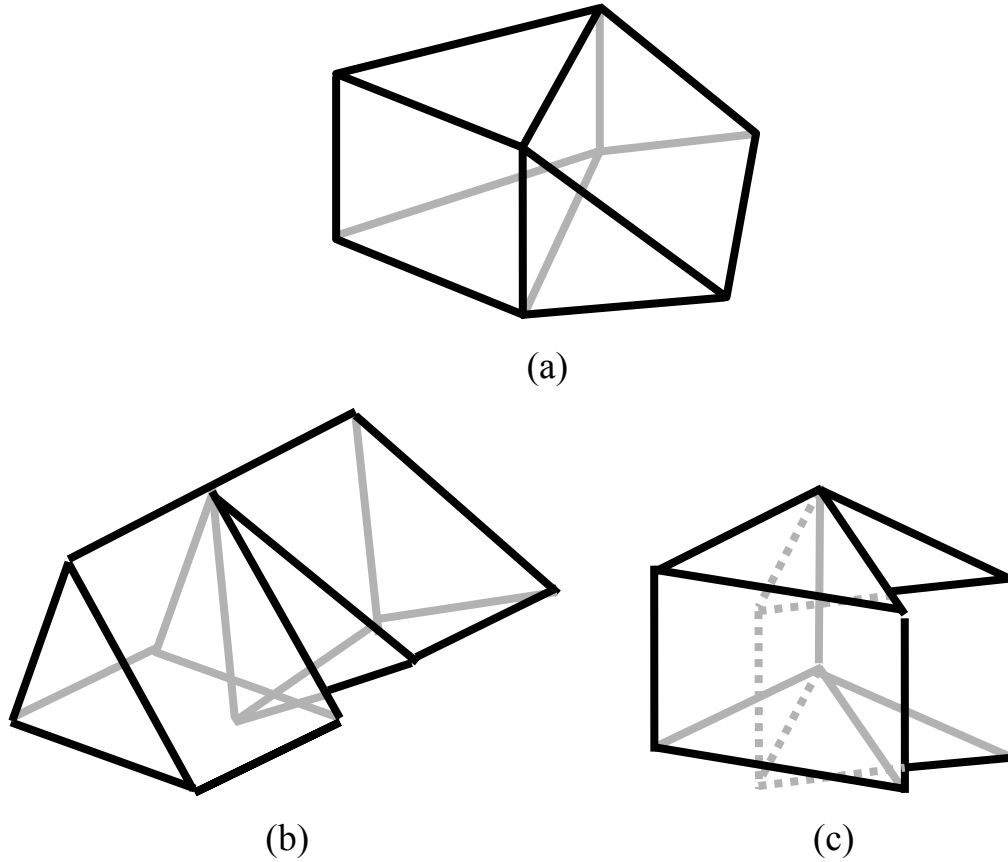


Fig. 4.17 : Schematic representations of the three most common types of grain boundaries in composites. (a) $90^\circ [10\bar{1}0]$ boundary with two $\{10\bar{1}0\}$ planes, (b) $30^\circ [0001]$ boundary with two $\{0001\}$ planes, and (c) $30^\circ [0001]$ boundary with $\{10\bar{1}0\}$ and $\{11\bar{2}0\}$ planes.

Using a tolerance of 3° on the axis and angle parameters and a tolerance of 5° on the boundary plane parameters, we find that 11% of all the observed boundaries have the $90^\circ [10\bar{1}0]$ twist configuration and 3% have one of the two $30^\circ [0001]$ configurations. One can imagine several possible mechanisms for the formation of the WC/WC grain boundaries. They might be left over from the starting materials or they might form when two grains impinge as the result of either coarsening or grain growth. Neither process suggests a mechanism for creating higher populations of certain boundary types. A more likely explanation is that a random distribution of boundaries is created by growth related

impingement and that the highest energy boundaries are then eliminated from the population by the infiltration of Co. This process, which is consistent with the observed random orientation texture of the samples, would lead to an enhanced population of boundaries that are resistant to wetting [15]. The boundaries that are preserved in the population must have energies that are less than twice the WC/Co interface energy.

Based on the special geometric characteristics of the three boundaries that dominate the population, it seems feasible that they represent relatively low energy configurations and resist wetting. The most populous boundary is the $90^\circ [10\bar{1}0]$ twist boundary. The WC unit cell has a c/a ratio of 0.976 so that a 90° rotation about $[10\bar{1}0]$ that brings $[0001]$ axis in one crystal parallel to $[2\bar{1}\bar{1}0]$ in the other and the misfit between the two rectangular surface units is less than 3%. The stability of this boundary against wetting has been demonstrated in a TEM study, which showed a direct WC to WC transition at this boundary [16]. The $30^\circ [0001]$ twist configuration is close to a relatively high coincidence boundary ($\Sigma 13$, $28^\circ [0001]$, in which one out of 13 lattice sites are in coincidence). If we assume that the high coincidence also leads to a low energy, then this can potentially explain its stability against wetting. However, the $30^\circ [0001]$ asymmetric tilt, while it forms the same coincident site lattice, does not have an interface plane of high coincidence. Farooq and Klement used orientation imaging microscopy to measure the distribution of WC/WC grain boundary. In contrast to our results, they reported that the distribution is nearly random and that there are no significant amounts of special boundaries [20]. However, it is considered that the WC/WC grain boundaries that were used in their analysis are distorted by the OIM clean-up procedure.

A second geometric principal that can be used to assess the relative energies of grain boundaries is that interfaces made up of planes with large interplanar spacings generally have lower energies [17]. The basic idea is that planes with large interplanar spacing are also relatively flatter, and two smooth surfaces fit together better than two rough surfaces. The superior fit results in greater attractive forces across the boundary and less repulsion, which means that the boundary has a relatively lower energy. For the case of WC, the $\{10\bar{1}0\}$ and $\{0001\}$ interface planes have the two greatest interplanar spacings, 2.52 Å and 2.84 Å, respectively. The $\{11\bar{2}0\}$ plane, which is a component of the $[0001]$ asymmetric tilt boundary, has the fourth largest interplanar spacing, 1.45 Å. Therefore, if we assess the energies of the boundaries according to the interplanar spacings of their component planes, we also conclude that the three most common boundaries have relatively low energies.

Another potential explanation for the occurrence of a high population of boundaries with $\{10\bar{1}0\}$ and $\{0001\}$ interface planes is that the crystals are already terminated by these orientations in the liquid Co and, if forced together, would be expected to align with their habit planes parallel. This process would clearly favor the occurrence of $[10\bar{1}0]$ and $[0001]$ twist boundaries. However, since these twist boundaries are observed preferentially at characteristic angles (90° and 30°), the crystals would also have to rotate into these particular configurations. Considering the constraints imposed by the other crystals in the composite, this does not seem very likely. Therefore, an enhanced stability against wetting seems to be a more likely explanation for the high population of these boundaries.

4.4.2 Analysis of other grades (two-parameter calculations)

The WC/WC boundary segments data for other specimen grades were extracted from the OIM images from the TSL software. The stereological method has been applied with an approximate resolution of 10° . $2 \times 10^4 \sim 4 \times 10^4$ WC/WC boundary line segments, depending on the specimen grade, were used in the calculations. More line segments were obtained from the grades with higher carbide volume fractions. Examinations of WC/WC grain boundary plane distributions (misorientation averaged distribution, not shown) again revealed two prominent peaks at prismatic and basal positions for all grades. Furthermore, the peak heights and the ratios of two dominant facets in all angular straight grades are almost indistinguishable. All of the calculated aspect ratio (base-to-height ratio) falls in the range of 1.12 to 1.19 (see Fig. 4.12).

To quantify the populations of two WC/WC grain boundaries ($90^\circ [10\bar{1}0]$ twist and $30^\circ [0001]$), we used the same tolerance angles (3° on the axis and angle parameters and 5° tolerance on the boundary plane parameters) as for the straight angular grades (grades *A~G*). The population of these two boundaries in all straight angular grades appears to be nearly constant, occupying 11 to 14 % and 2 to 3 % for 90° and 30° configurations, respectively; recall that the respective populations for the specimen grade *A* are 11 and 3 %. The populations, on the other hand, for specimen grade *H* (straight non-angular grade) and *I* (alloyed plate-like grade) were found to be different from the straight angular grades. As expected, the non-angular grade (grade *H*) displays low populations for the two special boundaries; 7 % for 90° boundaries and 1% for 30° boundaries. In case of the plate-like grade (grade *I*), 30° boundaries exceed 90° boundaries in population, since the basal facet is more frequent than the prismatic one;

90° and 30° boundaries make up 6 % and 7 % of the populations, respectively. The occurrences of basal and prismatic facets in WC/WC boundaries are less frequent than for WC/Co interfaces. With a 5° tolerance angle, the percentage of the two special facets (basal and prismatic) decreases from ~80 % of the WC/Co interfaces to ~60 % of the WC/WC grain boundaries. The peak height at the two positions reflects this fact. Fig. 4.17 (a) and (b) compares the plane distributions between WC/Co interfaces (Fig. 4.18 (a), same as Fig. 4.11 (a)) and WC/WC boundaries (Fig. 4.18 (b)) in the specimen grade *B*. The respective peak heights of the distribution at prismatic orientations of WC/Co interfaces (MRD=4.93) are higher than for WC/WC boundaries (MRD=4.02). The reduced area of special orientations for the internal interfaces is probably the result of impingement that occurs during coarsening. The same phenomena was found in all specimen grades (grades *A~H*).

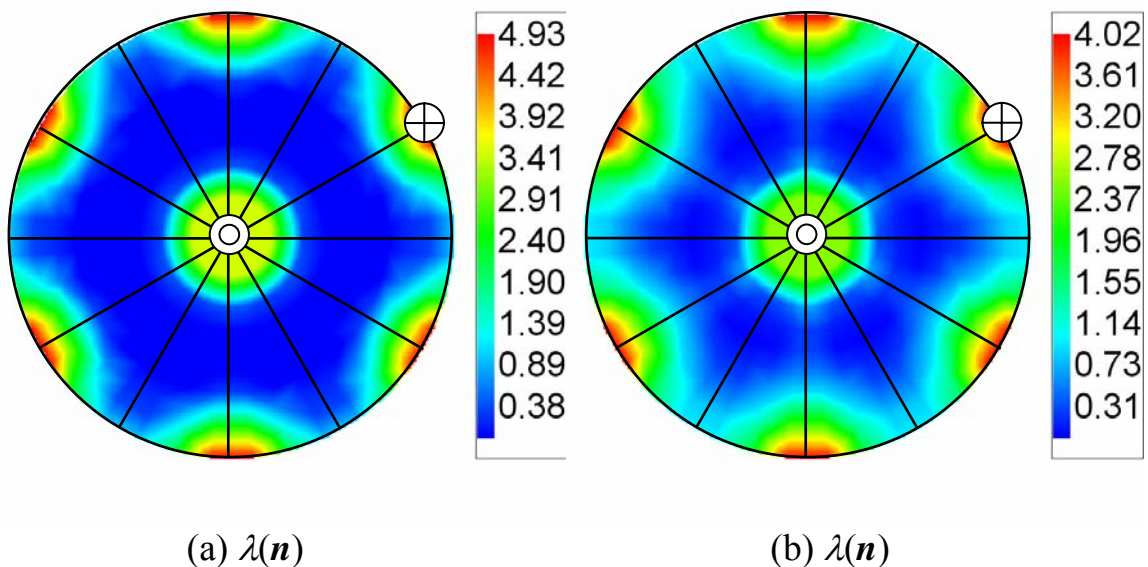


Fig. 4.18 : Habit plane distributions of grad *B* from automatic extractions. (a) WC/Co interfaces, and (b) WC/WC grain boundaries. \odot represents a basal position and \oplus stands for a prismatic position.

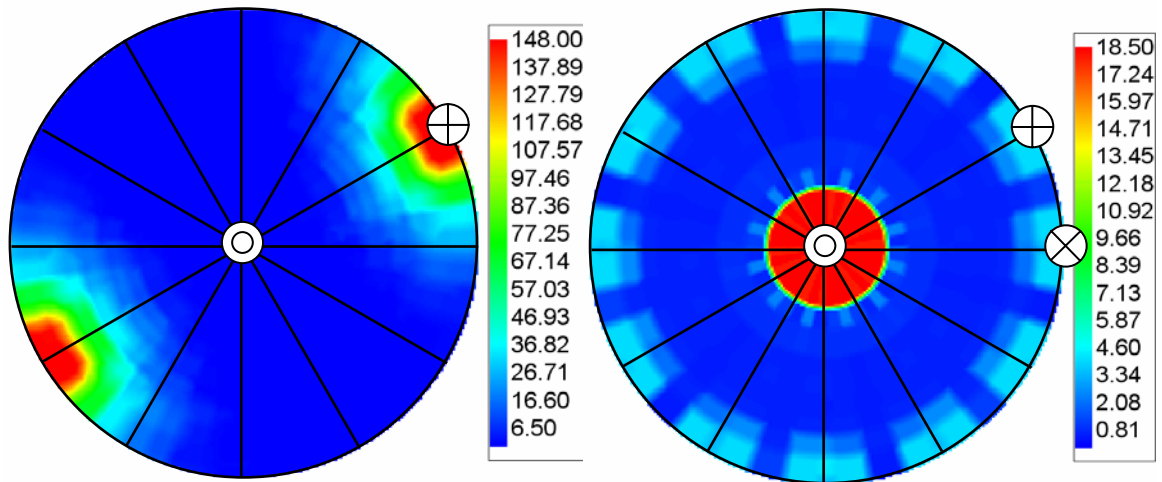
4.4.3 Five-parameter calculation

Up to now, misorientation averaged results (two-parameter calculation) for WC/Co interfaces and WC/WC boundaries were discussed. To include misorientations in the WC/WC grain boundary plane distribution analysis, it is necessary to have at least 2.6×10^4 line segments (see estimates in Section 4.2.1). Since the populations of the two special boundaries in each straight angular specimen grade are almost invariant (11 to 14 % and 2 to 3 % for $90^\circ \{10\bar{1}0\}$ and $30^\circ \{0001\}$ boundaries, respectively), we have combined all of the data from all of the straight angular grades. The total number of line segments accrued was $\sim 2.2 \times 10^4$, which is approximately 85 % of the required number. While some of the misorientations will not have enough data for a reliable analysis, data from the highly populated misorientations should be sufficient for the five-parameter analysis.

Fig. 4.19 (a)~(c) illustrate the grain boundary plane distributions, $\lambda(\Delta g, \mathbf{n})$, for misorientations of 90° about the $[10\bar{1}0]$ axis, 30° about the $[0001]$ axis, and 90° about the $[\bar{2}110]$ axis. A strong peak at the $(10\bar{1}0)$ position in Fig. 4.19 (a) confirms the 90° twist configuration and peaks at the $\{10\bar{1}0\}$, $\{11\bar{2}0\}$ and (0001) positions in Fig. 4.19 (b) demonstrate the 30° twist and 30° asymmetric configurations. It appears that the 30° twist boundary is more populous than the 30° asymmetric boundaries in general straight angular grades; the MRD value at the (0001) orientation is 18.2 and the MRD value at the $\{10\bar{1}0\}$ and $\{11\bar{2}0\}$ orientations is approximately four. Note that the grain boundary distribution ($\lambda(\Delta g, \mathbf{n}) = \lambda(90^\circ [10\bar{1}0], \mathbf{n})$, five-parameter calculation) in Fig. 4.19(a) is

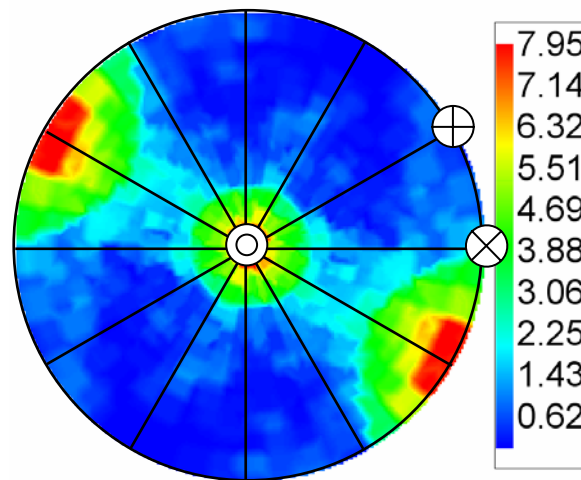
different from the distribution ($\lambda(\Delta g, \mathbf{n}) = \lambda(90^\circ < 10\bar{1}0 >, \mathbf{n})$, two-parameter calculation, all of the 90° boundaries were used) in Fig. 4.16 (a). After spanning all misorientation space, we found another set of boundaries other than these two special misorientation-boundary pairs that have relatively high populations at 90° about $[\bar{2}110]$ (see Fig. 4.19 (c)). The peaks at the basal and prismatic orientations (which are separated by 90°) indicate the presence of an asymmetric tilt boundary.

The fact that there is a strong preference for low index planes in WC/WC grain boundaries is consistent with observations in other polycrystalline materials [3, 4, 6]. Even if there is a thin layer of Co between the carbide grains as some has argued [18, 19] (dispersed carbide hypothesis, see Section 2.2.2), it apparently does not greatly affect the tendency for specific low index interface planes to align with one another. The carbide skeletons are connected mostly by the 90° and 30° misorientations and these boundaries are thought to be low energy configurations.



(a) $\lambda(\Delta g, \mathbf{n}) = \lambda(90^\circ / [10\bar{1}0], \mathbf{n})$

(b) $\lambda(\Delta g, \mathbf{n}) = \lambda(90^\circ / [0001], \mathbf{n})$



(c) $\lambda(\Delta g, \mathbf{n}) = \lambda(90^\circ / [\bar{2}110], \mathbf{n})$

Fig. 4.19 : Grain boundary plane distributions. (a) 90° misorientation about $[10\bar{1}0]$ axis, (b) 30° misorientation about $[0001]$ axis, and (c) 90° misorientation about $[\bar{2}110]$ axis. \odot , \oplus , and \otimes represent (0001) , $(10\bar{1}0)$, and $(11\bar{2}0)$ poles, respectively.

4.5 Summary

A stereological method has been used to analyze the distribution of WC/Co and WC/WC interfaces in WC-Co composites. For WC/Co interfaces, it was found that $\{10\bar{1}0\}$ prismatic and $\{0001\}$ basal facets dominate the populations. These two special facets make up ~80 % of the WC/Co interfaces. The aspect ratio (base-to-height ratio of prismatic plane) increases as the carbide volume fraction increases. For WC/WC boundaries, the prismatic and basal facets were also prominent. The basal and prismatic planes make up ~60 % of the entire grain boundary population. Grain boundaries with a 90° about $[10\bar{1}0]$ make up 11~14 % of the population and boundaries with 30° about $[0001]$ make up 2~3 % of the population in straight angular grades (grades A~G), respectively.

4.6 References

- [1] D.M. Saylor and G.S. Rohrer, "Determining Crystal Habits from Observations of Planar Sections", *J. Am. Ceram. Soc.*, **85**, 2799 (2002)
- [2] C.-S. Kim and G.S. Rohrer, "Geometric and Crystallographic Characterization of WC Surfaces and Grain Boundaries in WC-Co Composites", *Interface Sci.*, **12**, 19 (2004)
- [3] D.M. Saylor, B.S. El-Dasher, Y. Pang, H.M. Miller, P. Wynblatt, A.D. Rollett, and G.S. Rohrer, "Habits of Grains in Dense Polycrystalline Solids", *J. Am. Ceram. Soc.*, **87**, 724 (2004)

- [4] T. Sano, C.-S. Kim, and G.S. Rohrer, "Shape Evolution of SrTiO₃ Crystals During Coarsening in a Titania-Rich Liquid", *J. Am. Ceram. Soc.*, in press
- [5] D.M. Saylor, B.L. Adams, and G.S. Rohrer, "Measuring the Five Parameter Grain Boundary Distribution From Observations of Planar Sections", *Metall. Mat. Trans.*, **35A**, 1981 (2004)
- [6] D.M. Saylor, B.S. El Dasher, A.D. Rollett, and G.S. Rohrer, "Distribution of Grain Boundaries in Aluminum as a Function of Five Macroscopic Parameters", *Acta Mater.*, **52**, 3649 (2004)
- [7] D.M. Saylor, B.S. El-Dasher, T. Sano, and G.S. Rohrer, "Distribution of Grain boundaries in SrTiO₃ as a Function of Five Macroscopic Parameters", *J. Am. Ceram. Soc.*, **87**, 670 (2004)
- [8] M.G. Kendall and P.A.P. Moran, Geometrical Probability, Hafner Publishing Company, New York, 1963
- [9] S.I. Wright and R.J. Larsen, "Extracting Twins from Orientation Imaging Microscopy Scan Data", *J. Microscopy*, **205**, part 3, 245 (2002)
- [10] D.N. French, "The Microstructure and Microproperties of WC-Co Alloys", *Int. J. Powder Metall.*, **5**, No. 3, 47 (1969)
- [11] J. Gurland, "New Scientific Approaches to Development of Tool Materials", *Int. Mater. Rev.*, **33**, No. 3, 151 (1988)
- [12] A.V. Shatov, S.A. Firstov, nad I.V. Shatova, "The Shape of WC Crystals in Cemented Carbides", *Mater. Sci. Eng. A*, **242**, 7 (1998)

- [13] S. Kim, S.-H. Han, J.-K. Park, and H.-E. Kim, "Variation of WC Grain Shape with Carbon Content in the WC-Co Alloys during Liquid-phase Sintering", *Scripta Mater.*, **48**, 635 (2003)
- [14] A. Morawiec, "Misorientation-angle Distribution of Randomly Oriented Symmetrical Objects", *J. Appl. Cryst.*, **28**, 289 (1995)
- [15] P. Wynblatt, M. Takashima, "Correlation of Grain Boundary Character with Wetting Behavior", *Interface Science*, **9**, 265 (2001)
- [16] S. Hagege, G. Nouet, and P. Delavignette, "Grain Boundary Analysis in TEM (IV)", *Phys. Stat. Sol. A*, **61**, 97 (1980)
- [17] D. Wolf, "Correlation between Structure, Energy, and Ideal Cleavage Fracture for Symmetrical Grain Boundaries in FCC Metals", *J. Mater. Res.*, **5**, 1708 (1990)
- [18] J. Gurland and J.T. Norton, "Role of the Binder Phase in the Cemented Carbide-Cobalt Alloys", *Trans. Metall. Soc. AIME*, **194**, 1051 (1952)
- [19] A. Henjered, M. Hellsing, H.-O. Andren, and H. Norden, "Quantitative Microanalysis of Carbide/carbide Interfaces in WC-Co-base Cemented Carbides", *Mater. Sci. Technol.*, **2**, 847 (1986)
- [20] M.U. Farooq and U. Klement, "EBSD characterization of carbide-carbide boundaries in WC-Co composites", *J. Microscopy*, **213**, 306 (2004)

Chapter 5

Finite Element Simulations of Fracture Strength in WC-Co Composites

This chapter describes a finite element method (FEM) for predicting the mechanical properties of WC-Co composites. A brittle fracture criterion has been assumed to estimate the fracture strength of these materials. Both the digital grain maps constructed on the basis of direct microstructural measurements (AFM maps, such as those in Fig. 3.3(c) and OIM maps, such as those in Fig. 3.2 (b)) have been used as input. In the first section, the simulation method using the object-oriented finite (OOF) element code will be explained. The results of yield strength (YS) and transverse rupture strength (TRS) calculations using real microstructures are presented in section two. By comparing the results of calculations with measurements, we are able to select a fracture energy that allows the simulation to reproduce the observed transverse rupture strength. The calibrated simulation can then be used to calculate the properties of hypothetical microstructures; this is discussed in section three.

5.1 Simulation methods

Object-oriented finite element analysis (OOF) was developed at National Institute of Standards and Technology (NIST, Gaithersburg, MD). As described in Chapter 2, this

program is designed to investigate the stress, strain and failure behavior in complex microstructures. The program performs two-dimensional thermo-elastic computations under mechanical and/or thermal loads. In this work, the responses to the combined loads (mechanical + thermal) were calculated for the real WC-Co microstructures. For the some of hypothetical microstructures, only mechanical loads were applied to estimate the fracture strength. It has been found that while this simplified approach using only mechanical loads leads to quantitatively different answers, the trend is unchanged and it is only these relative changes that are of interest in the hypothetical microstructures.

Digital grain maps from orientation imaging microscopy (OIM) and atomic force microscopy (AFM) that were used for the previously described microstructural analysis procedures were used as input. Crystallographic orientations and elastic constants of each phase (carbide and binder) were incorporated to model the anisotropic materials properties. The crystallographic orientations of the WC crystals were obtained by electron backscattered patterns (EBSPs), in the form of Euler angles (ϕ_1 , Φ , ϕ_2). Table 5.1 [1, 2] presents the elastic constants of the WC and Co phases. Since the crystallographic orientations of the Co phase were not measured, the bulk properties (Young's modulus, E_{Co} , and Poisson's ratio, ν_{Co}) have been used instead of the anisotropic stiffness (C_{11} , C_{22} , C_{33} , C_{12} , C_{13} , and C_{23}) of Co. In other words, the carbide phase was modeled as a hexagonal material, while the binder phase was treated as an isotropic material. It turns out, however, that the isotropic assumption for Co does not affect the results significantly. Tests using random assignments of Co orientations and actual stiffnesses yielded the same results as tests using isotropic elastic constants. The consistency of the results from

the two elastic models presumably derives from the high concentrations of residual stresses at sharp edges of the binder phase.

	WC	Co
C_{11} [GPa]	720	307
C_{33} [GPa]	972	358.1
C_{44} [GPa]	328	78.3
C_{12} [GPa]	254	165
C_{13} [GPa]	267	103

(a)

	WC	Co
E [GPa]	714	211
ν	0.19	0.31

(b)

Table 5.1 : Elastic constants of WC and Co [1, 2]. (a) Microstructural property (hexagonal symmetry). (b) Bulk property (isotropic). E denotes Young's modulus and ν denotes Poisson's ratio.

As described in Chapter 2, the finite elements in the OOF program fail under a Griffith-like criterion [3],

$$2\gamma\Delta L \leq \frac{1}{2}\sigma_{ij}\varepsilon_{ij}A \quad (5.1)$$

in which γ is the surface energy of the cracked interface, ΔL is the edge length, A is the area, σ_{ij} is the stress, and ε_{ij} is the strain of a element, respectively. Therefore, specifications of appropriate surface energies (or fracture energies, γ) are important to simulate mechanical failures. Since there are four possible crack paths (transgranular along WC/WC boundaries, transgranular along WC/Co interfaces, intergranular in WC

crystals, and intergranular in the Co) [4], it is necessary to define different fracture energies for each case. Moreover, the transgranular fracture energies vary with the crystallographic misorientations. Currently, it is not feasible to obtain the correct fracture energy distributions as a function of crystallographic orientation and/or misorientation in WC-Co composites. In this work, therefore, we assume that cracks always initiate in the WC phase (intergranular along WC/WC grain boundaries and transgranular in WC grains), and that fracture energies (γ) for the intergranular and transgranular fracture of the carbide phase are constant [5]. This assumption is supported by the theoretical fracture energy models of Sigl and Fischmeister's [5]. They reported that the fracture energies of the WC phase are significantly lower than those of the WC/Co interface and/or Co phase.

It has been found that thermal loads are important for determining the fracture energy of the composites (see Section 5.2). However, to simplify the description of OOF simulation, an example (from grade A) is used that is subject only to a mechanical load. While the actual calculations for WC-Co composites were performed using OIM maps, in this example, a digital image from AFM has been used as an input (see Fig. 5.1). Based on the microstructural data and the direct measurement technique described earlier (see Section 3.2.3), a grain map is constructed and this was used for the OOF program. Using a sub-program called 'ppm2oof' (version 1.1.27), the corresponding finite element mesh can be generated as shown in Fig. 5.1(d). We then performed an OOF (version 1.1.17) simulation that allowed us to calculate the stress and strain at the point of fracture according to Eq. (5.1). The stress at this point (crack initiation point) is considered to be the yield strength (YS). Thus, the key to this analysis is to find the first crack initiation

point as the mechanical load is incrementally increased. Fig. 5.1(e) and Fig. 5.1(f) represent stress (stress invariant 1, $\sigma_{11}+\sigma_{22}+\sigma_{33}$) distributions at the fracture point for elongation tests. The fractured elements are colored black (surrounded by circles). All of the simulations in this thesis were carried out under the plane-stress condition. Note that the stress distributions for the x- and y- simulations are different, and that the fractured elements are also different. All of the fracture strength calculation results presented in this thesis are averages of the x- and y- simulations.

One thing that should be mentioned is that all the simulation results discussed in the later sections are based on the ‘skeletonized carbide’ hypothesis [6] (see details in Section 2.2.2). Even though it is possible that there is a very thin Co layer at the carbide/carbide boundary, the layer was ignored in all calculations. This amounts to saying that even if there is a thin layer of Co at WC/WC boundaries, it has a brittle and hard character in comparison to bulk Co. In other words, it is assumed that the ‘skeletonized carbide’ hypothesis is acceptable for the mechanical property calculations.

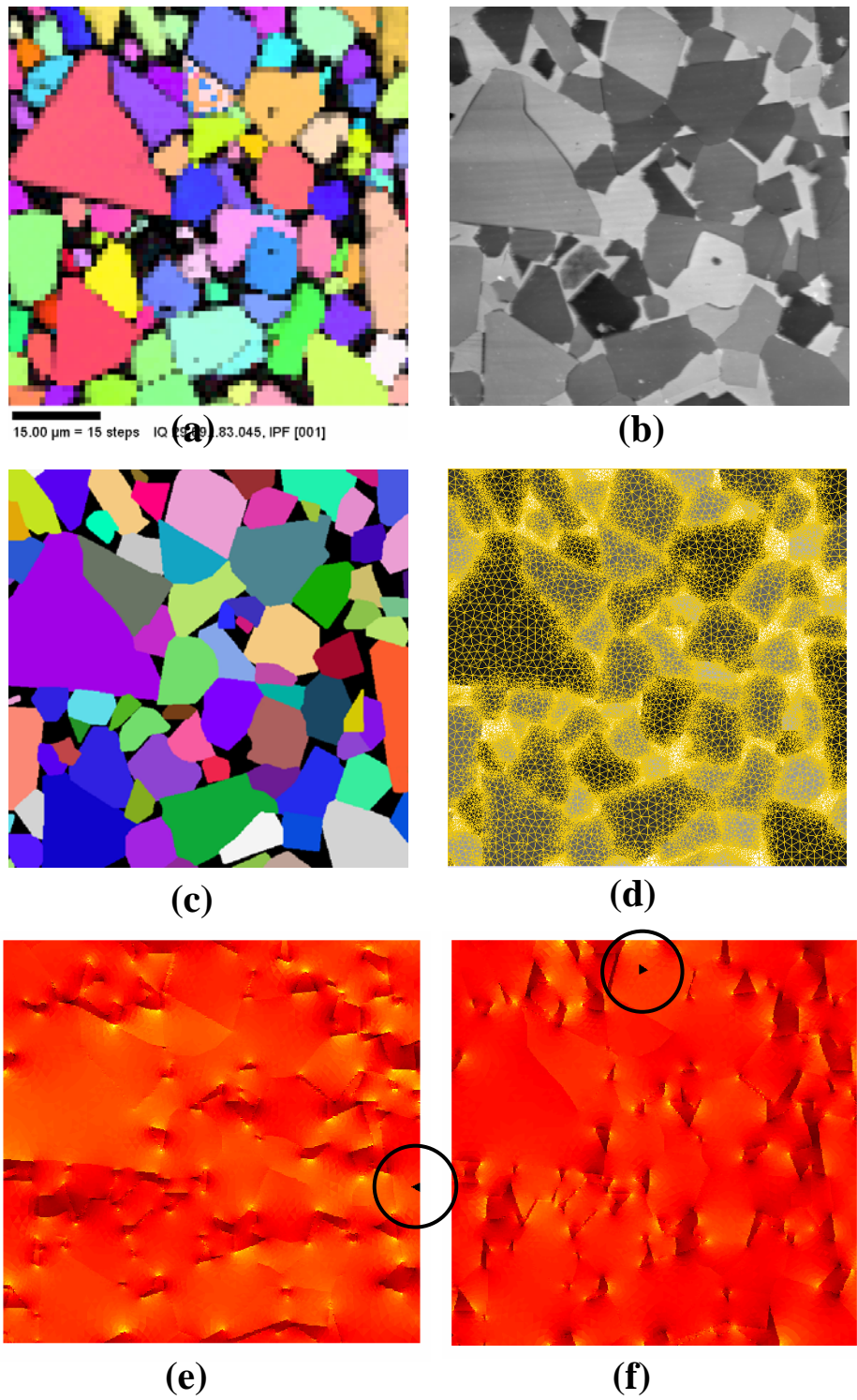


Fig. 5.1 : Example of OOF simulations under mechanical loads. (a) OIM IPF map. (b) AFM topography map. (c) Grain map. (d) Finite element mesh. (e) stress invariant 1 distribution along x-elongation. (f) stress invariant 1 distribution along y-elongation. (see text for details).

Euler angles in OOF software

The Euler angles used in the OOF code are different from the conventional definition of Bunge. OOF's Euler angle (α, β, γ) definition is as follows [3]:

- 1) Rotate β about the z-axis
- 2) Rotate α about the new rotated y-axis
- 3) Rotate γ about the new rotated z-axis

After some matrix algebra, a general conversion from Bunge to OOF Euler angles can be reached as:

$$\alpha = \Phi \quad (5.2a)$$

$$\beta = \text{mod}[(90 - \phi_2), 360] \quad (5.2b)$$

$$\gamma = \text{mod}[(270 - \phi_1), 360] \quad (5.2c)$$

where *mod* is a function that returns the positive remainder, and ϕ_1 , Φ , and ϕ_2 are Bunge Euler angles defined in Chapter 2 (see Section 2.2.1 i)).

5.2 Results from real microstructures using brittle fracture model

The finite element analysis has been completed for specimen grades *A*, *B*, *C*, and *E*. These particular grades are good examples for comparing the influence of the basic microstructural parameters, grain size and contiguity (equivalently, volume fraction), on strength. Effects of grain size can be investigated using grades *A* and *B* (different grain

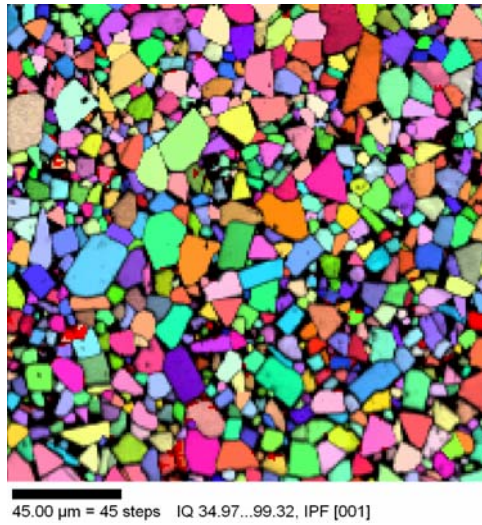
size and same volume fraction), and effects of carbide volume fraction are estimable by grades *B*, *C*, and *D* (similar grain size and different volume fraction). Table 5.2 summarizes the microstructural parameters and measured transverse rupture strength (TRS) for these four grades. All simulations in this thesis using real microstructures are based on these four specimen grades.

Grade	grain diameter (d)	carbide volume fraction (f_c)	contiguity of carbide phase (C)	transverse rupture strength [GPa]
<i>A</i>	5.31 (3.19)	0.88	0.60	1.94 (0.05)
<i>B</i>	1.65 (0.97)	0.88	0.59	3.29 (0.13)
<i>C</i>	1.41 (0.90)	0.82	0.50	2.84 (N/A)
<i>E</i>	1.40 (0.88)	0.69	0.35	2.57 (N/A)

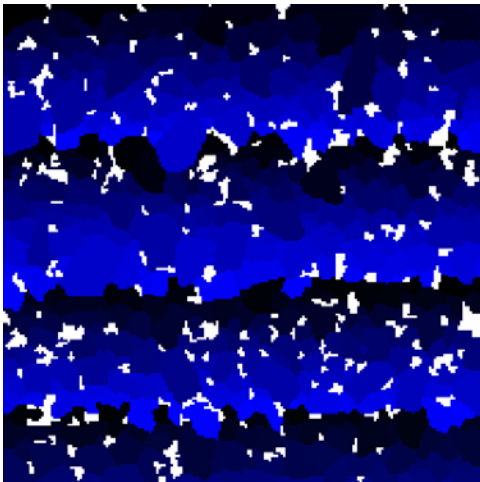
Table. 5.2 : Summary of the microstructural and mechanical properties for grades *A*, *B*, *C*, and *E*.

All the calculation was carried out based on the OIM maps of these four samples. To produce reliable results, three independent sections of each specimen grade have been analyzed. Each section (cropped from a larger map) contains approximately 600 to 900 WC grains and is discretized using ~180,000 to 210,000 triangular elements. To transfer the orientation information in an OIM map to OOF code, we have redefined the colors of individual carbide grains according to their grain identification number (grain ID); different red, green, and blue (R, G, B) values were assigned in each grain. (R, G, B) values were specified in the order of (0, 0, 0) (pure black), (0, 0, 1), (0, 0, 2), ... , (0, 0,

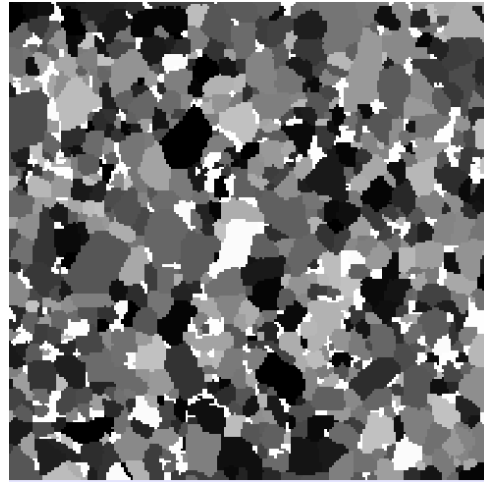
255) (pure blue), (0, 1, 0), (0, 1, 1), ... , (0, 1, 255), (0, 2, 1), ... as grain ID increases. Fig. 5.2 shows an example of input image (from specimen grade A) for OOF simulations. The grain ID starts from the upper-left corner.



(a)



(b)



(c)

Fig. 5.2 : Conversion of colors for OOF simulations (grade A). (a) Original OIM IPF map, (b) new RGB map, and (c) grain map created in OOF code. See text for details.

First, to test the performance of the OOF program, we have calculated the effective modulus (composite modulus) of each grade. In Fig. 5.3, calculated composite moduli (based on 3 sections per grade) are compared to experimentally measured moduli. The error bars indicate the standard deviations in the results from the three sections. It is clear that the calculated moduli for all grades exhibit slightly lower values than the measured data. These systematic negative deviations might be because the Co binder is not pure and, therefore, doesn't have the same modulus as pure Co, which was assumed in the calculation. We can be sure that the binder in the composites contains dissolved W and C and this might increase the modulus by a small amount. Thus, it is assumed that the actual modulus of the Co in the composites is slightly higher than that of pure Co. While the calculations do show systematic differences, it should be emphasized that the absolute values of the errors fall in the range of 1.33 to 2.27 %.

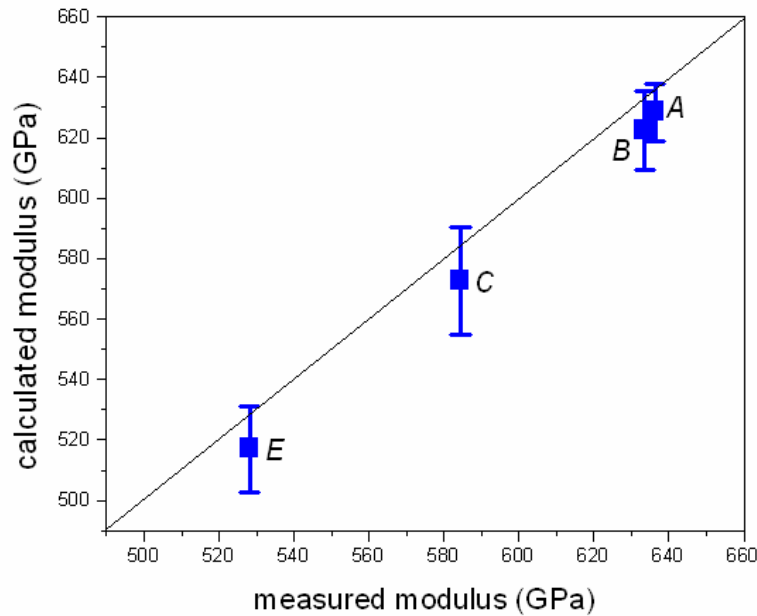


Fig. 5.3 : Comparison of the calculated and measured modulus for each grade. Calculated moduli show systematic negative deviations.

For the calculation of the fracture strength of composites, a thermal load of $\Delta T = -1400^\circ\text{C}$ was applied with a plane stress and fixed (fix (y) the top and bottom during y-elongation and fix (x) the right and left during x-elongation simulations) boundary conditions. Because the composites are sintered in the 1400 to 1600 °C range, the quenching parameter was taken to be $\Delta T = -1400$ °C. The thermal expansion coefficients in the calculations were $\alpha_{11, \text{WC}} = 5.2 \times 10^{-6}/\text{K}$ and $\alpha_{33, \text{WC}} = 7.3 \times 10^{-6}/\text{K}$ for the carbide phase, and $\alpha_{\text{Co}} = 1.4 \times 10^{-5} /\text{K}$ for the binder phase [7]. Here, we assume that the thermal expansion coefficients of the WC and Co phases are constant at all temperatures. An example of an OOF simulation result is given in Fig. 5.4. The distributions of stress invariant 1 ([Pa]) and elastic energy density (arbitrary unit, [a.u.]) are illustrated under a combined load of $\Delta T = -1400$ °C and 0.1 % y-elongation.

Since the surface energies (or fracture energy, γ) for the two crack paths (transgranular along WC/WC boundaries and intergranular in WC crystals) are not available, we calculated the yield strength (YS) as a function of assumed fracture energies. It was found that the calculated YS is linearly proportional to $\gamma^{1/2}$. The linear dependence of yield strength on $\gamma^{1/2}$ can be derived from the Griffith-like brittle fracture criterion (Eq. 5.1). Since the area of a element is proportional to edge length of the element ($A \propto \Delta L$), fracture criterion equation can be written as:

$$2\gamma \leq \frac{1}{2} \sigma_{ij} \varepsilon_{ij} \frac{A}{\Delta L} \propto \frac{1}{2} \sigma_{ij} \varepsilon_{ij} \Delta L \quad (5.3)$$

$$\gamma \propto \frac{1}{4} \sigma_{ij} \varepsilon_{ij} \Delta L \quad (5.4)$$

Here, the linear relationship between stress and strain in the elastic range ($\sigma=E\varepsilon$) reduces Eq. (5.4) to $\gamma^{1/2} \propto \sigma$. This is a plausible explanation for the variation of the calculated yield strength with fracture energies. Based on the relationship between yield strength and fracture energy ($\gamma^{1/2} \propto \sigma$), the yield strengths at all values of the fracture energy can be easily determined from a single calculation of yield strength at a specific fracture energy.

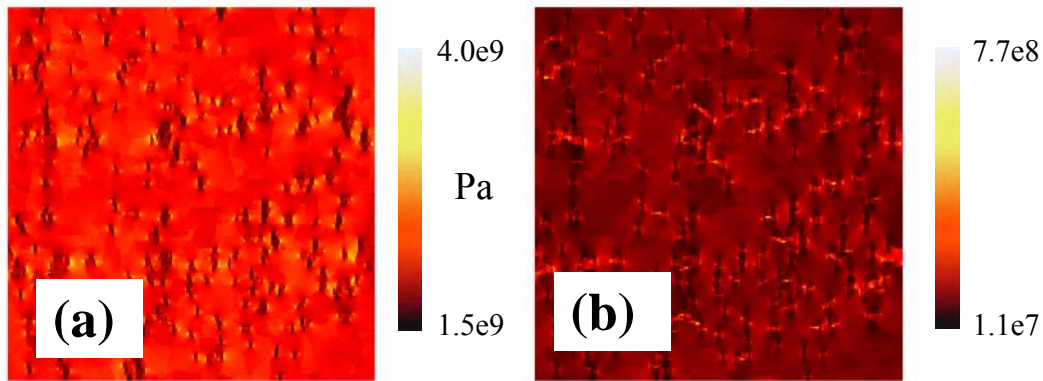


Fig. 5.4 : Stress invariant 1 ([Pa]) and elastic energy density ([a.u.]) distributions (from grade A). (a) Stress invariant 1 under a combined load of $\Delta T=-1400$ °C and 0.1 % y-elongation, (b) elastic energy density under a combined load of $\Delta T=-1400$ °C and 0.1 % y-elongation.

Using a brittle fracture assumption, the calculated yield strength was taken as the fracture strength. As described before, we ignore the plastic process. It should be noted that we do not expect the fracture energies that describes fracture in WC-Co composites to be similar to a WC surface energy. We are assuming a brittle process, even though it is known that plastic processes occur during the failure at these materials. Thus, our assumption is that all of the complete energy dissipation process that occurs during

fracture can be represented by a single average value, γ . Since typical surface energy is of order 1 J/m^2 , we expect this γ to be considerably higher.

Since transverse rupture strength (TRS) is usually used as a measure of strength in WC-Co composites, the effective fracture energy in the carbide phase was calibrated so that the calculated YS of four specimen grades agreed with the measured TRS values. Throughout this thesis, fracture strength is treated as the same quantity as TRS. With the approach described above, we compute the best-fit value of γ , using results for all three sections for each grade. The effective fracture energy was therefore empirically determined to be $\sim 49 \text{ J/m}^2$. This result is remarkably consistent with the reported fracture energy value, $\sim 50 \text{ J/m}^2$ [5]. The calculated results are compared with measured TRS data in Fig. 5.5. The results are averaged based on the analyses of three sections for each grade and the error bars denote standard deviations arising from the variation from section to section. The calculated strengths are consistent with the measured data. All the errors fall within the range of 6 %. This indicates that the constant effective fracture energy assumption provides a useful way to predict the fracture strength of WC-Co composites regardless of the grain size and volume fraction. It suggests that, using the effective fracture energy ($\gamma=49 \text{ J/m}^2$), the strength is plausibly approximated irrespective of the volume fraction. These results indicate that grain size has a negative effect and carbide volume fraction has a positive effect on strength, as is the case with hardness. Furthermore, it appears that coarse-grains are more detrimental to strength than to hardness.

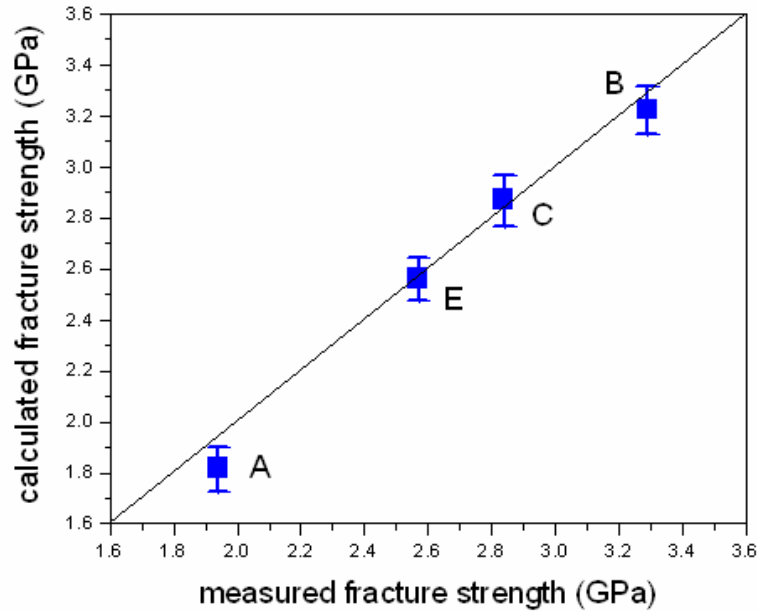


Fig. 5.5 : Comparison of the calculated and measured fracture strength. Error bar denote standard deviation (in sections) of calculated fracture strength. All the calculated fracture strengths are based on the analysis of three sections per each grade.

To examine the effect of the resolution of the digital images on the results of the simulations, we calculated the strength of composites using AFM images as input. There are two disadvantages of using AFM images for OOF simulations. First, an automatic assignment of physical properties (orientations, stiffness, and thermal expansion coefficients) is not possible. In previous simulations, all of the physical parameters were given by automatic assignments. Second, large area simulations are unavailable; whereas one OIM section contains 600~900 carbide grains, one AFM section includes only 120~150 carbide grains. On the other hand, simulations from AFM maps have an advantage in that the resolutions of the AFM images are better than those in OIM maps. Recall that the resolutions are 0.04 (grades *B*, *C*, and *E*) to 0.12 (grade *A*) $\mu\text{m}/\text{pixel}$ in the AFM images, but they are 0.15 (grades *B*, *C*, and *E*) to 1.0 (grade *A*) $\mu\text{m}/\text{pixel}$ in the OIM

scans. In other words, the AFM images have the advantage of accurate boundary positions, but have the disadvantage of limiting the maximum size of the computational section. We compared the calculated strengths from AFM and OIM images and the results turned out to be very similar (not shown). Those results demonstrate that OIM maps can be used to produce accurate simulations even though the boundary positions are not resolved as well as they are in the AFM images. The comparison was made using results from simulations that considered only mechanical loads. It is noteworthy that the simulations performed with only mechanical loads can produce a result that is also consistent with the measured strength data. However, the calibrated effective fracture energy under mechanical loads alone was found to be significantly small than the expected value, $\sim 50 \text{ J/m}^2$. This means that there must be some pre-existing stresses within materials due to cooling and thermal loads are important to for predicting realistic fracture energies in the carbide phase.

For a more realistic calculation of the fracture strength, it is necessary to develop a plastic fracture model that includes the binder plasticity. Currently, however, it is not feasible to develop such a model, since available finite element methods are applicable only to the elastic region. The model described above simply averages all of the energy dissipation processes into effective fracture energy.

5.3 Results from hypothetical microstructures using brittle fracture model

With the model calibrated to calculate the fracture strength of real materials, the fracture strengths of hypothetical microstructures were then calculated to investigate the

effects of microstructural features (the contiguity of the WC phase, the shape of WC grains, and the WC grain size distribution) on fracture strength. To properly evaluate the individual influences of these microstructural features, simple hypothetical microstructures have been generated either from simulations (Monte-Carlo seeding method) or from real microstructures of other composite materials. Because the microstructures of the hypothetical materials could be controlled to produce nearly independent variations in the microstructural parameters, the effects on the fracture strength were clearly revealed. Although some of the hypothetical microstructures presented below are very simple, they clearly demonstrate that the fracture strength can be potentially enhanced through the appropriate control of the microstructural parameters. Because it has been found that the calculated strength under a mechanical load alone also exhibits a consistent result with measured data, only mechanical loads have been applied to the simulations using hypothetical microstructures for contiguity, angularity, size ratio, and size distributions. For the simulations using textured hypothetical microstructures, a combined load was applied.

5.3.1 Contiguity

i) Hypothetical microstructures from simulations

In Fig. 5.6 (a)~(c), three simple hypothetical microstructures with square-shaped crystals are illustrated. These microstructures were designed to have different contiguities while maintaining the carbide volume fraction, grain size, size distribution, and

angularity. Here, color contrast was randomly assigned to distinguish individual grains. These microstructures were created by the following algorithm:

- 1) Determine the desired microstructural features; contiguity (C), average grain size (\bar{d}), standard deviation (σ), maximum and minimum grain size, and carbide volume fraction (f_c).
- 2) Calculate the old contiguity
- 3) Generate a random integer within the range of maximum and minimum grain sizes.
- 4) Calculate the probability for finding the size of the grain in step 1) according to Gaussian distribution:

$$p(r) = \frac{1}{\sigma\sqrt{2\pi}} \exp\left[-\frac{(d - \bar{d})^2}{2\sigma^2}\right] \quad (5.5)$$

- 5) Generate a random number (0 to 1)
- 6) If the calculated probability ($p(r)$) in step 4) is greater than the random number (0 to 1) in step 5), go to step 7). Otherwise, go to step 3).
- 7) Generate random integers (x- and y-positions within domain) to locate the grain created in step 3).
- 8) Calculate the new contiguity using all grains in the domain
- 9) Adjust the contiguity of the microstructure. When the old contiguity is less than the predetermined contiguity in step 1), if the new contiguity is greater than the old one, locate the grain, else discard the grain and go to step 3). When the old contiguity is

greater than the predetermined contiguity, if the new contiguity is less than the old one, locate the grain, otherwise, discard the grain and go to step 3).

10) Calculate the carbide volume fractions. If the calculated carbide volume fraction is greater than the pre-determined fraction (f_c), stop. Otherwise, go to step 3).

With this algorithm, it is possible to control the contiguity with preserving nearly same quantities of other microstructural features. The values of f_c and \bar{d} are the most important parameters to be kept constant, since they have the most significant effect on the properties. In Fig. 5.6, the carbide volume fraction was set to be 0.9 and average grain edge length was ~ 1.5 (arbitrary unit, [a.u.]) in each microstructure. Because the contiguity of real WC-Co composites is ~ 0.59 with carbide volume fraction of 0.9 (specimen grades *A* and *B*), the values selected for the simulation were 0.59, 0.35 and 0.02. The same simulation conditions were used as for the real WC-Co microstructures: plane stress and fixed boundary conditions. But, for the crystallographic properties of WC phase, averaged values of the bulk Young's modulus ($=714$ GPa) and Poisson's ratio ($=0.19$) were used. Since we already tested the effect of crystallographic anisotropies under a mechanical load (see Section 5.2.1 i)), which turned out to be negligible, assigning average moduli and Poisson's ratios will not strongly influence the results.

Fig. 5.6 (d)~(i) shows the stress invariant 1 (hereafter SI1, in units of [Pa]) and elastic energy density (hereafter EED, in units of [a.u.]) distributions with different contiguities (mechanical load alone, 0.1 % y -elongation). It is apparent that stresses and stored energies are more concentrated in the WC phase in the high contiguity microstructure. The dissipation of stresses through WC phase is prohibited by the Co

phase in the low contiguity microstructure. This trend is also found in the data in Fig. 5.7. The average stresses on each phase were averaged from five independent sections created using the algorithm described above. While the average stress on the composites are nearly the same, the average stress ratio of the carbide to binder phase (average stress of WC/average stress of Co) increases as the contiguity increases. The contiguity effect is more obvious when we compare the calculated fracture strengths under mechanical loads in Fig. 5.8. Error bars stand for the standard deviations in five different sections. The estimated fracture strength increases by ~7 % as the contiguity decreases from 0.59 to 0.02. One thing that needs to be noticed is that the width of grain size distributions in these microstructures decreases with the contiguity because we used a probabilistic approach to make hypothetical microstructures. The low contiguity microstructure has a wider distribution whereas the high contiguity microstructure shows a narrower distribution. The normalized standard deviations (σ/\bar{d} , standard deviation/average grain size) are ~0.5, ~0.7, and ~0.8 with the contiguities of 0.59, 0.35, and 0.02. Since it has been found that the wide distribution has a negative effect on fracture strength (see Section 5.3.4), the effects of contiguity in the strength would presumably have been larger if the hypothetical microstructures had the same grain size distribution.

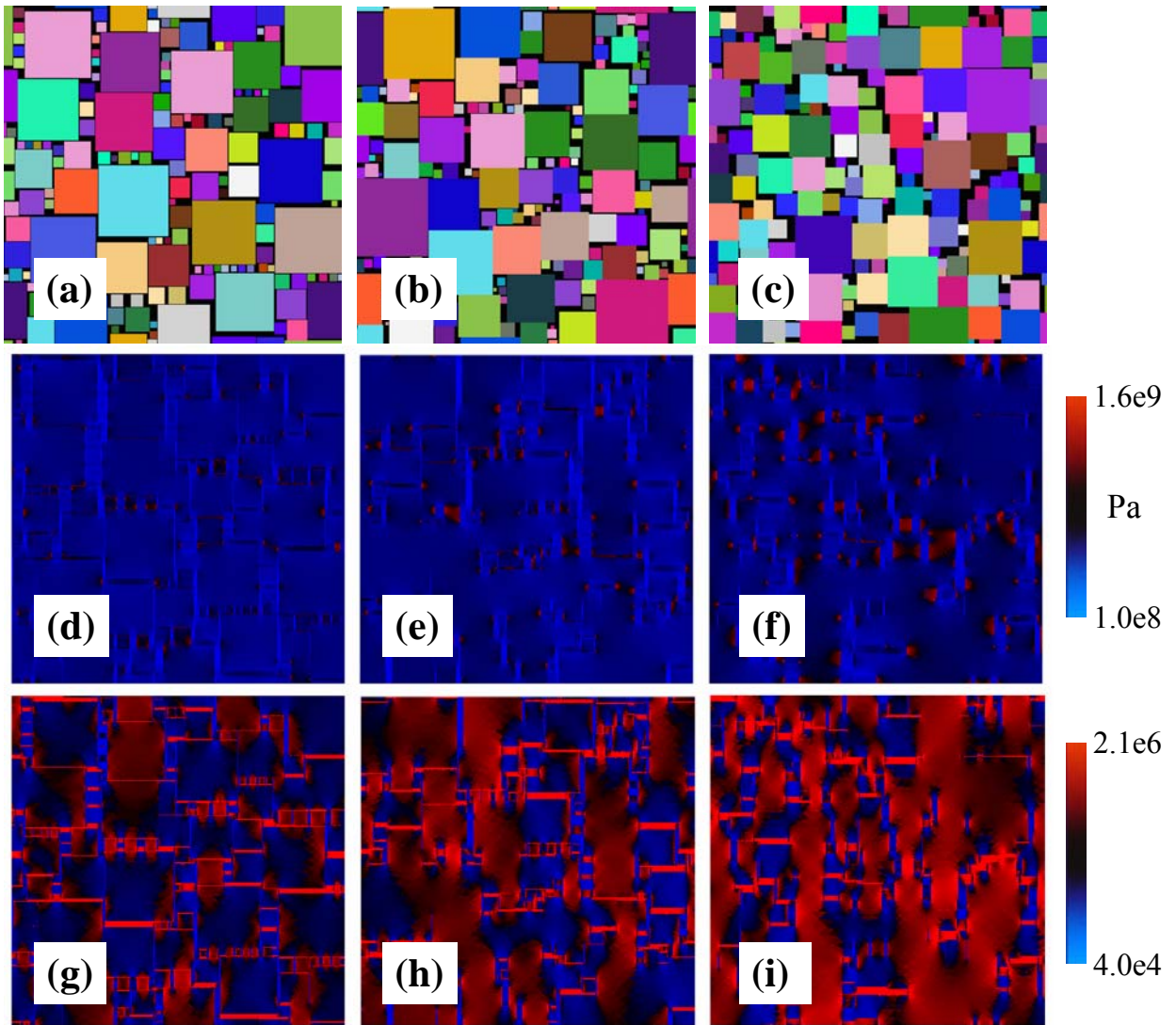


Fig. 5.6 : Examples of hypothetical microstructures with their stress invariant 1 ([Pa]) and elastic energy density ([a.u.]) distributions. Simulations performed under mechanical load alone (0.1 % y-elongation), fixed and plane stress boundary conditions. (a) Low contiguity (0.02) microstructure, (b) medium contiguity (0.35) microstructure, (c) high contiguity (0.59) microstructure, (d)~(f) stress invariant 1 distributions (same scale) for (a), (b), and (c) microstructures, respectively, (g)~(i) elastic energy density distributions (same scale) for (a), (b), and (c) microstructures, respectively. As the contiguity increases, more SI1 and EED are concentrated in the carbide phase.

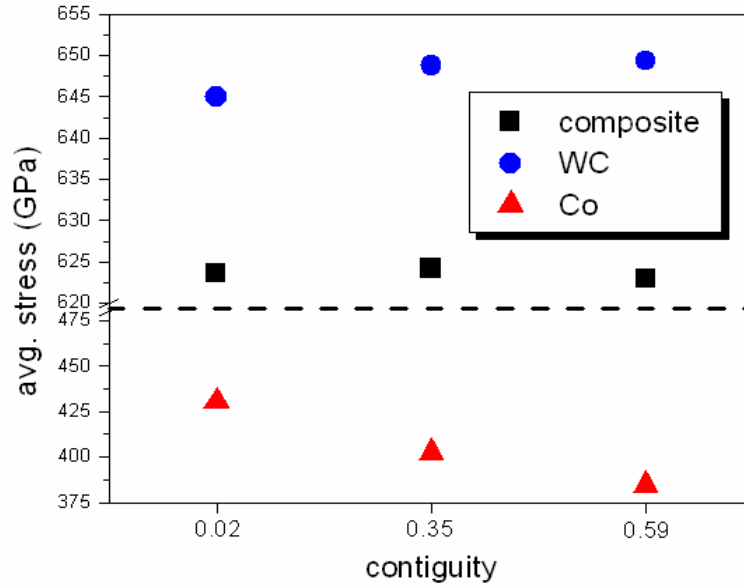


Fig. 5.7 : Average stresses in the composites, carbide and binder phases with different contiguities (0.1% γ -elongation, mechanical load alone, plane stress and fixed boundary conditions). Average stress in the carbide phase increases as contiguity increases. Results from one section (same section shown in Fig. 5.6).

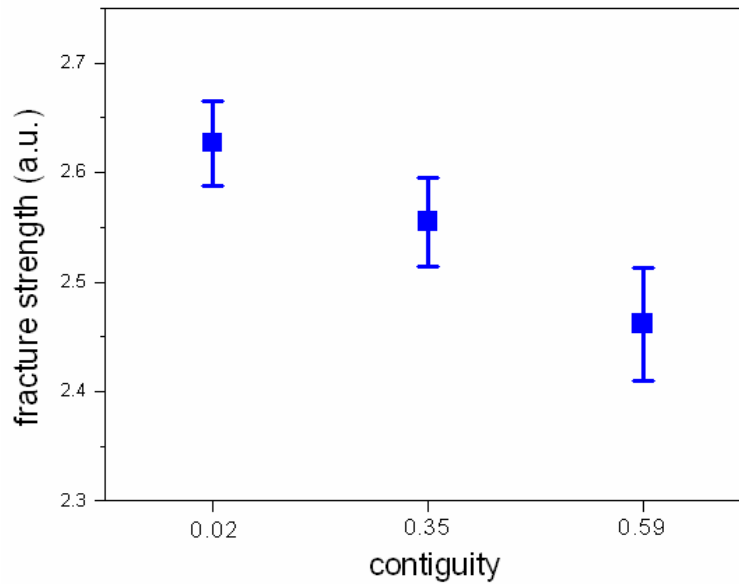


Fig. 5.8 : Plot of the calculated fracture strength ([a.u.]) with different contiguities. Mechanical load with plane stress and fixed boundary conditions was applied. Results are averages of five sections. Error bars represent standard deviations in sections. Hypothetical microstructure with low contiguity has a higher fracture strength.

ii) Hypothetical microstructures from real microstructures

Since the hypothetical microstructures used in previous section are rather simple compared to the real WC-Co composites, modified microstructures were created based on real microstructures in order to test the reproducibility of the contiguity effect on strength. Hypothetical microstructures with same grain size, and carbide volume fraction, but different contiguities were made by the following procedure:

- 1) Specify the desired carbide volume fraction.
- 2) Randomly select a WC/WC grain boundary.
- 3) Convert the selected boundary into Co.
- 4) Calculate the carbide volume fraction.
- 5) If the calculated carbide fraction is greater than the pre-determined carbide fraction in step 1), then go to step 2). Otherwise, return the converted Co phase in step 3) to the original WC/WC boundary and stop.

The shortcoming of this method is that it is not feasible to create a higher contiguity microstructure than the original one; some WC/WC grain boundaries are always eliminated. Hence, the pre-determined carbide volume fraction must be smaller than the fraction in real microstructure. Furthermore, it is not possible to fully control the contiguity. Once the newly calculated carbide volume fraction is less than the pre-determined fraction, the process is stopped. Therefore, in every trial to create a

hypothetical microstructure, the final contiguity cannot be fixed, and it varies within a certain range.

OIM sections of specimen grade *B* ($f_c=0.8992$, $\bar{d}=1.65 \mu\text{m}$) were chosen as the original microstructure because they have the highest contiguity. From these sections, we created microstructures with carbide volume fractions of ~ 0.69 that were analogous to specimen grade *E* ($f_c=0.6949$, $\bar{d}=1.40 \mu\text{m}$). In other words, the hypothetical structure created from grade *B* has same microstructural features as grade *E*, but different contiguity. Of course, the average carbide grain sizes of the hypothetical and real grades *E* are different, but it can be easily modified by changing the size of computational domains in the OOF simulations. Fig. 5.9 contains the hypothetical and real grade *E* microstructures with their responses (EED distribution) to a mechanical load (0.1 % y-elongation). They have a same carbide fraction ($=0.69$) but different contiguities, 0.32 (real) and 0.06 (hypothetical). Here, the EED distribution for only the carbide phase is illustrated for the purpose of visualization (Fig. 5.9 (c) and (d)). It is also seen that the energy propagation through the WC in the low contiguity (hypothetical) microstructure is smaller than in a high contiguity (real) sample. The calculated fracture strengths are 2.53 and 2.71 GPa for the high and low contiguity microstructures, respectively. Note that experimentally measured TRS is 2.57 GPa and standard deviation is ~ 0.09 GPa for specimen grade *E*. While the calculated strength for the real grade *E* (Fig. 5.9 (b)) is close to the measured value, the strength for the hypothetical grade *E* (Fig. 5.9 (a)) is beyond the range of the standard deviation.

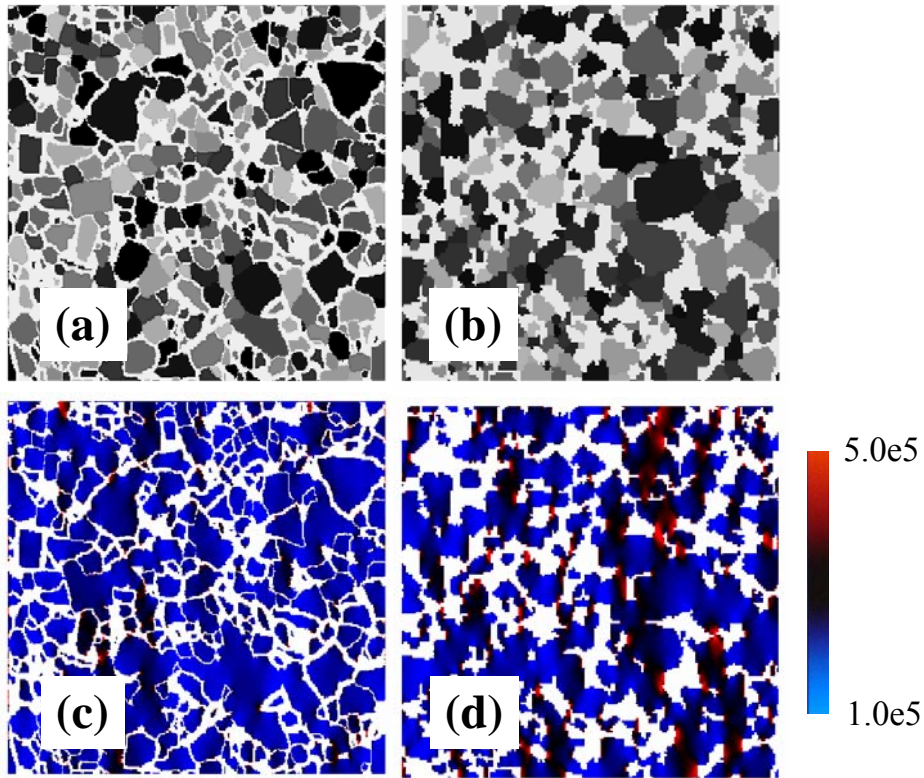


Fig. 5.9 : Examples of hypothetical microstructures with their EED ([a.u.]) distributions. Simulations performed under mechanical load alone (0.1 % y-elongation), fixed and plane stress boundary conditions. (a) Low contiguity (0.06) microstructure (hypothetical grade *E*, from real grade *A*), (b) high contiguity (0.32) microstructure (real grade *E*), (c) and (d) EED distributions (carbide phase, same scale) for low and high contiguity microstructures (a) and (b), respectively. Low contiguity sample shows low EED.

We tested several examples using the ‘WC/WC boundary removal’ method. It turned out none of the high contiguity samples have better performance in strength than the low contiguity ones. Fig. 5.10 shows another example. Here, a hypothetical low contiguity grade *C* ($f_c=0.83$, $C=0.28$) was created and compared with a real sample ($f_c=0.83$, $C=0.50$). In this case also, a high elastic energy density distribution in the carbide phase was observed in the real microstructure and the estimated strengths were 2.80 and 2.93 GPa for the real and hypothetical specimens, respectively (the measured

TRS for grade *C* is 2.84 GPa). The reason for the improved performance of the low contiguity samples is illustrated schematically in Fig. 5.11. When the contiguity is high, the load is transmitted through the carbide phase, which is stiffer. When the contiguity is low, the more compliant binder carries more of the load.

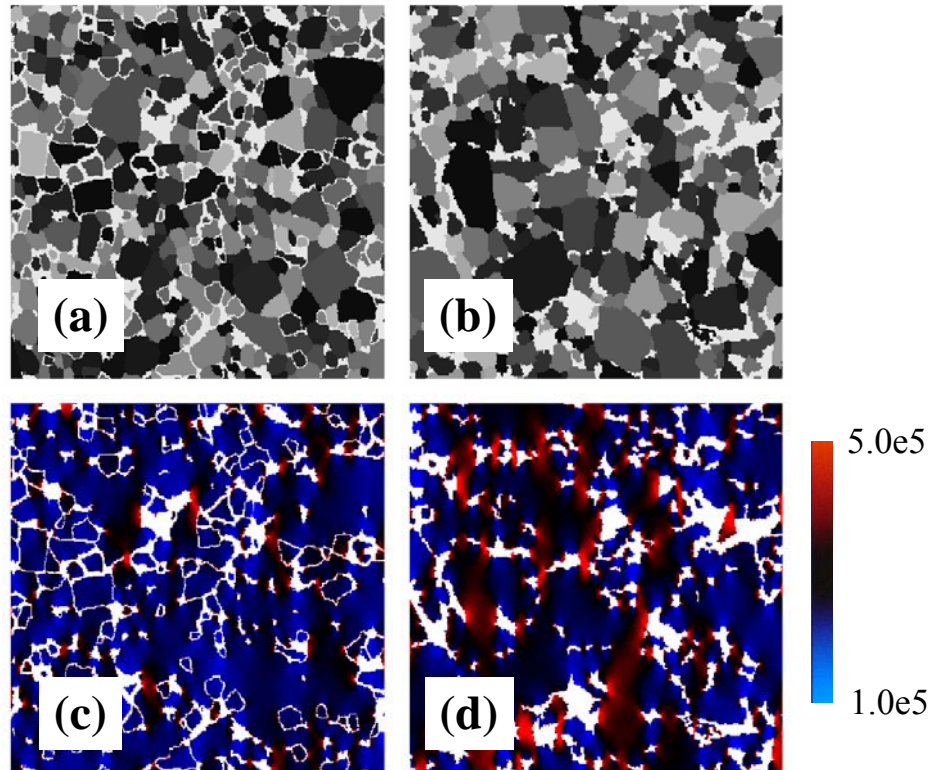


Fig. 5.10 : Examples of hypothetical microstructures with their elastic energy density (a.u.) distributions. Simulations performed under mechanical load alone (0.1 % y -elongation), fixed and plane-stress boundary conditions. (a) Low contiguity (0.28) microstructure (hypothetical grade *C*, from real grade *A*), (b) high contiguity (0.50) microstructure (real grade *C*), (c) and (d) stress invariant 1 distributions (carbide phase, same scale, a.u.) for low and high contiguity microstructures (a) and (b), respectively. Low contiguity sample shows low energy densities.

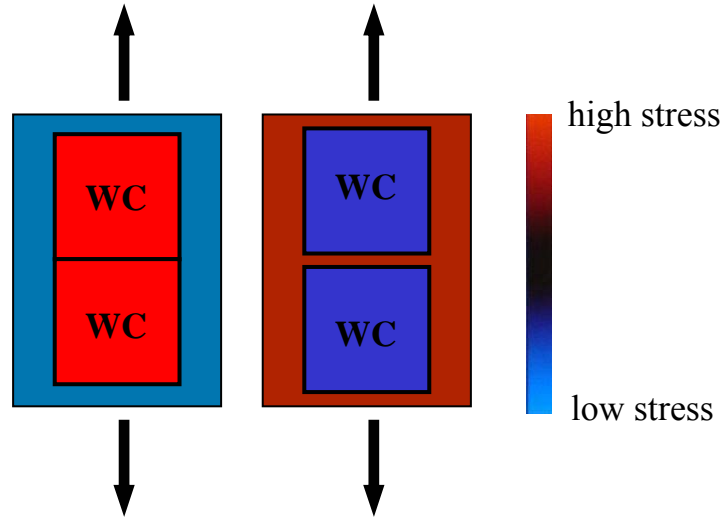


Fig. 5.11 : Schematic illustration of stress distributions of high (left) and low (right) contiguity microstructures. While high stresses are concentrated in WC phase in a high contiguity sample, the propagation of stresses are blocked by Co phase in a low contiguity sample.

5.3.2 Angularity

i) Hypothetical microstructures from simulations

The effect of angularity on strength was explored using hypothetical images with completely dispersed WC particles ($C=0$). Fully dispersed microstructures have been selected because it is difficult to control angularity while maintaining constant finite contiguity. It is, however, already verified that low contiguity microstructures exhibit better strengths. Thus, it can be assumed that we are testing the effect of angularity in the best possible ($C=0$) of constant contiguity.

Microstructures were created with relatively low carbide volume fraction ($=0.55$) to avoid the impingement of carbide crystals. To simplify the situation, we divided microstructures into binary categories; square shapes represent high angularity particles and circles represent low angularity crystals (see Fig. 5.12 (a)~(c)). The locations of WC

crystals were randomly selected. Orientations in the samples with the square shapes were either randomly assigned (square 1, see Fig. 5.12 (a)) or fixed (square 2, see Fig. 5.12 (b)). In Fig. 5.12 (a)~(i), the SII (carbide and binder phases) and EED distributions (carbide phase only) are shown with their corresponding microstructures. Simulations were carried out under mechanical load alone (0.1 % y -elongation), fixed and plane stress boundary conditions. It was found that the samples with square shapes experience higher stresses and elastic energies than those with circular shapes. This is because the stresses and elastic energies are more easily redistributed in the microstructures containing curved interfaces. Also, it has been observed that the microstructure made up of squares with fixed orientations (square 2) shows less SII and EED in the carbide phase than the microstructures with random orientations (square 1). This fact presumably arises from differences in binder free path distributions. As can be seen in Fig. 5.12 (a) and (b), the binder free path distribution in square 1 is wider than that in square 2. This suggests that a uniform distribution of binder free paths leads to an increase in the strength of the composites.

The calculated fracture strengths are plotted in the Fig. 5.13. Only a mechanical load has been applied and the results are averages of five independent sections (error bars indicate standard deviations in results from different sections). Data shows that fracture strength increases by $\sim 3\%$ as the shape changes from square 1 to circle, and the stress ratio (average stress in WC /average stress in Co) decreases by $\sim 6\%$ as the shape changes from square 1 to circle (not shown). Based on the results from simple hypothetical microstructures discussed above (square 1, square 2, and circle), it can be concluded that the low angularity sample has an advantage over the high angularity structure.

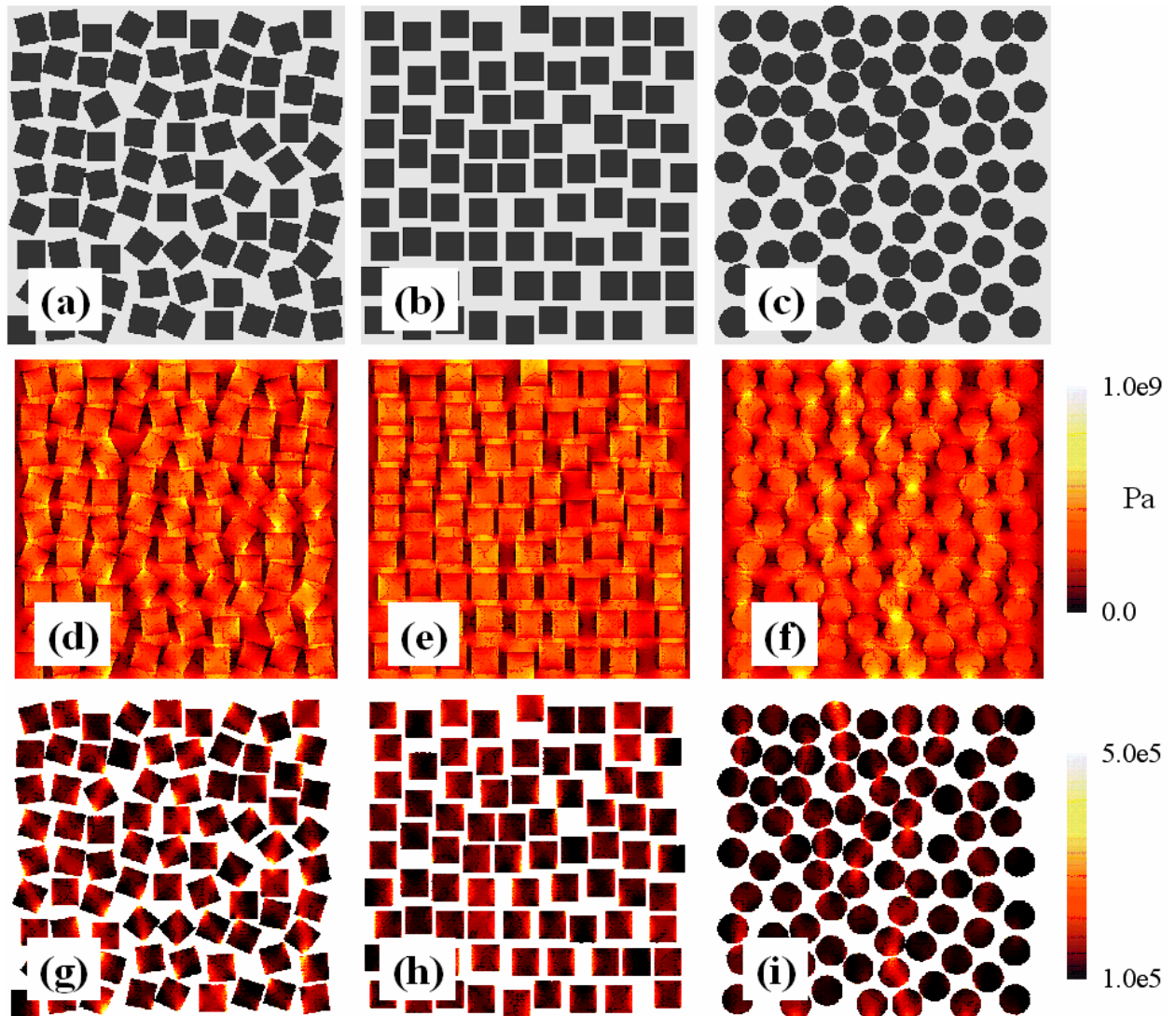


Fig. 5.12 : Examples of hypothetical microstructures with their SII ([Pa]) and EED ([a.u.]) distributions. Simulations performed under mechanical load alone (0.1 % y-elongation), fixed and plane stress boundary conditions. (a) Square microstructure with random orientations (square 1), (b) square microstructure with a fixed orientation (square 2), (c) circle microstructure, (d)~(f) SII distributions (same scale) for square 1, square 2, and circle, respectively, (g)~(i) EED distributions (same scale) for square 1, square 2, and circle, respectively.

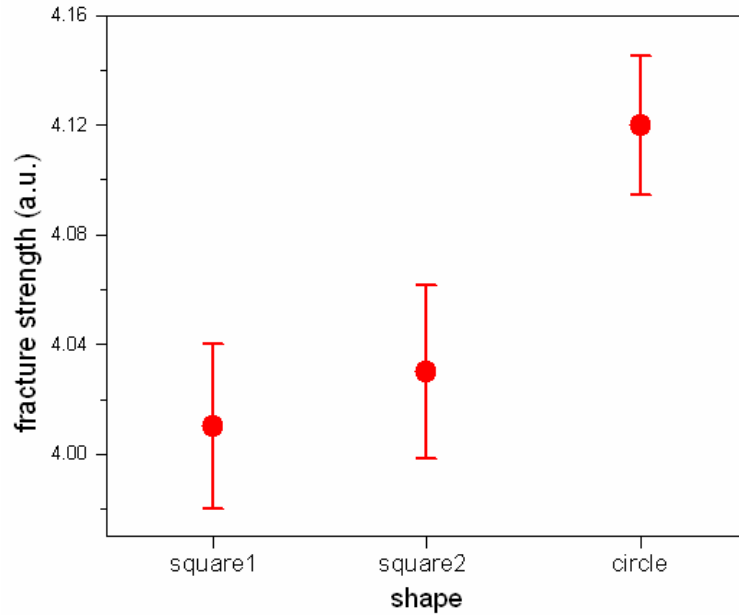


Fig. 5.13 : Plot of the calculated fracture strength ([a.u.]) with different angularities (or shapes). Results are averages of five sections. Error bars represent standard deviations in sections. Hypothetical microstructure with a circle shape shows a higher fracture strength.

ii) Hypothetical microstructures from real microstructures of other composites

The results described above suggest that in a fully dispersed composite with a relatively low carbide volume fractioned, reducing angularity increases strength. To test the generality of this assertion, we made high angularity hypothetical microstructures using the ‘WC/WC boundary removal’ method (see Section 5.3.1 i)) and compared their mechanical response to a low angularity microstructure with a similar contiguity derived from a different composites (W-Ni-Fe alloy, courtesy of A.D. Rollett, Carnegie Mellon University). Fig. 5.14 shows these hypothetical microstructures with their EED distributions ([a.u.]) under a 0.1 % y-elongation mechanical load. The W-Ni-Fe composites have approximately ellipsoidal particles (W) in the Ni-Fe matrix, which is a good model for low angularity microstructures; the ellipsoidal W crystals can be treated

as carbide particles and Ni-Fe matrix can be treated as the Co binder. In the W-Ni-Fe alloy, particle volume fraction and contiguity are calculated to be ~ 0.79 and ~ 0.16 , respectively, so hypothetical angular microstructures of same carbide fraction (0.79) and contiguity (0.16) are generated from a real WC/Co microstructure using the ‘boundary removal’ method described in Section 5.3.1 ii).

Fig. 5.14 (a) is the original OIM micrographs of grade *B*, and (c) is the hypothetical microstructure after WC/WC boundaries were selectively removed. No visible difference was found in EED distributions for these low and high angular microstructures. Fracture strengths were determined to be 2.81 and 2.89 GPa for the low and high angularity sample shown in Fig. 5.14 (a) and (b), respectively. We tested several other sections (low and high contiguity structure with $f_c=0.79$ and $C=0.16$), and the calculated fracture strength in high angularity microstructures from the ‘boundary removal’ method is greater by 0.1 GPa on average. It was found that the dihedral angles at junctions where Co meets a WC bicrystal are important in determining the crack initiation and strength (see Fig. 5.15).

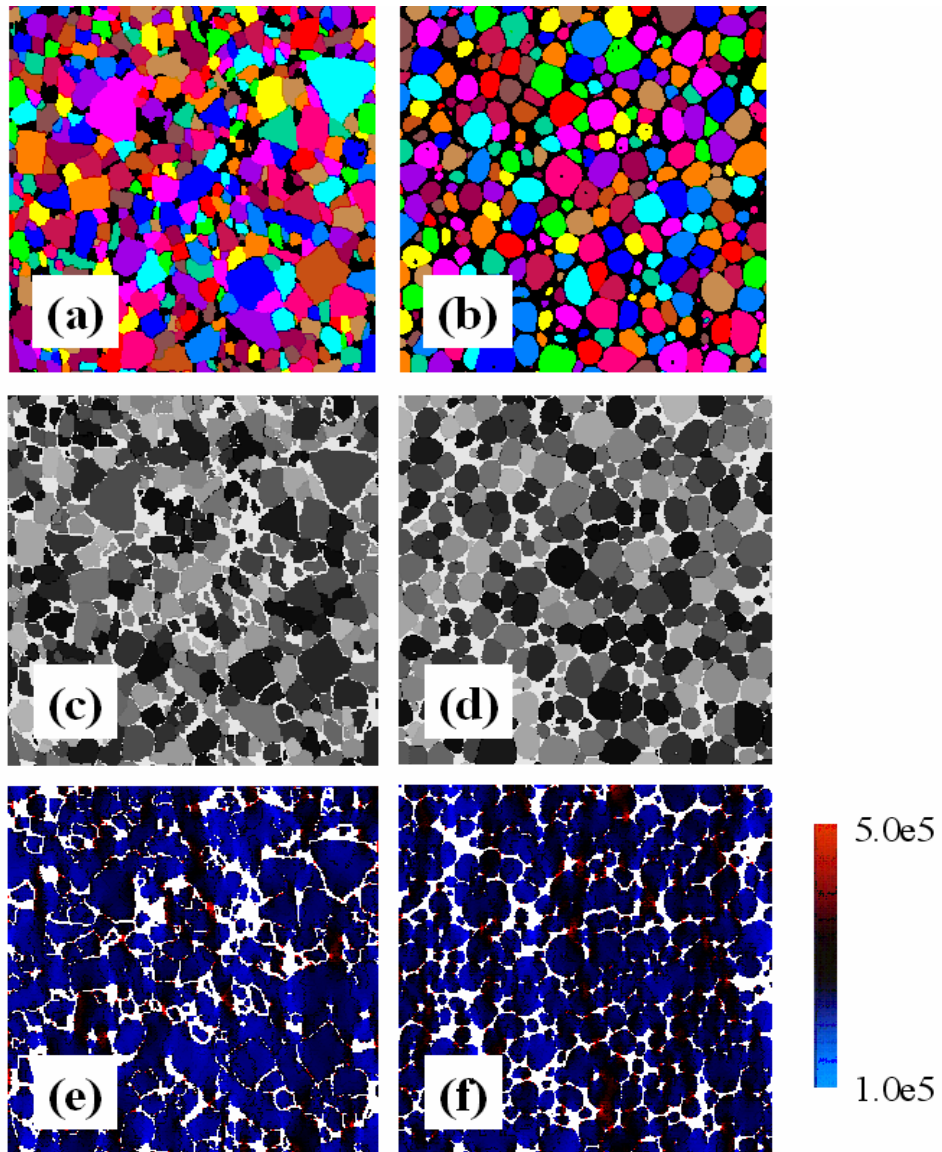


Fig. 5.14 : Examples of hypothetical microstructures with their EED ([a.u.]) distributions. Simulations performed under mechanical load alone (0.1 % y-elongation), fixed and plane stress boundary conditions. (a) High angularity microstructure (original, grade A), (b) low angularity microstructure (W-Ni-Fe alloy, courtesy of A.D. Rollett, Carnegie Mellon University), (c) input for the OOF simulation of high angularity microstructure (WC/WC boundaries were selectively removed, from (a)), (d) input for the OOF simulation of low angularity microstructure (same as (b)), (e)~(f) EED distributions (same scale) for high and low angularity microstructures, respectively. Color contrasts in (a)~(b) are randomly assigned to distinguish individual grains.

The fact that the high angularity structure is better than the low angularity structure seems to be diametrically opposed to the preceding results, but recall that the situations are different. The simulations in the previous section (Section 5.3.2 i)) were carried out under zero contiguity (fully embedded), whereas the current calculations are conducted under finite contiguity ($C=0.16$). Also, the carbide volume fractions are different: ~ 0.55 for the previous and ~ 0.79 for current sections. Therefore, it allows us to conclude that the angularity has two (positive and negative) effects on the strength depending on the carbide fraction and contiguity. When the carbide fraction is small enough and the contiguity is very small, low angularity increases the strength. However, in commercial WC-Co composites, where the carbide fraction is $0.7\sim 0.9$, the spherical or ellipsoidal particles are considered to be detrimental to the strength.

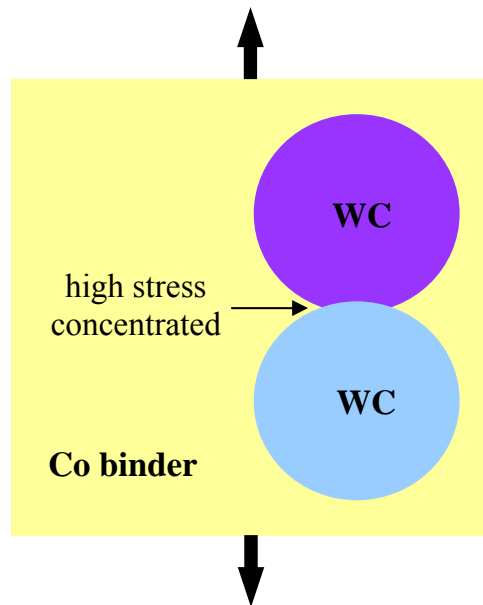


Fig. 5.15 : Schematic illustration of the stress concentration at sharp edge of WC phase in a y-elongation simulation.

5.3.3 Aspect ratio

i) Hypothetical microstructures from simulations

The influence of aspect ratio on the strength is tested by simple hypothetical microstructures using the ‘random location’ method described in section 5.3.2 i). Here, the hypothetical microstructures were again made up of fully dispersed structures. Carbide shapes are modeled as squares and rectangles for fixed aspect ratios of 1:1, 1:2, and 1:4. Fig. 5.16 illustrates an example of hypothetical microstructures, SII (carbide and binder phases), and EED (carbide phase only) distributions under 0.1 % y-direction mechanical strain. Average grain sizes, angularity (each particle consists of four edges), contiguity (=0), and carbide fraction (=0.55) are the same for all of the samples in Fig. 5.16 (a)~(c). High stress and energy concentrations were found along the elongated grains parallel to the direction of the mechanical load (see Fig. 5.16 (f) and (i)). The calculated fracture strengths are compared with different aspect ratios in Fig. 5.17, which shows that the fracture strength decreases by ~4 % as the aspect ratio increases from 1:1 to 1:4. In this plot, the strengths have been averaged from five different sections and error bars represent the standard deviations in sections. The reason for the better performance of the microstructures with equiaxed carbide crystals is schematically illustrated in Fig. 5.18. When the aspect ratio is large, the stress and elastic energy density exhibit wider distribution. The stress and elastic energy is directly transmitted through elongated carbide particles that are parallel to the loading direction. Although the model structures discussed here are very simplified, they clearly show that equiaxed (aspect ratio of 1:1)

shapes can provide better reinforcements than elongated (aspect ratios of 1:2 and 1:4) shapes.

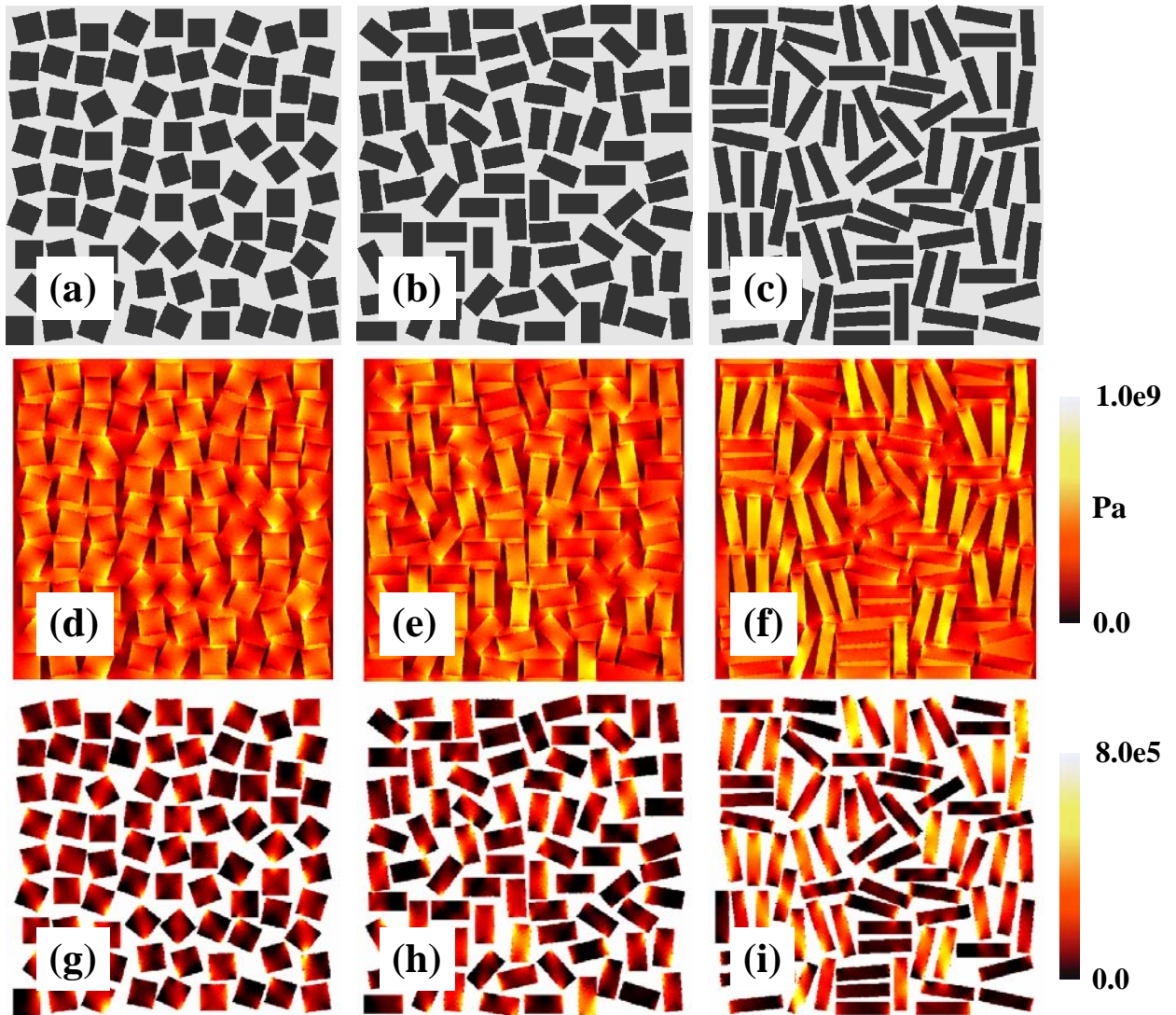


Fig. 5.16 : Examples of hypothetical microstructures with their SII ([Pa]) and EED ([a.u.]) distributions. Simulations performed under mechanical load alone (0.1 % y-elongation), fixed and plane stress boundary conditions. (a) Square microstructure with aspect ratio of 1:1, (b) rectangle microstructure with aspect ratio of 1:2, (c) rectangle microstructure with aspect ratio of 1:4, (d)~(f) SII distributions (same scale) for (a)~(c) structures, respectively, (g)~(i) EED distributions (same scale) for (a)~(c) structures, respectively.

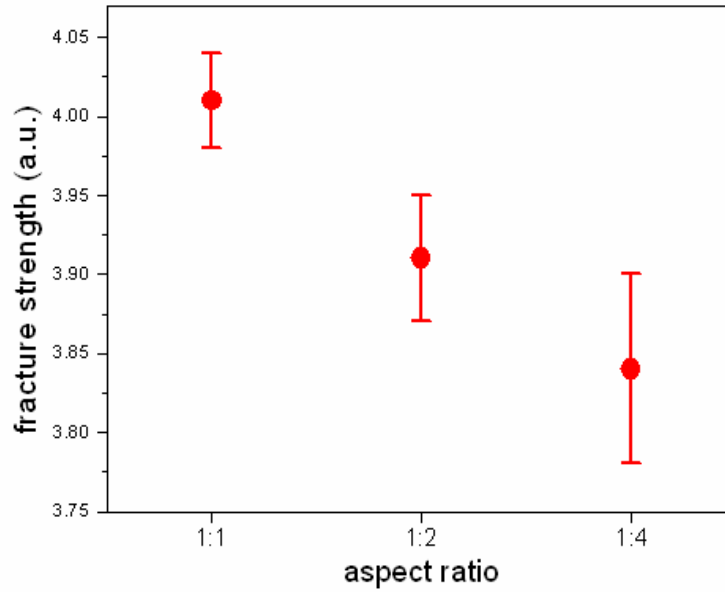


Fig. 5.17 : Plot of the calculated fracture strength ([a.u.]) with different aspect ratios. Results are averages of five sections. Error bars represent standard deviations in sections. Hypothetical microstructure with equiaxed shape has a higher fracture strength.

The effect of aspect ratio on the strength of composites is schematically illustrated in Fig. 5.18. High stresses and elastic energies are easily transmitted through the elongated carbide grains that are parallel to the loading direction. Less stresses and elastic energies were found in the carbide grains elongated perpendicular to the loading direction. In other words, in samples with high aspect ratios, the stress and elastic energy density distributions is wider than those in samples with equiaxed carbide shapes, and this is detrimental to the fracture strength of WC-Co composites.

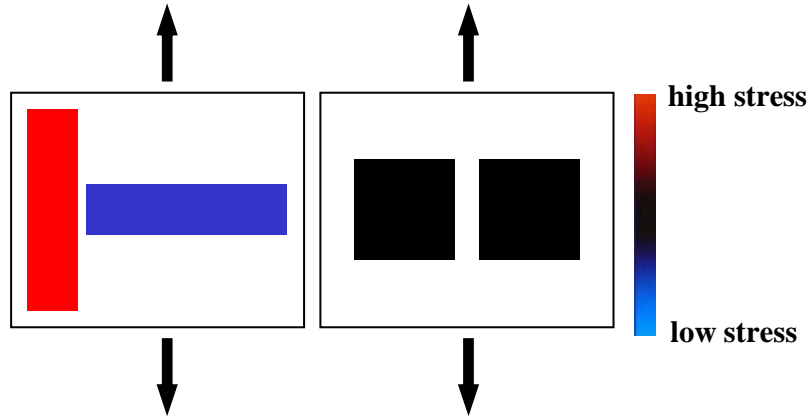


Fig. 5.18 : Schematic illustration of the stress concentrations with different aspect ratios in a y-elongation simulation. High stresses propagate through vertical WC particles (red).

5.3.4 Size distribution

i) Hypothetical microstructures from simulations

The effect of size distributions on strength was investigated in a way that is similar to the studies of angularity and aspect ratio. We assume that the carbide shape is square, the orientation is random, and the carbide particles are fully dispersed ($C=0$). Again, a relatively low carbide volume fraction (≈ 0.55) was assigned in order to avoid impingement of the WC particles. An example of hypothetical microstructures with different square edge size ratio (1:1, 1:2, and 1:4) is given in Fig. 5.19 (a)~(c). The number of small and large crystals in Fig. 5.19 (b) and (c) is identical. EED (carbide phase only, [a.u.]) distributions under 0.1 % y-direction strains are illustrated in the bottom (Fig. 5.19 (d)~(f)). From these images, we conclude that high stresses and elastic energies pass through the large grains rather than small grains (see Fig. 5.19 (d)~(f)). Based on the calculations for fracture strengths (averages of five independent sections) of three different size distributions, it has been found that the fracture strength decreases by

~3 % as the size ratio increases from 1:1 to 1:4 (see Fig. 5.20). Therefore, it is concluded that a homogeneous size distribution will certainly benefit for the strength of WC-Co composites.

The reason for improved strength in samples with a uniform size distribution is illustrated schematically in Fig. 5.21. When the size distribution is wider, the load can be easily transmitted through the larger carbide grains, while the stresses in the smaller grains are low. On the other hand, when the size distributions is narrower (or uniform), the stresses and elastic energies are evenly distributed, thus, the improved strength of composites is expected.

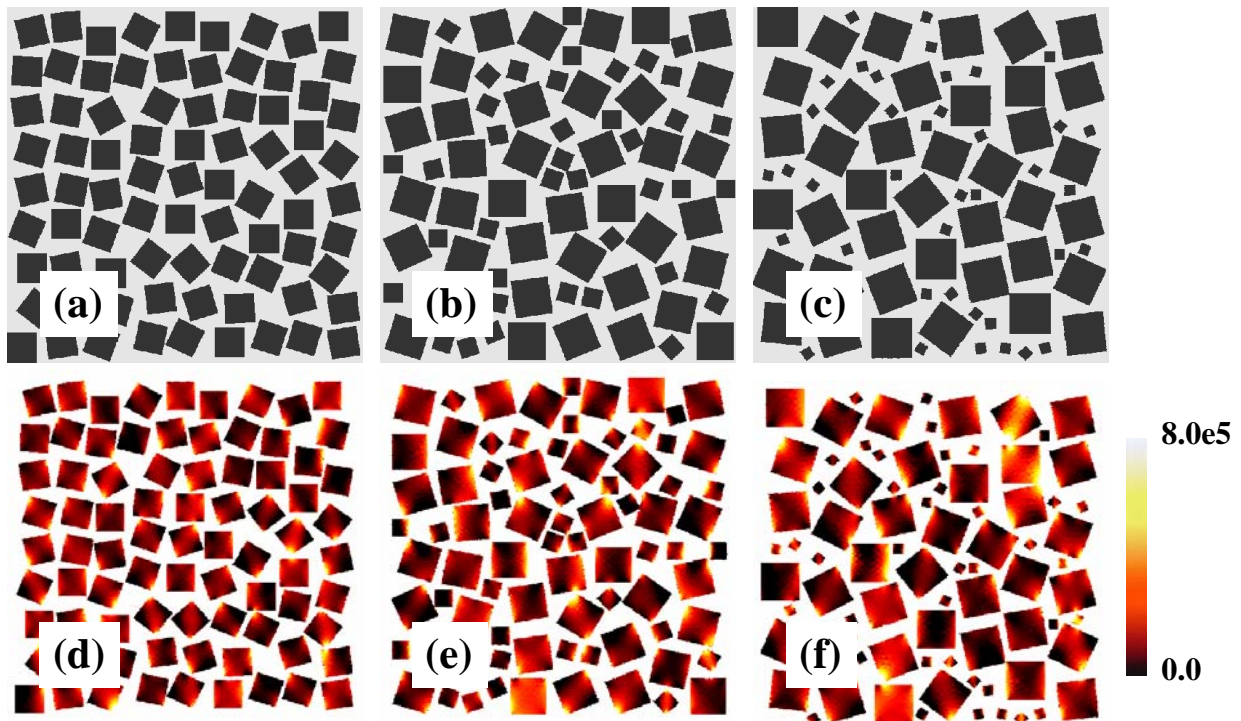


Fig. 5.19 : Examples of hypothetical microstructures with their EED ([a.u.]) distributions. Simulations performed under mechanical load alone (0.1 % y-elongation), fixed and plane stress boundary conditions. (a) Square microstructure with edge size ratio of 1:1, (b) square microstructure with edge size ratio of 1:2, (c) square microstructure with edge size ratio of 1:4, (d)~(f) EED distributions (same scale) for (a)~(c) structures, respectively.

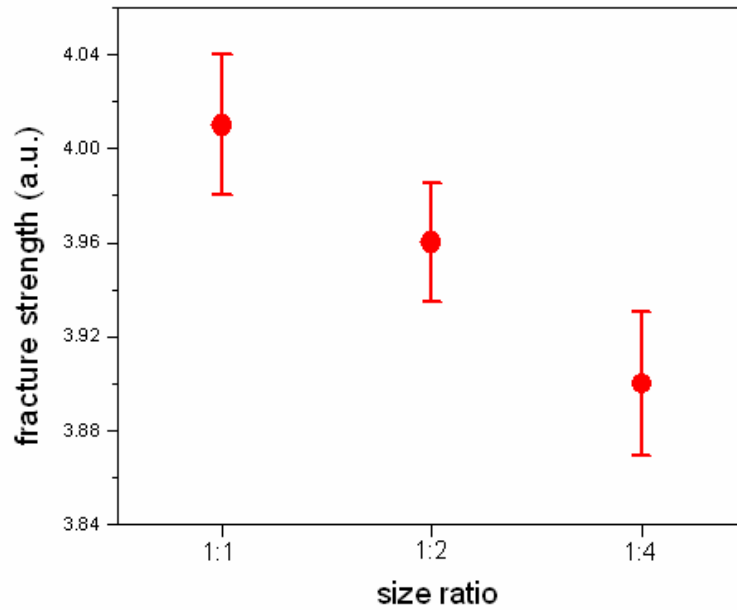


Fig. 5.20 : Plot of the calculated fracture strength ([a.u.]) with different size ratios. Results are averages of five sections. Error bars represent standard deviations in sections. Hypothetical microstructure with homogeneous distribution (1:1 size ratio) has a higher fracture strength.

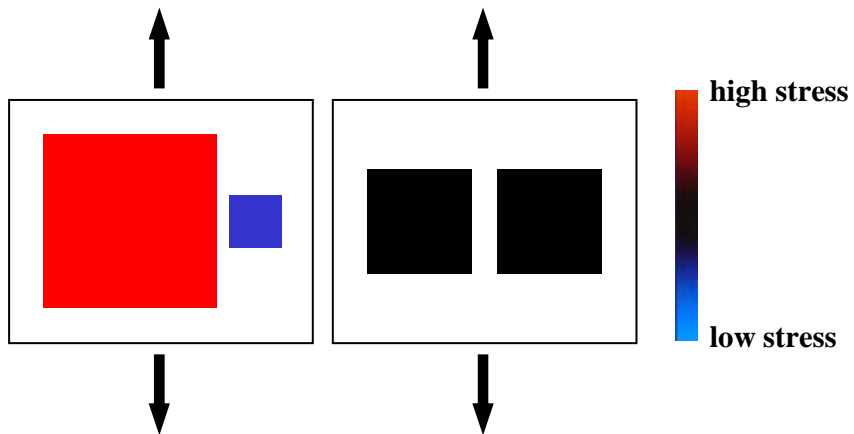


Fig. 5.21 : Schematic illustration of the stress concentrations with different size ratios in a y-elongation simulation. High stresses propagate through large WC particles (red).

Note that all of the simulations for the aspect ratio and size distribution (section 5.3.3 i), and 5.3.4 i)) were executed with a zero contiguity and a low carbide fraction ($=0.55$), which might be thought to be a highly impractical situation. It is, however, considered that these constraints in the simulations do not alter the results. If we have had a finite contiguity and high carbide fraction, the influences of aspect ratio and size distribution would have been much more apparent, because stresses and stored energies in the carbide phase are able to be easily spread out through the adjacent carbide crystals.

5.3.5 Orientation and Misorientation

The effects of orientation and misorientation textures on fracture strength were studied using hypothetical microstructures. We first examined the effects of orientation and misorientation on some simple microstructures, and then tested the orientation texture effects using hypothetical WC-Co microstructures.

i) Simple examples

Fig. 5.22 illustrates three simple microstructures with $(001)^C//[001]^S$ (the (001) plane of crystal is parallel to the [001] direction of sample) orientation. Here, this will be referred to [001] orientation texture. A small square crystal is embedded in another large matrix grain. The three microstructures differ in the misorientation between the dispersed and matrix crystals. Here, the crystals are designated as pseudo-cubic materials whose lattice parameters are cubic, but whose thermal expansion coefficients are different (orthorhombic characters, $\alpha_1=1.00 \times 10^{-5}$, $\alpha_2=0.99 \times 10^{-5}$, and $\alpha_3=1.01 \times 10^{-5}/K$).

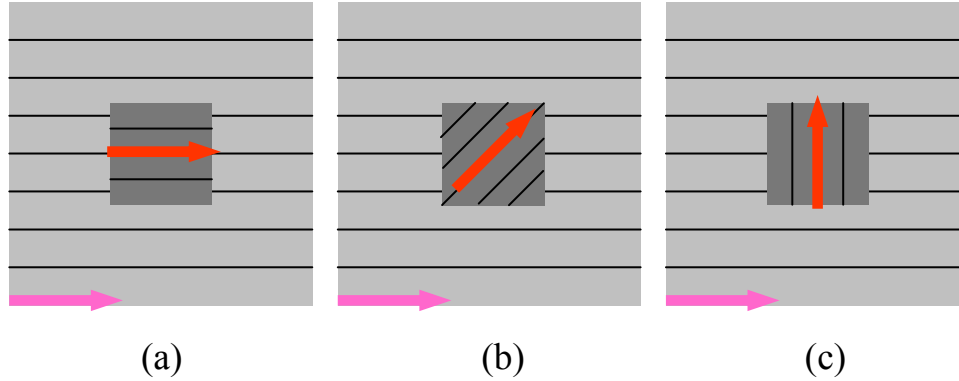


Fig. 5.22 : Schematic illustration of $(001)^C//[001]^S$ orientation texture samples (pseudo-cubic materials) with different misorientations. One crystal is embedded in another matrix crystal. (a) 0° misorientation, (b) 45° misorientation, and (c) 90° misorientation. Red and pink arrows denote a specific direction, $[100]$, for the embedded and matrix crystal, respectively. Section normals point the $[001]$ direction of sample reference frame.

Employing the same idea, a series of simple microstructures (misorientations of 10° to 90°) were prepared and simulated with a thermal load of $\Delta T = -1000^\circ$ with free and plane stress boundary conditions. In the simulation, the assigned physical parameters were: Young's modulus = 500 GPa, Poisson's ratio = 0.33, thermal expansion coefficient $\alpha_1 = 1.00 \times 10^{-5}$, $\alpha_2 = 0.99 \times 10^{-5}$, $\alpha_3 = 1.01 \times 10^{-5}/\text{K}$, and specimen width = 20 μm . Fig. 5.23 and Fig. 5.24 show SII ([Pa]) and EED ([a.u.]) distributions of these microstructures. Although the difference in thermal expansion coefficients is approximately 1~2% along the x-, y-, and z-directions, the stress and energy resulting from those thermal anisotropies clearly show the influence of misorientations. As the misorientation between two crystals increases, the stress and elastic energy associated with the thermal load increases (minimum at a misorientation of 10° , and maximum at a misorientation of 90°).

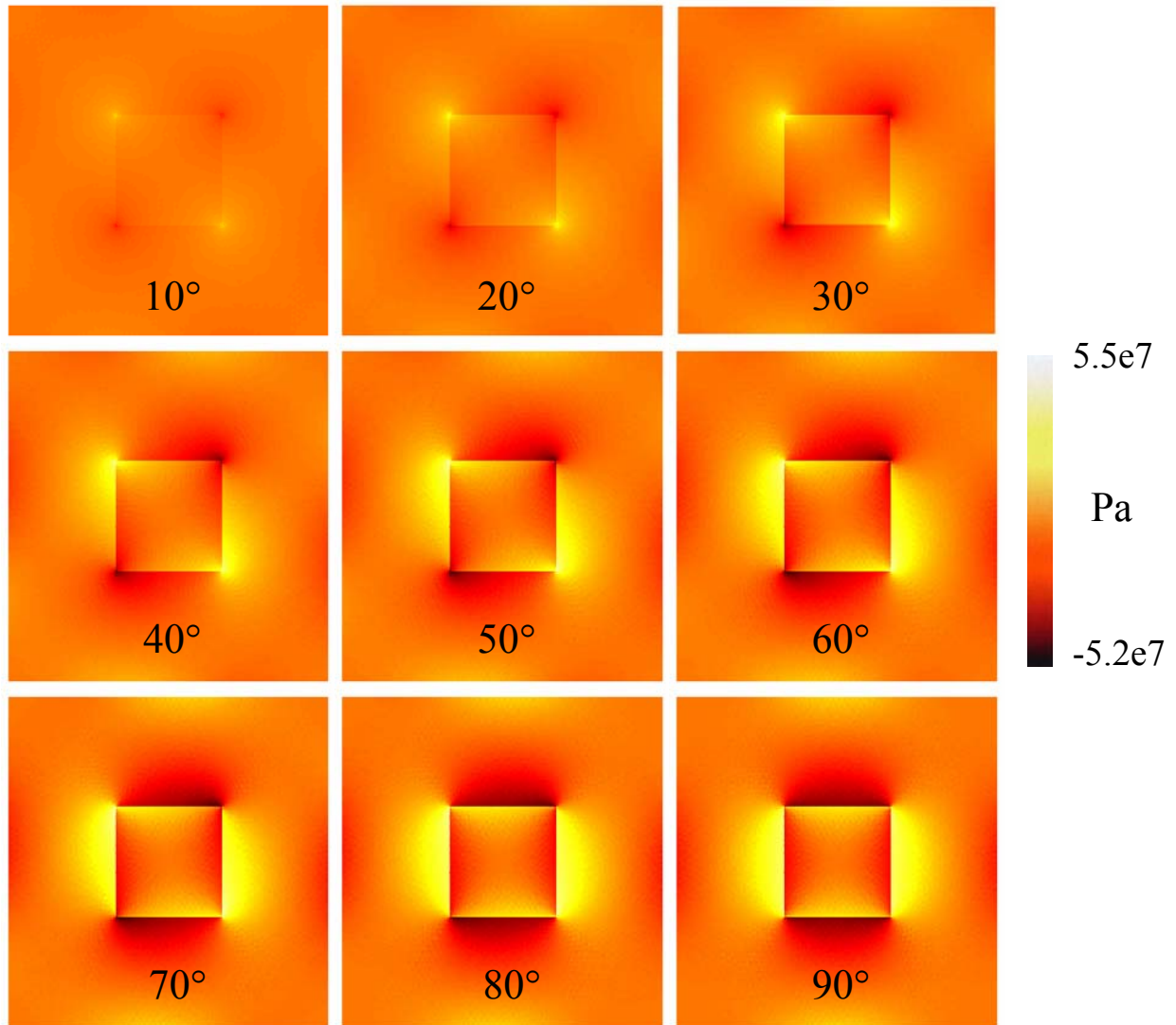


Fig. 5.23 : S11 ([Pa]) distribution of [001] orientation texture samples (pseudo-cubic materials) with different misorientations. $\Delta T = -1000^\circ\text{C}$ with free and plane stress boundary conditions was applied. All plots are same scale. As misorientation angle increases, the stress caused by different thermal expansion coefficients increases.

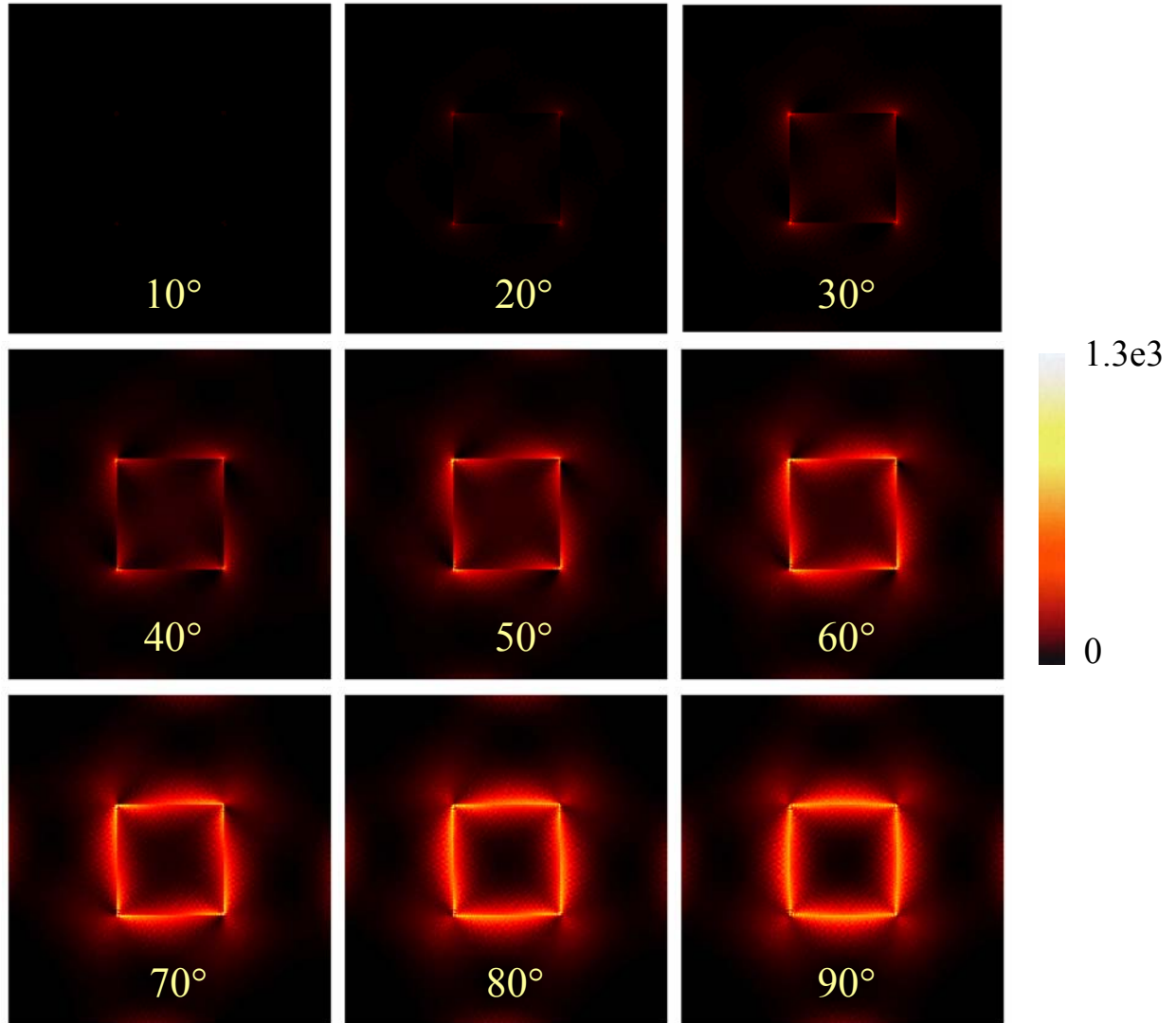


Fig. 5.24 : EED ([a.u.]) distribution of [001] orientation texture samples (pseudo-cubic materials) with different misorientations. $\Delta T = -1000^\circ\text{C}$ with free and plane stress boundary conditions was applied. All plots are same scale. As misorientation angle increases, the stored energy caused by different thermal expansion coefficients increases.

To generalize the misorientation effect on residual stresses and energies, we have tested another set of microstructures. In this case, nine square crystals reside in the computational domain and they all have different orientations (see Fig. 5.25 (a)~(d)). Among them, the first two (Fig. 5.25 (a) and (b)) has $(001)^{\text{C}}//[001]^{\text{S}}$ have orientation

texture, and the last two (Fig. 5.25 (c) and (d)) do not have any orientation texture (random orientations). Note that the orientation distribution in each pair of microstructures is preserved; the only thing that is changed is the arrangement of the crystals. In other words, rearranging the crystals in sample (a) makes structure (b), and rearranging the crystals in (c) makes microstructure (d). The microstructures have been constructed such that the average misorientation is maintained as low as possible in the sample (a) and (c), and as high as possible in the specimen (b) and (d), under fixed orientation distributions. The numerical values in the textured sample (Fig. 5.25 (a) and (b)) indicate orientations with respect to a certain reference frame, so the misorientation between two crystals is the difference of the corresponding orientations (all tilt boundaries). The average misorientations were calculated to be 20°, 35°, 28°, and 50° for the microstructures of (a), (b), (c), and (d) in Fig. 5.25.

The stress and energy distributions under a thermal load ($\Delta T = -1000^\circ\text{C}$) are depicted in Fig. 5.25 (e)~(l) with the corresponding microstructures. The boundary conditions and physical properties used in these simulations were exactly the same as those described in the preceding section. All SI1 and EED distributions are plotted in a same scale. Low SI1 and EED distributions were observed in samples with a small average misorientation angle (compare the first and second columns, third and fourth columns in Fig. 5.25). As expected, the residual stress and energy are more concentrated along the high angle boundaries (the boundaries between 0 and 50, 10 and 60, and 10 and 80 in Fig. 5.25 (f) and (j)). On the other hand, at the low angle boundary (the boundary between 50 and 60 in Fig. 5.25 (f) and (j)), the intensities of stress and elastic energy were almost negligible compared to those at a high angle boundary. The same trend was

found in the randomly oriented microstructures (the third and fourth columns in Fig. 5.25). The results demonstrate that it is feasible to diminish the stored energies and increase the fracture strength by rearranging crystals with the same orientation distributions.

The effect of the orientation distribution was also investigated (compare the second and third columns in Fig. 5.25). Recall that microstructure (b) has an average misorientation of 35° and microstructure (c) has an average misorientation of 28° . Even though the average misorientation of (b) is smaller than that of (c), the residual stress and energy in (c) are much larger than those in (b). For example, the maximum elastic energy densities are 1.2×10^3 , and 2.6×10^3 ([a.u.]), and the average energy densities are 3.49, and 6.39 ([a.u.]) for (b) and (c), respectively. This means that the three dimensional mismatch in the lattice will produce more stress and strain energy, and it suggests that these stresses and energies are able to be reduced by controlling the orientation textures. It is generally accepted that the orientation texture reduces the stored energy in polycrystalline materials, but there is a wide range of possibilities depending on the associated misorientations (see Fig. 5.26). We have also calculated the fracture strength in these microstructures under thermal load of $\Delta T = -1000^\circ\text{C}$. Although the results are based on simple microstructures, the data in Fig. 5.27 show that the fracture strength can be greatly increased by increasing the orientation texture and reducing misorientations.

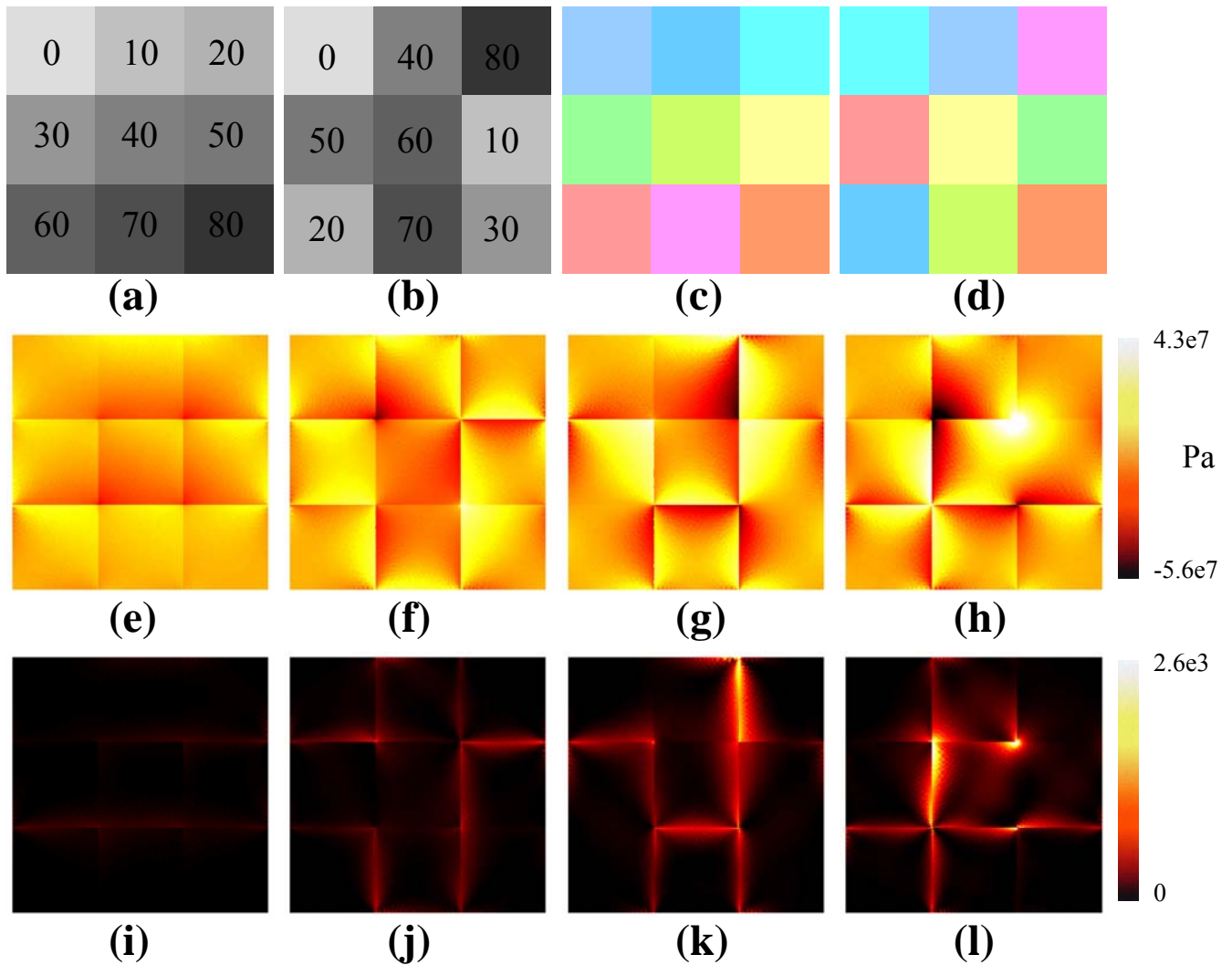


Fig. 5.25 : Effects of orientation and misorientation distributions on stress ([Pa]) and elastic energy density ([a.u.]) distributions. (a) Microstructure with a $(001)^C//[001]^S$ orientation texture and a small misorientation angle, (b) microstructure with a $(001)^C//[001]^S$ orientation texture and a high misorientation angle, (c) microstructure with random orientations and a small misorientation angle, (d) microstructure with random orientations and a high misorientation angle, (e)~(h) SI1 distribution for microstructures (a)~(d), (i)~(l) EED distribution for microstructures (a)~(d), respectively. Samples with the $(001)^C//[001]^S$ orientation texture display low stress and energy. Also, samples with a small misorientation angle show low stress and energy distributions. See text for details.

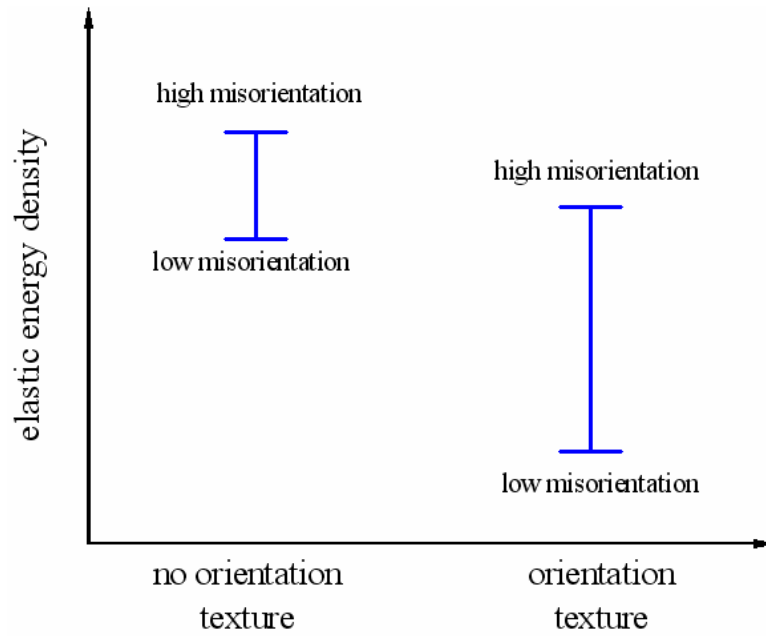


Fig. 5.26 : Stored energy density variation with orientation and misorientation textures. Generally, materials with a high orientation texture display a low energy density distribution than materials with random orientations. The range of stored energy density distribution is much wider in samples with orientation textures.

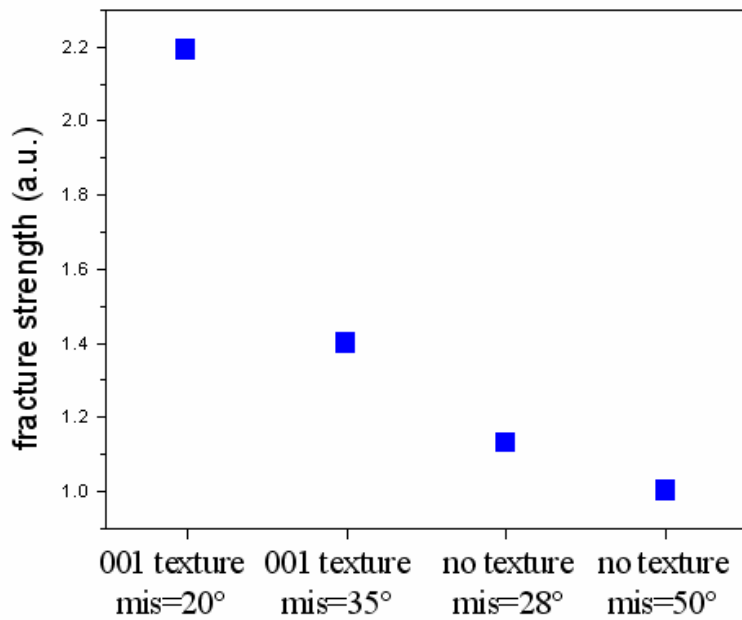


Fig. 5.27 : Estimated fracture strength in materials (Fig. 5. 25 (a)~(d)). The sample with $(001)^c/[001]^s$ orientation texture and a small misorientation shows the highest performance.

ii) Hypothetical microstructures

In the previous section, we verified that strength could be enhanced by orientation and misorientation texture. To employ this idea to WC-Co composites, model microstructures with orientation textures are proposed. Here, we neglect the geometrical constraints to orientations. In real WC-Co materials, the orientation is related to the geometry (shape) in the two-dimensional sections. For example, the $\langle 0001 \rangle$ axis of a red crystal (usually observed in a triangular shape) in an OIM IPF map (see Fig. 4.6) must be nearly parallel to the $[001]$ sample axis. In other words, the orientations are strongly correlated with the two-dimensional shapes that appear in planar sections. In the simulations described here, this correlation will be removed.

To impose some textured orientations, we first generate a set of random Euler angles and calculate the angle between a certain crystal axis and a fixed sample axis. Fig. 5.28 illustrates the deviation angle (Δ) between $[001]$ sample axis and $\langle 0001 \rangle$ crystal axis.

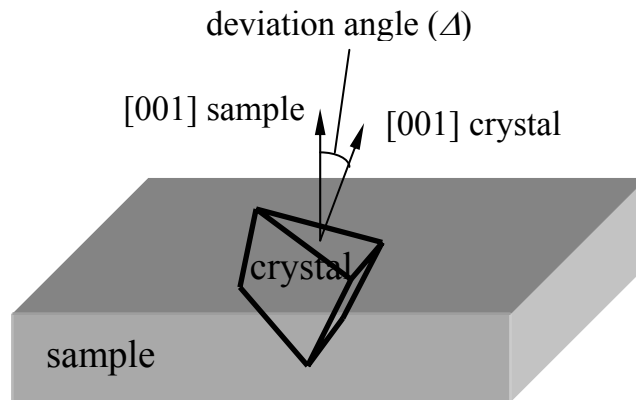


Fig. 5.28 : deviation angle (Δ) between the $[001]$ sample axis and a $\langle 0001 \rangle$ crystal axis.

We then compute the probability of finding a crystal with the randomly assigned Euler angles according to the following formula:

$$p = \exp(-\Delta / \beta) \quad (5.6)$$

where Δ (in degrees) is the angle between a crystal axis and a sample axis, β is a constant that determines the intensity (or degree) of orientation texture, and p is the probability of finding a crystal with a deviation angle of Δ . We used $\beta=2, 10$, and 25 to construct qualitatively high, medium, and low orientation textured microstructures, respectively. Fig. 5.29 shows the probability (p) as a function of the orientation texture intensity constant, β , and difference in angles, Δ , between the crystal and sample axes. It is clearly seen that in the high texture ($\beta=2$), the probability of finding a crystal with a deviation angle (Δ) greater than 10° is nearly 0. We then generate another random number (0 to 1) and if the random number is less than the computed probability (Eq. (5.6)), the pre-assigned Euler angles are accepted, otherwise, they are discarded. The process is repeated for all of the carbide crystals. In this manner, hypothetical microstructures with $(001)^C//[001]^S$ ([001] texture), $(100)^C//[100]^S$ ([100] texture), and $(111)^C//[111]^S$ ([111] texture) orientation textures were created. Here, for convenience, the three-digit notation (instead of the four-digit notation) is used for the plane normal and axis directions of hexagonal materials.

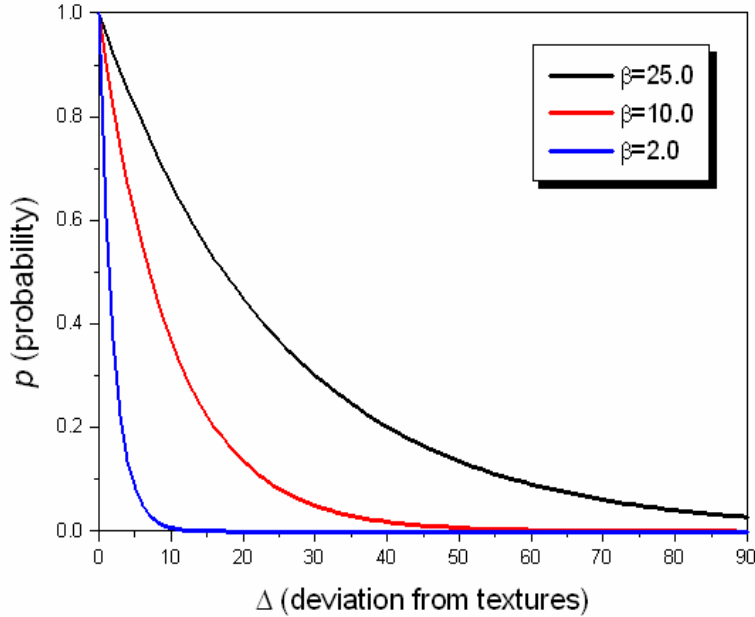


Fig. 5.29 : Probability of finding a crystal as a function of texture intensity factor (β) and deviation angle (Δ) from a sample axis.

Composite moduli were first calculated using these microstructures with hypothetical orientations (see Fig. 5.30). The results presented here are all based on hypothetical microstructures derived from a section of grade A. There are nine distinct models, three (high, medium, and low) [001] textures, three [100] textures, and three [111] textures. In Fig. 5.30, moduli of the [001] and [100] textured samples were calculated by averaging the results from the x- and y-elongation simulations. However, the modulus of [100] textured sample was measured separately because the responses along the x- and y-directions are fairly different. This difference results from the anisotropy of elastic constants of WC. Remember that the stiffness along c-axis (C_{33}) in the WC crystal is much higher than other directions ($C_{11}=720$, $C_{33}=972$, $C_{44}=328$, $C_{12}=254$, $C_{13}=267$ GPa). Therefore, in the [001] textured sample, the stiffness along the x- ([100] of sample) and y- ([010] of sample) directions is the averaged by the elastic constants of the axes

perpendicular to c-axis (see Fig. 5.31 (a)). Likewise, the anisotropy in the stiffness doesn't affect the modulus of the x- and y-directions in the [111] textured sample. On the other hand, in the [100] textured sample, the prismatic facets are mostly perpendicular to x-direction and basal planes are facing the y-direction of the sample reference frame (see Fig. 5.31 (b)). This explains the difference in modulus along the x- and y-directions in the [100] textured sample. Fig. 5.30 describes the calculated modulus of the nine different materials. The dotted horizontal line denotes the experimentally measured modulus of real (no orientation texture) grade A. It is clear that as the degree of the texture decreases ($\beta=2 \rightarrow 25$), the calculated modulus approaches to the measured value. The modulus of the [001] textured sample is always lower than the measured value since the stiffest axis (c-axis) was excluded in the calculation. In the case of the [100] textured sample, the modulus along c-axis direction (y-direction of sample) is invariably higher than the measured quantity, and the modulus along the direction perpendicular to c-axis (x-direction of sample) is lower than the experimental value. The modulus of [111] texture is nearly same as the measured quantity, which means the response is almost isotropic along the x- and y-direction of sample reference frame.

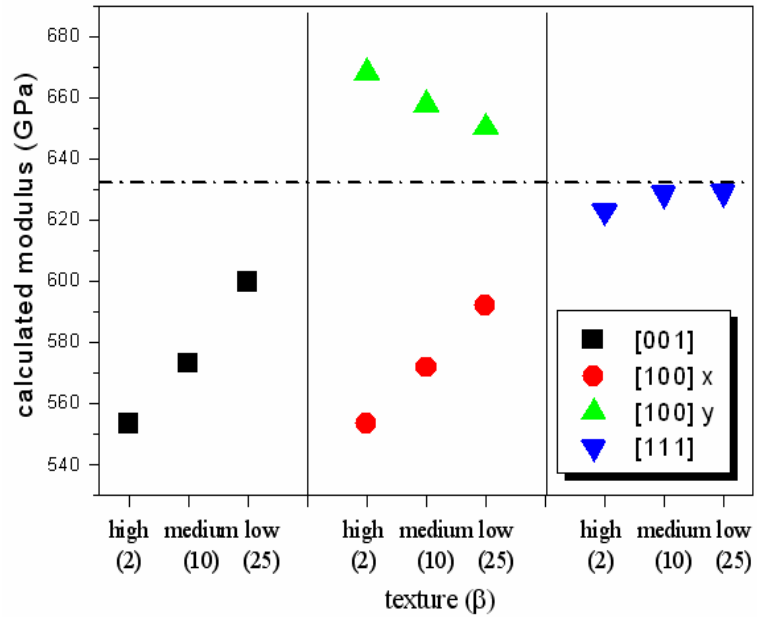


Fig. 5.30 : Calculated modulus with different orientation textures (from grade A). Dotted line indicates experimentally measured modulus. As the degree of texture decreases, the calculated modulus approaches to the measured value. See text for details.

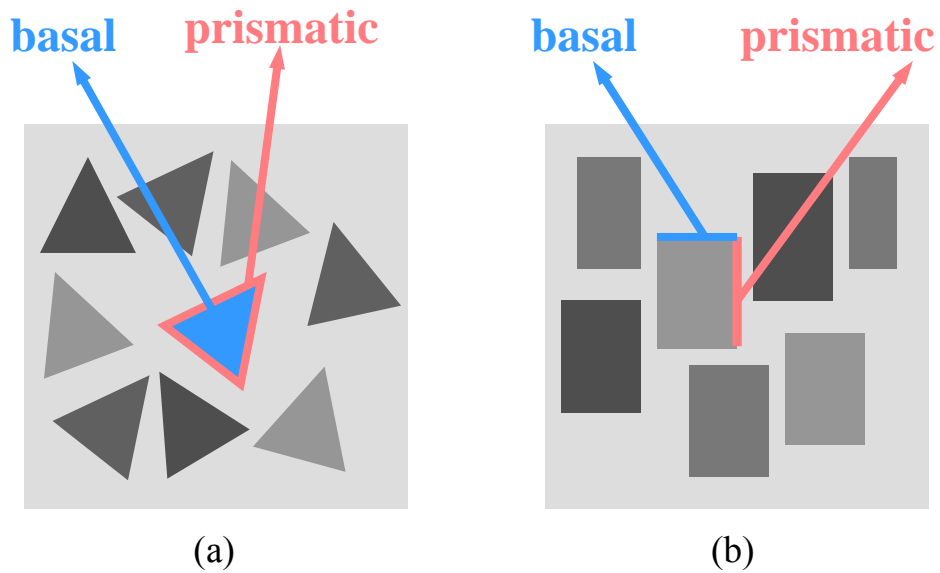


Fig. 5.31 : Schematic illustration of the orientation in (a) [001] texture, and (b) [100] texture. The shapes merely represent the orientations, not the actual shape of hypothetical microstructures.

The SI1 and EED were then computed for these hypothetical microstructures (see Fig. 5.32 and 5.33). A thermal load of $\Delta T = -1400^\circ\text{C}$ was applied with free and plane stress boundary conditions. The same scales were used for SI1 and EED to visualize the relative distributions. The distributions in the real microstructure (no texture) are illustrated at the bottom of Figs. 5.32 and 5.33. It is apparent that the sample with high [001] texture shows reduced stresses and energy densities. As the intensity of texture decreases, the stress and energy distributions resemble the original distribution.

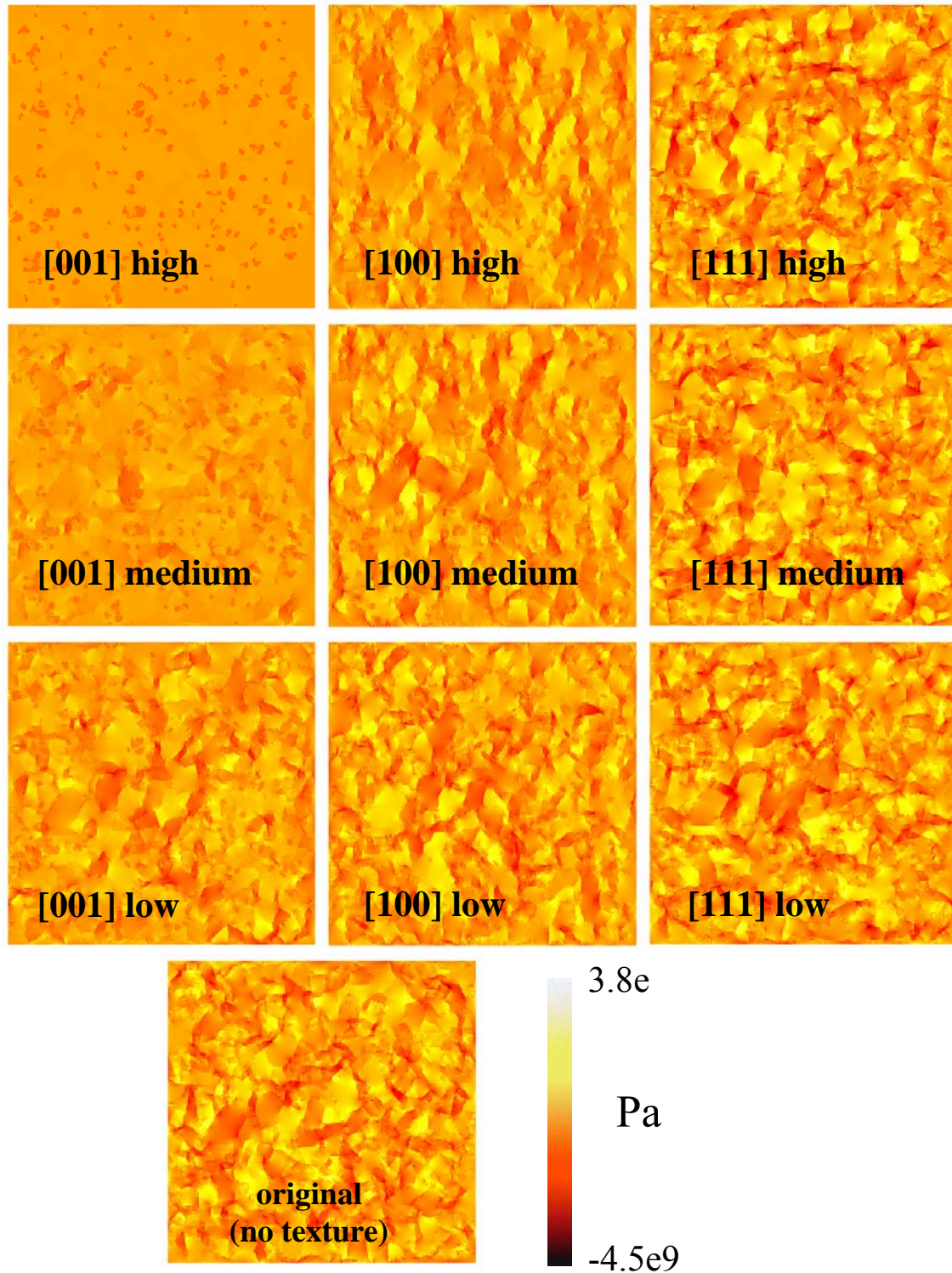


Fig. 5.32 : S11 ([Pa]) distributions with different orientation textures (from grade A). A thermal load of $\Delta T = -1400^\circ\text{C}$ was applied with free and plane stress boundary conditions. Same scale was used. The high [001] texture (upper-left) shows a low stress distribution.

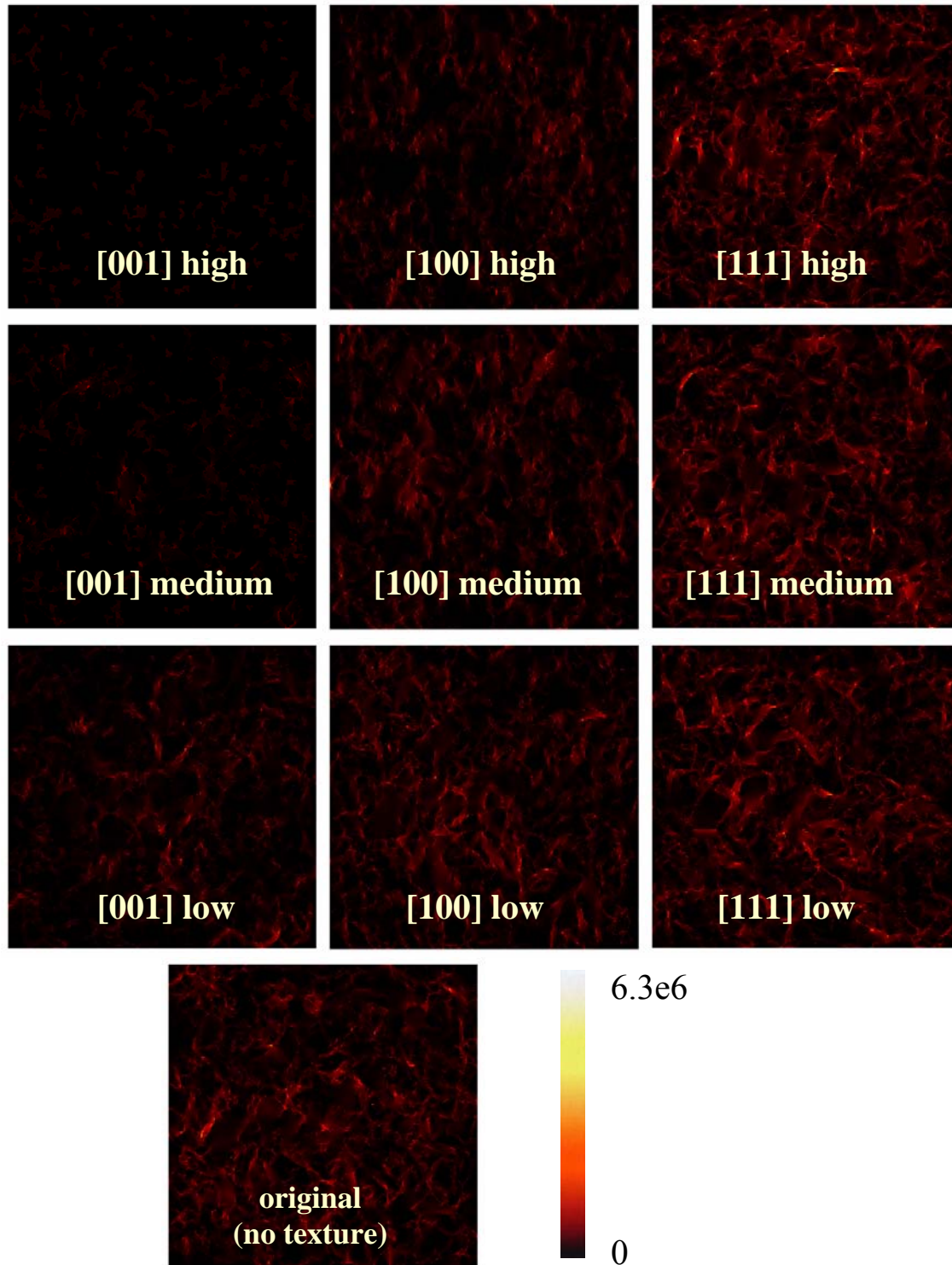
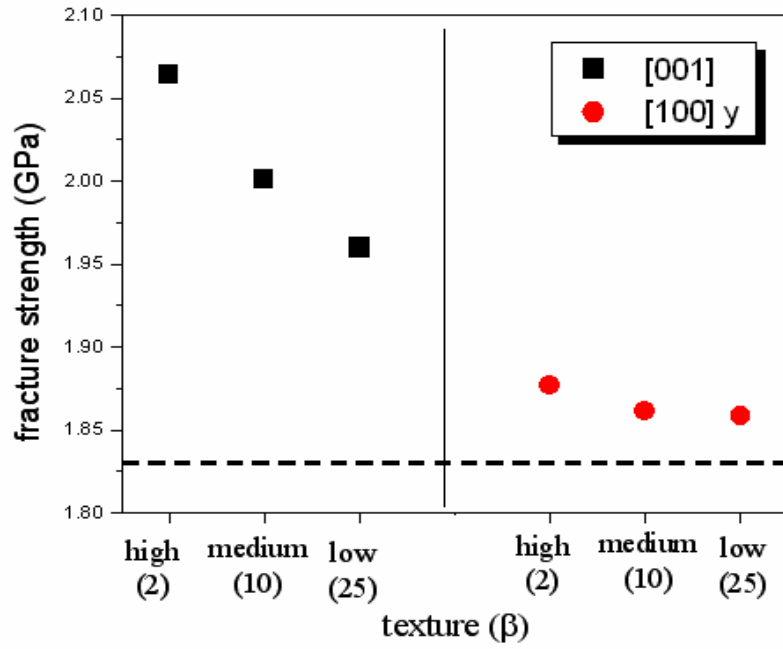
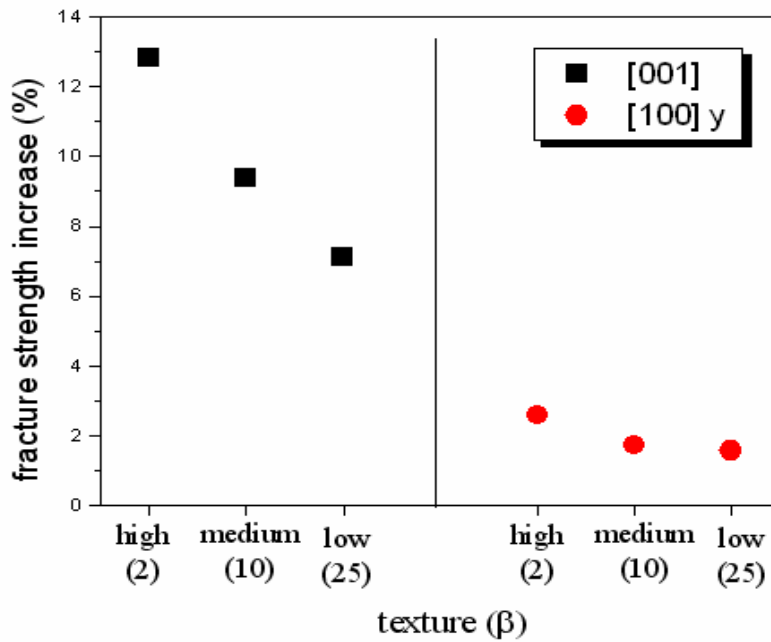


Fig. 5.33 : EED ([a.u.]) distributions with different orientation textures (from grade A). A thermal load of $\Delta T = -1400^\circ\text{C}$ was applied with free and plane stress boundary conditions. Same scale was used. The high [001] texture (upper-left) shows a low energy density distribution.

The fracture strength was calculated under a combined thermal and mechanical load in six sections of the nine (three with [001] texture and three with [100] texture, from grade A). Simulations were carried out using the same conditions as in the real microstructure (fixed and plane stress boundary conditions, and $\Delta T = -1400^\circ\text{C}$, see Section 5.2.3). Here, we tested the best ([001] texture) and worst (y-direction in the [100] texture) cases. In other words, we took the softest (the best case, x- and y- in [001] texture) and stiffest (the worst case, y- in [100] texture) axes for the strength calculations. In Fig. 5.34 (a), the strength of the [001] textured sample is the average of the x- and y-directions and the strength of the [100] textured sample was obtained by y-direction simulations. The results show that the [001] textured samples clearly have a higher strength; the dotted line indicates the strength of the real section (1.83 GPa, from grade A). Even in the calculations of the stiffest axis (y-direction of [100] texture), the approximated strength is not worse than that of real microstructure. The result indicates that the strength can be potentially increased by approximately 2 (the worst case) to 13 (the best case) % by texturing the sample (see Fig. 5.34 (b)).



(a)



(b)

Fig. 5.34 : The calculated (a) fracture strength and (b) fracture strength increase (%) with different orientation textures. Simulations were performed along the softest ([001] texture) and stiffest (y-direction in [100] texture) axes. The dotted line in (a) represents the strength of real microstructure (grade A).

Up to now, the effects of orientation texture on mechanical properties were presented by a single section from grade *A*. To generalize these observations, we expand the calculation to other grades (grades *B*, *C*, and *E*). Three different sections have been analyzed for each grade. The calculated fracture strength increase (%) is given in Fig. 5.35. The results are based on 72 (four different grades \times three sections for each grade \times six (three [001] and three [100] y) different textures) independent simulations. The range of the calculated fracture increase was calculated to be approximately -2 to 13 %. At all times, the maximum strength was found in the high [001] textured samples, and the minimum strength was found in the y-direction of high [100] textured samples. In the y-direction of high [100] textured sample, sometimes the calculated strength was lower than that of real sample; note that the minimum change in specimen grade *C* is -2 % (not shown in Fig. 5.35). Thus, the orientation texture does not always promote the strength along a certain direction, but it is considered that, generally, orientation textures with low misorientation angles enhance the strength of WC-Co composites. For more detail investigations, three-dimensional simulations need to be carried out, but, currently, this is not feasible in the OOF code.

Finally, it was observed that the relative maximum increment of the strength for different specimen grades is linear with the contiguity of the samples (see Fig. 5.36). It means the effect of WC/WC boundary misorientations is greater in high contiguity samples.

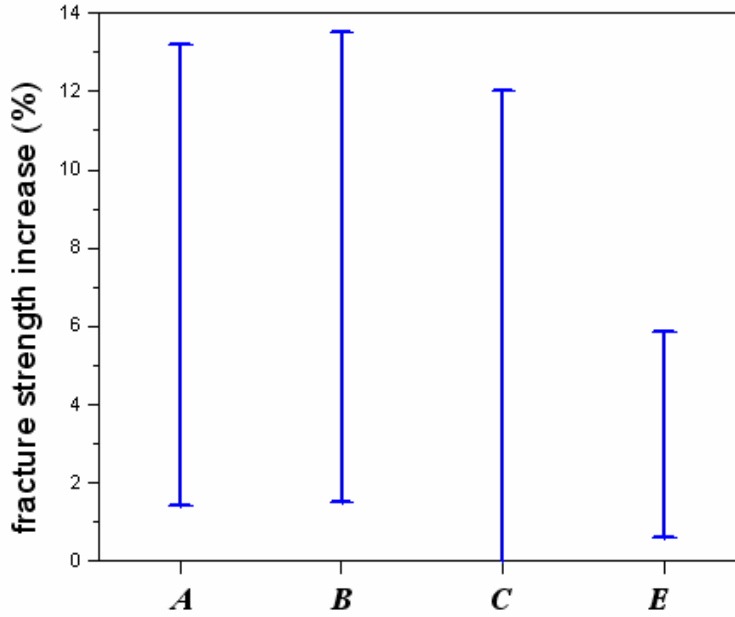


Fig. 5.35 : The calculated fracture strength increase (%) in the hypothetical microstructures of grades *A*, *B*, *C*, and *E*. Three sections were averaged for each grade. Maximum increment was found to be ~13% ([001] texture in the hypothetical *A* and *B*), and the minimum was approximated to be -2% (not shown, y-direction of [100] texture in the hypothetical *C*).

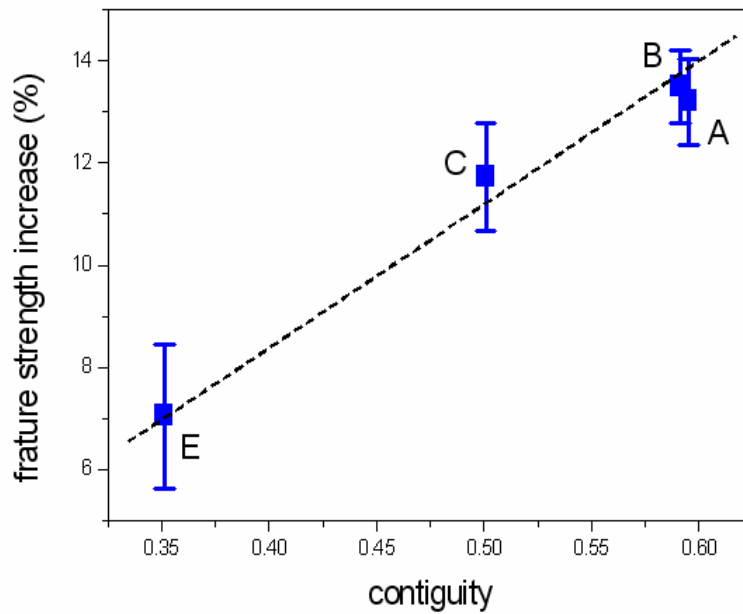


Fig. 5.36: The calculated maximum fracture strength increase as a function of contiguities. Three sections were averaged for each grade. Error bar indicates the standard deviation in sections. As the contiguity increases, the relative fracture strength increases.

5.4 Summary

A brittle fracture model for the fracture strength of WC-Co composites has been developed using finite element analysis (FEM). The model assumes that a crack initiates in the brittle carbide phase and that the fracture strength is proportional to the yield strength. When we use $\sim 49 \text{ J/m}^2$ as a constant surface energy under a combined load (thermal and mechanical), the brittle fracture model can approximate the fracture strength (transverse rupture strength). The calculated fracture strength using this model shows good agreement with the experimental data. With this brittle fracture model calibrated to calculate the fracture strength of real materials, the strength of hypothetical microstructures was then calculated. The most important factors appear to be the connectivity (contiguity) of the carbide skeleton, the orientation texture, and the misorientation texture. The angularity, the crystal size distribution, and the aspect ratio of the WC also influence strength, but these parameters are subordinate to contiguity and texture.

5.5 References

- [1] M. Lee and R.S. Gilmore, "Single Crystal Elastic Constants of Tungsten Monocarbide", *J. Mater. Sci.*, **17**, 2657 (1982)
- [2] A. Kelly and G.W. Groves, Crystallography and Crystal Defects, Longman Inc., London, 1973

- [3] W.C. Carter, S.A. Langer and E.R. Fuller Jr., The OOF Manual (version 1.0.8.6), National Institute of Standards and Technology (NIST), (2001); also available online at <http://www.ctcms.nist.gov/oof>
- [4] L.S. Sigl and H.E. Exner, “Experimental Study of Mechanics of Fracture in WC-Co Alloys”, *Metall. Trans. A*, **18A**, 1299 (1987)
- [5] L.S. Sigl and H.F. Fischmeister, “On the Fracture Toughness of Cemented Carbides”, *Acta Metall.*, **36**, No. 4, 887 (1988)
- [6] S. Bartolucci and H.H. Schlosin, “Plastic Deformation Preceding Fracture in Tungsten Carbide-Cobalt Alloys”, *Acta Metall. Mater.*, **14**, No. 3, 337 (1966)
- [7] W.M. Stoll and A.T. Santhanam, Kirk-Othmer Encyclopedia of Chemical Technology, 4th ed., **4**, John Wiley and Sons, Inc., 861, 1992

Chapter 6

Summary

This thesis focused on microstructure-property relationships in WC-Co composites and had three main components: quantitative microstructural measurements, measurements of the interface character distribution, and the development of a model to predict strength. Nine different specimen grades (seven straight angular grades, one straight non-angular grade, and one alloyed plate-like grade) with the average carbide grain sizes of one to seven microns and carbide volume fractions of 0.7 to 0.9 were used throughout this work.

For the microstructural characterization of these composites, the microscopic features were measured directly to avoid the inaccuracies and limitations of the conventional linear-intercept method. Geometric and crystallographic information was obtained using atomic microscopy (AFM) and orientation imaging microscopy (OIM). The composites studied in this work had very homogeneous microstructures. In all grades, the log normal distributions of carbide grain size and binder free path resemble the Gaussian distribution with normalized standard deviations of 0.55 to 0.60. It was found that the contiguity is a function of only the volume fraction of the carbide phase and it is strongly linear to the volume fraction in the range of 0.7 to 0.9. The average number of vertices per carbide grain was observed to be roughly constant; it varies from six to seven in the angular grades. The measured hardnesses and fracture toughnesses of these composites are mainly determined by the carbide grain size and contiguity (equivalently,

carbide volume fraction). Empirical expressions involving these two major parameters, the carbide grain size and contiguity, show a good agreement with the experimental values of the hardness and toughness.

A stereological method has been used to quantify the distributions of WC/Co interfaces and WC/WC grain boundaries. The surfaces of WC in contact with Co are mostly composed of $\{10\bar{1}0\}$ prismatic and $\{0001\}$ basal facets; 80 % of the WC/Co interfaces belong to one of those two habits within 5° tolerance angle. Approximately two thirds of the populations of these boundaries are prismatic planes and one third are basal planes, which leads the aspect ratio (base-to-height) of the prism shape to be 1.18 to 1.52, depending on the specimen grades. In the WC/WC grain boundaries, it was also found that the prismatic and basal planes dominate the populations. The population of these special facets is 60 % of the total boundary within a tolerance angle of 5° . Among them, there are two special boundaries, the 90° $[10\bar{1}0]$ and 30° $[0001]$ boundaries, which make up 11 to 14 % and 2 to 3 % of the total boundaries in the straight angular grades. The populations of these special boundaries in for the straight non-angular grade and the plate-like grade are approximately 7 % (90°), 1 % (30°), and 6 % (90°) and 7 % (30°), respectively.

The fracture strengths of WC-Co composites have been calculated using a two-dimensional finite element method (FEM) based on a Griffith-like brittle fracture criteria. The model approximates the fracture strength as the yield strength. The calculated fracture strength with the calibrated single fracture energy ($\sim 49 \text{ J/m}^2$) in the carbide phase shows a consistency with the measured transverse rupture strength. In calibrating the model, we found that the residual stress and strain resulting from a thermal load (cooling

down from the sintering temperature) is important to determine the fracture energy of the carbide phase. With this brittle fracture model, hypothetical microstructures were examined to investigate the effects of microstructural features on the strength of WC-Co composites. In Fig. 6.1, the effects of microstructural features are schematically illustrated. Here, the magnitudes of arrows indicate the extent of effect on the strength. The average grain size and volume fraction of the carbide phase mainly determine the fracture strength; this is also the case for hardness and fracture toughness. The contiguity and the texture of the carbide phase are the next most important parameters. It is predicted that the strength can be increased by as much as ~7 % by reducing the contiguity from 0.59 to 0.02 and/or by adopting a high degree of orientation and misorientation texture. The carbide shape and size distribution effects on the strength were also studied. It was observed that the equiaxed grain shape and homogenous size distribution can potentially increase the strength by ~3 to 4 %.

In this work, we didn't analyze the influence of the fraction of 90° and 30° special boundaries on mechanical properties. It has been reported that low energy boundaries can be used to improve mechanical properties, such as intergranular stress cracking [1-5], creep behavior, cavitation characteristics [6-9], fracture toughness [10, 11], cold work embrittlement [12], and weldability [13]. In WC-Co composites, it is anticipated that the mechanical properties would also be improved by increasing the fraction of special boundaries. Remarkably, the special boundary fraction was nearly constant in the commercial grades analyzed in this work. To include the effect of special boundaries, more complicated simulations need to be conducted; finer boundary meshes must be created and different fracture energy values must be specified. Also, for realistic

calculations to include the effects of grain boundary distributions, a three-dimensional simulation should be performed. This still remains a challenge for the future work.

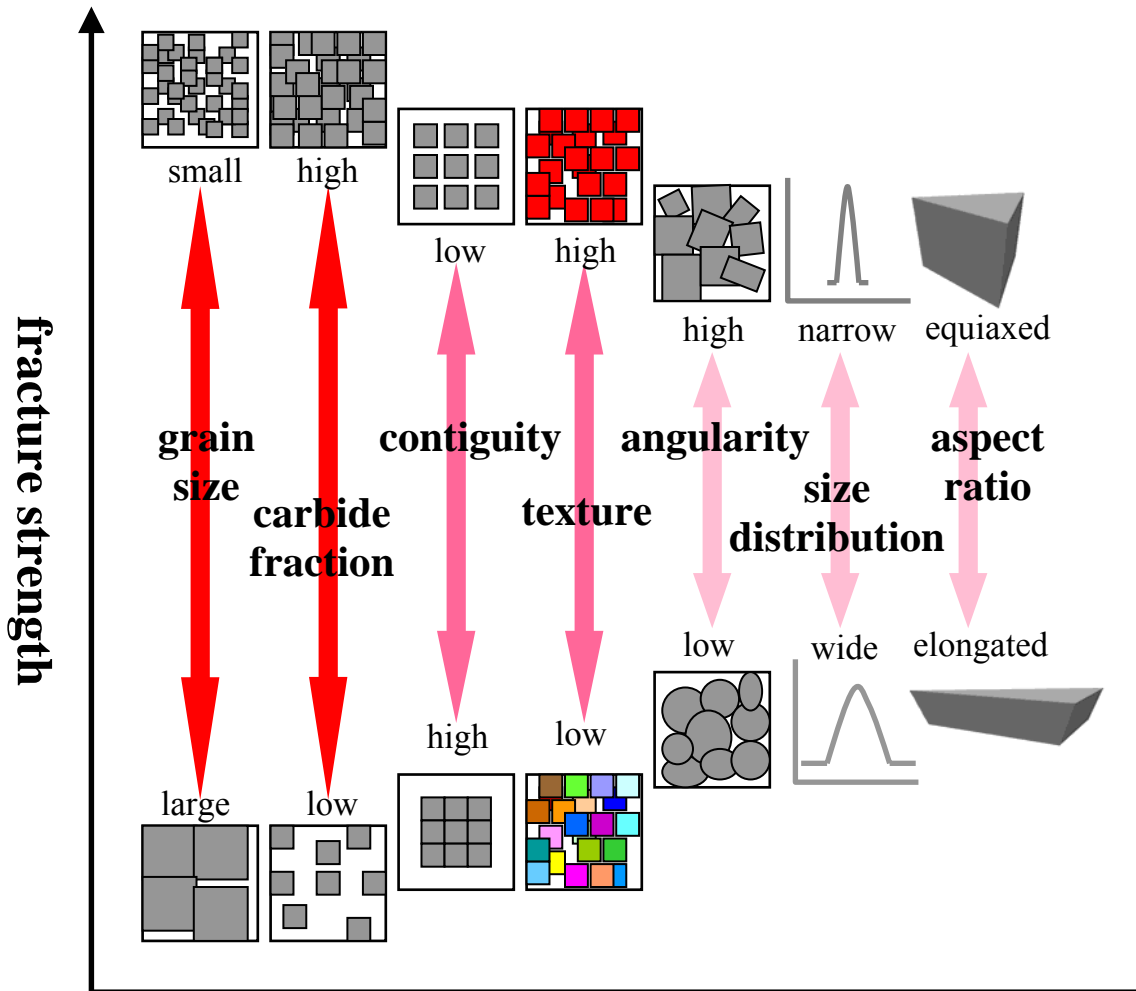


Fig. 6.1 : Schematic illustration of the effects of microstructural features on the fracture strength of composites. Carbide shapes are highly simplified. Different color contrasts for the texture effect represent different orientations.

6.1 References

- [1] G. Palumbo and K.T. Aust, “Localized Corrosion at Grain Boundary Intersections in High Purity Nickel”, *Scripta Metall.*, **22**, No.6, 847 (1988)
- [2] G. Palumbo and K.T. Aust, “Structure-Dependence of Intergranular Corrosion in High Purity Nickel”, *Acta Metall.*, **38**, No.11, 2343 (1990)
- [3] G. Palumbo, P.J. King, and K.T. Aust et al., “Grain Boundary Design and Control for Intergranular Stress-Corrosion Resistance”, *Scripta Metall.*, **25**, No.8, 1775 (1991)
- [4] P. Lin, G. Palumbo, U. Erb et al., “Influence of Grain Boundary Character Distribution on Sensitization and Intergranular Corrosion of Alloy 600”, *Scripta Metall.*, **33**, No.9, 1387 (1995)
- [5] D.C. Crawford and G.S. Was, “The Role of Grain Boundary Misorientation in Intergranular Cracking of Ni-16Cr-9Fe in 360 °C Argon and High Purity Water”, *Metall. Trans. A*, **23A**, No.4, 1195 (1992)
- [6] J. Don and S. Majumdar, “Creep Cavitation and Grain Boundary Structure in Type 304 Stainless Steel”, *Acta Metall.*, **34**, No.5, 961 (1987)
- [7] D.P. Field and B.L. Adams, “Interface Cavitation Damage in Polycrystalline Copper”, *Acta Metall.*, **40**, No.6, 1145 (1992)
- [8] V. Thaveerungsriporn and G.S. Was, “The Role of Coincidence Site Lattice Boundaries in Creep of Ni-16Cr-9Fe at 360 °C”, *Metall. Trans. A*, **28A**, No.10, 2101 (1997)

- [9] E.M. Lehockey, G. Palumbo, P. Lin et al., "On the Relationship between Grain Boundary Character Distribution and Intergranular Corrosion", *Scripta Mater.*, **36**, No.10, 1211 (1997)
- [10] L.C. Lim and T. Watanabe, "Fracture Toughness and Brittle-Ductile Transition Controlled by Grain Boundary Character Distribution (GBCD) in Polycrystals", *Acta Metall.*, **38**, No.12, 2507 (1990)
- [11] E.M. Lehockey, G. Palumbo, K.T. Aust et al., "On the Role of Intercrystalline Defects in Polycrystal Plasticity", *Scripta Mater.*, **39**, No.3, 341 (1998)
- [12] E.M. Lehockey, G. Palumbo, and P. Lin, "Grain Boundary Structure Effects on Cold Work Embrittlement of Microalloyed Steels", *Scripta Mater.*, **39**, No.3, 353 (1998)
- [13] E.M. Lehockey, G. Palumbo, and P. Lin, "Improving the Weldability and Service Performance of Nickel- and Iron-Based Superalloys by Grain Boundary Engineering", *Metall. Trans. A*, **29A**, No.12, 3069 (1998)